

AD \_\_\_\_\_

Award Number: DAMD17-02-2-0025

TITLE: Cholinesterase Structure: Identification of Mechanisms and Residues Involved in Organophosphate Inhibition and Enzyme Reactivation

PRINCIPAL INVESTIGATOR: Palmer W. Taylor, Ph.D.

CONTRACTING ORGANIZATION: The University of California  
La Jolla, California 92093-0934

REPORT DATE: May 2004

TYPE OF REPORT: Annual

PREPARED FOR: U.S. Army Medical Research and Materiel Command  
Fort Detrick, Maryland 21702-5012

DISTRIBUTION STATEMENT: Approved for Public Release;  
Distribution Unlimited

The views, opinions and/or findings contained in this report are those of the author(s) and should not be construed as an official Department of the Army position, policy or decision unless so designated by other documentation.

BEST AVAILABLE COPY

20040917 107

# REPORT DOCUMENTATION PAGE

**Form Approved  
OMB No. 074-0188**

Public reporting burden for this collection of information is estimated to average 1 hour per response, including the time for reviewing instructions, searching existing data sources, gathering and maintaining the data needed, and completing and reviewing this collection of information. Send comments regarding this burden estimate or any other aspect of this collection of information, including suggestions for reducing this burden to Washington Headquarters Services, Directorate for Information Operations and Reports, 1215 Jefferson Davis Highway, Suite 1204, Arlington, VA 22202-4302, and to the Office of Management and Budget, Paperwork Reduction Project (0704-0188), Washington, DC 20503.

1. AGENCY USE ONLY <i>(Leave blank)</i>	2. REPORT DATE May 2004	3. REPORT TYPE AND DATES COVERED Annual (15 Apr 2003 - 14 Apr 2004)	
4. TITLE AND SUBTITLE Cholinesterase Structure: Identification of Mechanisms and Residues Involved in Organophosphate Inhibition and Enzyme Reactivation		5. FUNDING NUMBERS DAMD17-02-2-0025	
6. AUTHOR(S) Palmer W. Taylor, Ph.D.			
7. PERFORMING ORGANIZATION NAME(S) AND ADDRESS(ES) The University of California La Jolla, California 92093-0934  E-Mail: pwtaylor@ucsd.edu		8. PERFORMING ORGANIZATION REPORT NUMBER	
9. SPONSORING / MONITORING AGENCY NAME(S) AND ADDRESS(ES) U.S. Army Medical Research and Materiel Command Fort Detrick, Maryland 21702-5012		10. SPONSORING / MONITORING AGENCY REPORT NUMBER	
11. SUPPLEMENTARY NOTES Original contains color plates: All DTIC reproductions will be in black and white.			
12a. DISTRIBUTION / AVAILABILITY STATEMENT Approved for Public Release; Distribution Unlimited		12b. DISTRIBUTION CODE	
13. ABSTRACT (Maximum 200 Words) Studies on the structural of acetylcholinesterase (AChE) as a target of organophosphate toxicity continue and have yielded several leads of significance and practical outcomes. First, studies on oxime reactivation reveal the importance of achieving a suitable angle of attack for the oxime within the confines of the active center gorge. Through the use of mutant AChE-oxime combinations, oxime assisted catalytic turnover of organophosphates can be achieved such that mutant AChE can be employed with oximes as a catalytic scavenger. Second, through cysteine substitution mutagenesis and acrylodan labeling we have developed a fluorescent enzyme whose emission spectrum changes upon conjugation with organophosphate. These enzymes are now being immobilized and developed as a remote sensor for acetylcholinesterase. Third, we have developed mass spectrometry methods to detect directly the organophosphate conjugates with AChE. Lastly, we have developed several transgenic animal strains that enable us to study the roles cholinesterase inhibition centrally and in the periphery play in organophosphate toxicity and whether the antidotal actions of oximes arise solely through reactivation.			
14. SUBJECT TERMS Acetylcholinesterase, organophosphate, oxime reactivation, fluorescence spectroscopy, nerve agent antidotes, exposure detection		15. NUMBER OF PAGES 86	
		16. PRICE CODE	
17. SECURITY CLASSIFICATION OF REPORT Unclassified	18. SECURITY CLASSIFICATION OF THIS PAGE Unclassified	19. SECURITY CLASSIFICATION OF ABSTRACT Unclassified	20. LIMITATION OF ABSTRACT Unlimited

## **Table of Contents**

<b>Cover.....</b>	<b>1</b>
<b>SF 298.....</b>	<b>2</b>
<b>Table of Contents.....</b>	<b>3</b>
<b>Introduction.....</b>	<b>4</b>
<b>Body.....</b>	<b>4</b>
<b>Key Research Accomplishments.....</b>	<b>9</b>
<b>Reportable Outcomes.....</b>	<b>9</b>
<b>Conclusions.....</b>	<b>9</b>
<b>References.....</b>	<b>9</b>
<b>Appendices.....</b>	<b>11</b>

## INTRODUCTION

Our overall objective of understanding the structure and function of acetylcholinesterase (AChE) as the target of organophosphate poisoning remains the same. This approach has several positive outcomes. First, AChE can be modified in its structure such that when the mutant enzyme is combined with oximes, it becomes a catalytic scavenger of organophosphates. Second, acrylodan or other fluorophore modification of AChE yields a fluorescent conjugate that can be used as a remote sensor for organophosphate exposure. Third, AChE conjugates can be detected directly by MALDI mass spectrometry, enabling us to characterize organophosphate exposure directly through detection of the conjugate, rather than indirectly through reduction of catalytic activity. Fourth, transgenic animal strains have been developed that should enable us to examine further the locus of organophosphate toxicity and understand the mechanism of action of oxime antidotes. Fifth, in new experiments we are employing a novel chemistry to synthesize oximes that cross the blood-brain barrier and have greater selectivity as antidotes. Sixth, the combination of these new approaches to the AChE oxime field has spawn new approaches for therapy for the organophosphates more refractory to antidotal therapy.

## BODY

The individual areas in which progress has been made are enumerated below.

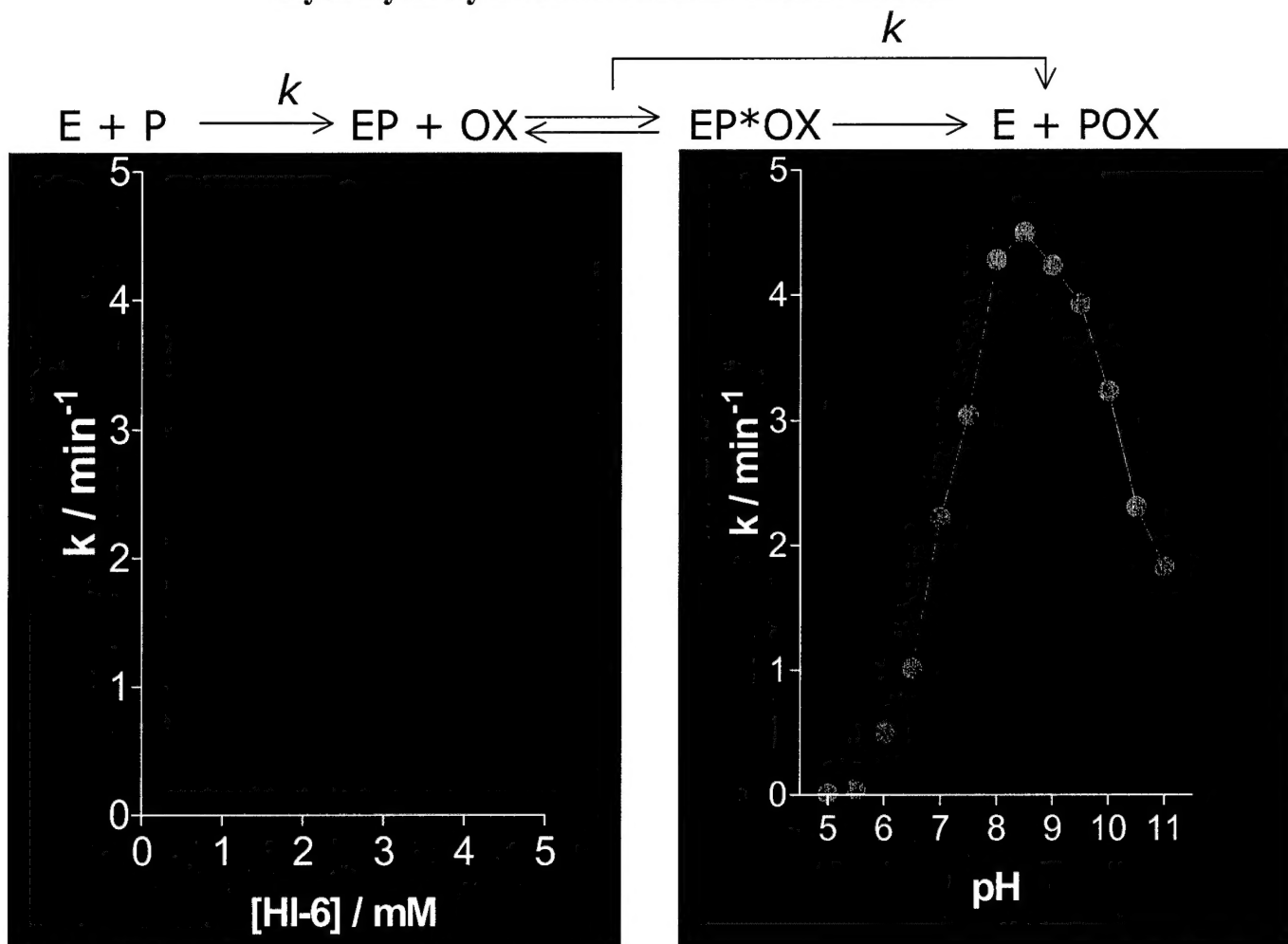
1. *Development of an Oxime-Mutant Acetylcholinesterase System for Catalytic Scavenging of Organophosphates.* In the last project period, we presented detailed kinetics on the rates of inactivation by cycloheptyl, isopropyl and 3,3-dimethylbutyl methylphosphonyl thioesters and the reactivation of the conjugates by two oximes, 2-PAM and HI-6. Reactivation studies showed the following:

- a. Efficient reactivation requires a phosphonate orientation where the phosphonyl (phosphoryl) oxygen is in the oxyanion hole. Hence, those S<sub>p</sub> or R<sub>p</sub> enantiomers that are the most reactive are also the ones most susceptible to reactivation (1).
- b. The narrow confines of the gorge ensure that the conjugated organophosphate is impacted at its base. Hence, the efficiency of the reactivation reaction is limited by the angle of access of the oxime to the phosphonyl phosphorus (1).
- c. Opening the gorge dimensions within prescribed limits enhances the rate of reactivation by the oxime. Each oxime has slightly different attack directions, hence the mutations that enlarge gorge dimensions have a differential effect on reactivation. Thus, reactivation efficiency depends on: the organophosphate structure, the structure of the attacking oxime, and the enzyme template (1).
- d. Optimization of the reaction, to date, has yielded a 120-fold increase in reactivation rate for the more bulky cycloheptyl methylphosphono-AChE conjugate. Enhancement rates are not as large for the isopropyl- and the 3,3dimethylbutyl methyl phosphonate conjugates (1).

These studies continue, and we have examined whether the aging rate affects the reactivation rates. We find that it does not, and we have also found that spontaneous hydrolysis is slow relative to oxime induced reactivation. Some of the R<sub>p</sub> compounds are extremely resistant to reactivation, and we have begun to examine structure-activity relationships for achieving more rapid reactivation. Similar considerations apply to tabun and related phosphoramidates, as well as the non-volatile VX compounds.

We have also noted that excessive enlargement of the active center gorge, such as is seen for butyrylcholinesterase, actually reduces oxime efficiency for reactivation. A more vacuous gorge may yield a configuration where the conjugated phosphate is buried in a crevice within the gorge. Accordingly, predictions on how to enhance further reactivation rates may be problematic. Accordingly, we have taken our best double mutant, Y297L-Y337A, and developed a continuous colorimetric assay for oxime turnover using the substituted alkyl methylphosphonothiocholines as reacting ligands. Turnover yields the corresponding

**Rate constant ( $k$ ) of  $S_p$ -Cycloheptyl Methylphosphonyl Thiocholine Hydrolysis by mAChE mutant F295L/Y337A**



**F295L/Y337A**

[HI-6] / mM	$k^* / \text{min}^{-1}$
0.1	0.65
0.5	2.1
1	3.3
2	3.9
5	4.5

\*0.5  $\mu\text{M}$  Enzyme  
20  $\mu\text{M}$  S-CHMPTCh  
100 mM Phosphate Buffer pH 7.4

1 mM HI-6	F295L/Y337	Y337A	F297I/Y337A	AChE w.t.
$k^* / \text{min}^{-1}$	3.3	0.69	0.34	0.15

Fig. 1: pH Dependence and Oxime Concentration Dependence for Cycloheptyl Methylphosphonylthiocholine Hydrolysis in the Presence of HI-6.

thiocholine that can be reacted with dithiodinitrobenzoate to form a yellow color. In figure 1, we examine the hydrolytic rate of one of the mutant enzymes. This assay has enabled us to measure the pH dependence and the catalytic parameters of oxime-assisted organophosphate hydrolysis. The kinetics reveal that the reaction is rate limited by oxime mediated dephosphorylation of the serine rather than the phosphorylation step. Thus, a suitable continuous assay applicable to multiwell, high throughput endeavors is now available for selecting mutants with enhanced organophosphate hydrolysis capacity.

*2. Studies with a Fluorescently Modified Acetylcholinesterase to Examine Conformation and Molecular Fluctuations in Enzyme Structure.* In the last project period, we showed that cysteine substitution mutagenesis at residues 81 and 84 followed by acrylodan labeling at these positions resulted in a fluorescent enzyme where excitation at 380nm yielded an emission peak residing between 480 and 525nm. The emission spectrum of acrylodan is very sensitive to its immediate dielectric constant. Thus, the immediate microenvironment around this introduced side chain can be ascertained. Several positions at the rim and just within the active center gorge and around the outside of the molecule were labeled. Residues within the gorge and near its rim where ligands bind show a decrease in dielectric constant as would be expected from the ligand excluding the H<sub>2</sub>O molecules upon binding. What was more surprising are the residues on the outer edge of the omega loop. Residue 84, at some distance from the binding site showed a red shift to longer wavelength with the binding of ligands. This change in fluorescence results from the acrylodan side chain becoming exposed to solvent upon ligand binding. We interpret this to result from the omega loop closing down on the bound ligand, increasing the curvature on the outer portion of the loop and causing the side chain to move into the solvent. Some plasticity of the omega loop must exist and is reflected in the emission changes seen at residue 81 where the S<sub>p</sub>-organophosphates and the reversibly bound ligands show the typical red shift to longer wavelength, whereas the R<sub>p</sub> compounds, when conjugated, cause a blue shift. The differences between enantiomers depend on whether the organophosphate phosphorus can fit into the oxyanion hole; the bulky R<sub>p</sub> compounds do not allow such a fit. If this fit does not occur, then the acyl pocket and base gorge structure are perturbed resulting in a distinctive positioning of the acrylodan at residue 81.

The practical outcome of these studies is that the Cys81 and Cys84 conjugated acrylodans can report on the exposure to organophosphate by the wavelength shift. Moreover, if the 81 residue is mutated and conjugated, the enzyme can distinguish between S<sub>p</sub> and R<sub>p</sub> methylphosphonates and the phosphorates that have a dimethoxy moiety (malathion, metrifonate, methylparathion-oxon, DDVP) from those that have a diethoxy or larger moiety (paraoxon, diisopropylfluorophosphate). The latter perturb the acyl pocket and their phosphoryl oxygen does not fit into the oxyanion hole giving rise to a blue shift.

These studies over the past 18 months have been followed up using fluorescence lifetime analysis and decay of fluorescence anisotropy for the study of molecular motion (2,3). Anisotropy studies reveal two important points. First, differences in molecular motional fluctuations can be mapped at the various sites in the molecule as torsional, segmental and global motion. Second, the active center gorge exists in a dynamic equilibrium with rapid opening and closing of the gorge presumably on a nanosecond to picosecond time frame. This time frame is short relative to the diffusional translation time of the diffusing ligand.

Current efforts are devoted to examining other residues on the non-omega loop side of the gorge. Residues 341 and its neighbors reveal fluctuations in structure around the gorge rim. Here again, we notice considerable fluctuations in this region with diminished motion as we descend into the gorge base. A second set of studies examines omega loop conformation where the active center serine has been removed or the histidine in the catalytic triad has been replaced by a isoleucine. This approach has enabled us to distinguish perturbations of structure involving the formation of the initial complex and formation of the covalent conjugate with the organophosphate.

As an aside, we found through these methods that the trifluoroacetophenones that form a hemiketal linkage with the active site serine do not require an intact catalytic triad for isoleucine can be substituted for histidine

447 and a hemiketal conjugate still forms with *m*-trimethylammonio trifluoroacetophenone, whereas the same mutant enzyme will not form conjugates with organophosphates and catalyze ester hydrolysis.

Current endeavors are directed to using the fluorescent enzyme in a remote sensing device to detect organophosphate exposure. The approach has a three-fold advantage. First, detection of organophosphate inhibition of enzyme activity depends on the reduction from full activity and full activity is subject to considerable biological variation between individuals and over time. Hence, 10 or 20% differences in activity cannot be ascribed to organophosphate inhibition. On the other hand, measurement of the actual organophosphate conjugate by the wavelength shift and wavelength ratio is easier to detect as a significant change relative to exposure. Second, the fluorescent enzyme is the very target of organophosphate toxicity and is less susceptible to false inhibition seen with simple colorimetric or fluorometric compounds. Third, detection does not require reagent addition for it is only the organophosphate conjugation that causes the fluorescence change. Hence, this system is well suited for remote sensing with a laser light source and photomultiplier detection.

Current studies are directed to placing the enzyme in a polyvinyl pyrrolidine matrix that keeps it hydrated but non-diffusible. These studies are being done with Dr. Sangeeta Bhatia, who has considerable experience with placing enzymes and cells in hydrated matrices for high through-put detection. Should this approach not be successful, we have arranged alternative experiments with Dr. John G. Reynolds of the Lawrence Berkeley laboratories, who has been studying phosphatases in immobilized matrices.

*3. Analysis of Organophosphate Conjugation by Mass Spectrometry: Conjugates of the Active Center Serine.* These studies have now come to fruition for the phosphorotester insecticides where we have been able to follow the kinetics of inactivation by the organophosphate, ageing and spontaneous reactivation by isolating the active center serine peptide and determining its mass using a MALDI source (4). Moreover, the method is quite sensitive for we have been able to measure the conjugated organophosphate, dimethoxyphosphoryl serine peptide, and aged species in single brain samples after exposure to metrifonate. Current studies are directed to methylphosphonate detection *in vitro* and following *in situ* exposure to sarin and cyclosarin analogs. Second, we have begun to add oximes to these studies in order to ascertain the conjugate products after oxime exposure. In particular, we are measuring whether in some cases the oxime does not reactivate, but rather promotes aging. This is quite possible since the leaving group would be the serine alkoxy moiety or the alkoxy moiety on the methylphosphonate. The studies should be facilitated by our recent acquisition of a ABI Qstar XL quadrupole-time of flight mass spectrometer with both electrospray ionization (ESI) and Matrix-assisted Laser Desorption Ionization (MALDI) sources available. The nanoflow liquid chromatography capacity also enhances our sensitivity, and our preliminary runs suggest that the sensitivity enhancement is about an order of magnitude.

We have also employed mass spectrometry analysis of the tryptic peptides to analyze whether methionine oxidation correlates with inactivation of the enzyme. Indeed that seems to be the case, and we find that methionine 222 is the offending residue. Its oxidation to the corresponding sulfoxide and perhaps the sulfone correlates with the inactivation process. To confirm this, we are currently mutating the methionine to a leucine, a substitution that should yield a more oxidation resistant enzyme.

*4. Studying Organophosphate Resistance with Transgenic Animal Strains.* Although the initial work was supported by a grant from the National Institute of Environmental Health Sciences, we have produced a series of transgenic mice strains that should prove useful in the study of susceptibility to organophosphate exposure. The various mouse strains are outlined in Figure 2. They include: (a) the total knock out of the gene, generated and studied primarily by Dr. Oskana Lockridge, (b) deletion of exon 5 – a deletion that prevents formation of the glycophospholipid-linked form of AChE, a form that resides primarily in hematopoietic cells, (c) deletion of exon 6-a deletion which precludes the expression of the major form of AChE in nerve and muscle and a form that tethers to the plasma or basal lamina membranes, (d) deletion of exons 5 and 6-a deletion that will eliminate

- all membrane associated forms of AChE giving rise to only a soluble form of the enzyme, and (e) deletion of an upstream intron between exons 1 and 2. This intron controls expression of AChE with the differentiation of skeletal muscle, but we are unsure of its influence in neuronal tissue. The latter knock-out has been done with the Cre-lox system so that developmentally controlled and tissue-selective knock outs are possible.

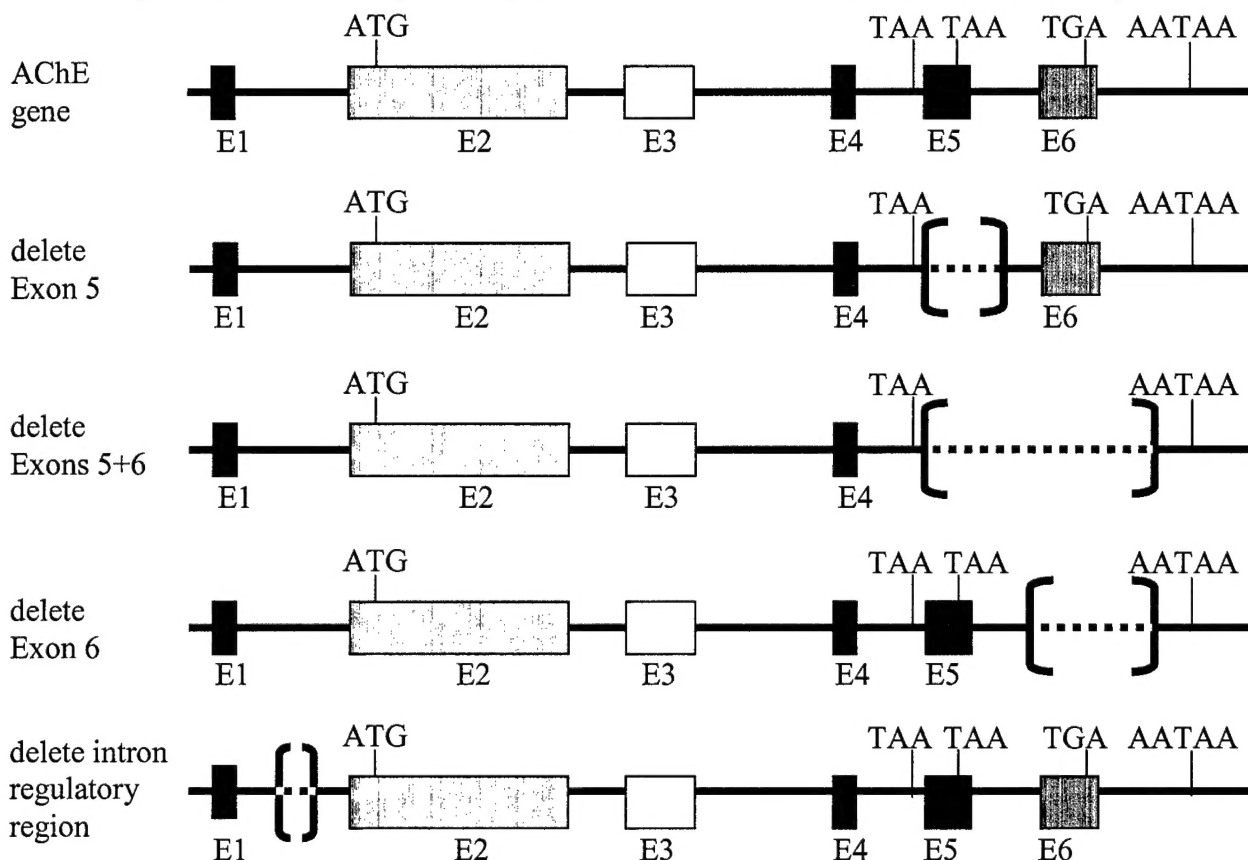


Fig 2: Structure of the Mouse Acetylcholinesterase Gene. The 7.5kb region from promoter to the second 3' polyadenylation signal is shown.

The knock out strains are being characterized phenotypically in terms of multiple parameters. These include expression levels in brain, blood, liver and skeletal muscle, identification of molecular forms in the tissues of interest: skeletal muscle, regional areas of brain, cerebral spinal fluid, erythrocyte membranes and platelet membranes and interiors. Behavioral, muscle strength, physiologic and metabolic parameters are also being assessed. Once complete, we will then assess susceptibility to organophosphates and to oxime reactivation. Such animals will prove of considerable value since they will help us ascertain the extent to which toxicity is central or peripheral and what tissues are most involved. In addition, a non-chemical means of controlling AChE activity should tell us whether certain oximes have therapeutic value arising from mechanisms other than reactivation.

*5. Development of a New Generation of Oximes.* Our recent studies with Barry Sharpless group have led to a new approach to structure-guided drug design, where the drug target itself becomes a mini-reaction vessel in which the two precursor molecules. The approach involves allowing precursor molecules containing azide and acetylene groups to react through cycloaddition forming high affinity triazoles. This can be done with combinatorial libraries and identifying the preferential reaction product with the highest affinity. To date, we have accomplished the following:

- a) characterized the preferential *syn* cycloaddition products and the template determinants controlling the reaction
- b) ascertained the structures of the *syn* and *anti* complexes with acetylcholinesterase and delineated the distinguishing conformational features of the complexes
- c) develop precursor ligands that will cross the blood-brain barrier
- d) designed approaches to employ cycloaddition chemistry in oxime design

## KEY RESEARCH ACCOMPLISHMENTS

These accomplishments are detailed as six achievements in the INTRODUCTION.

## REPORTABLE OUTCOMES

The reportable outcomes are listed in the seven publications listed in the Reference section.

## CONCLUSIONS

Our studies have been developed around the strategy of characterizing the target of organophosphate, nerve agent action, acetylcholinesterase. Target characterization and modification have enabled us to: (a) employ acetylcholinesterase in combination with oximer as a potential *in vivo* scavenger for nerve agents, (b) develop fluorescent conjugates of acetylcholinesterase for potential detection of exposure to nerve agents, (c) analyze the conjugate of the organophosphate with an active center peptide by mass spectrometry to detect cumulative exposure to organophosphates and identify the agent, (d) modify the gene encoding acetylcholinesterase to produce transgenic animals with unusual sensitivities to organophosphates, (e) use cholinesterase itself as a template to synthesize selective inhibitors and, more importantly new modalities of oxime therapy.

## REFERENCES

1. Kovarik, Z., Radic, Z., Berman, H.A., Simeon-Rudolf, V., Reiner, E., and Taylor, P. Mutant Cholinesterases Possessing Enhanced Capacity for Reactivation of Their Phosphonylated Conjugates. *Biochemistry*, 43, 3222-3229 (2004).
2. Shi, J., Tai, K., McCammon, J.A., Taylor, P., and Johnson, D.A. Nanosecond Dynamics of the Mouse Acetylcholinesterase Cys69-Cys96 Omega Loop, *J. Biol. Chem.*, 278, 30905-30911 (2003).
3. Boyd, A. E., Dunlop, C., Wong, L., Radic, Z., Taylor, P., and Johnson, D. Nanosecond Dynamics of Acetylcholinesterase Near the Active-Center Gorge. *J. Biol. Chem.*, 279, 26612-26618 (2004).
4. Hoffman, R., Jennings, L., Tsigelny, I., Comoletti, D., Flynn, R.E., Sudhof, T.C., and Taylor, P. Structural Characterization of Recombinant Soluble Rat Neuroligin 1: Mapping of Secondary Structure and Glycosylation by Mass Spectrometry. *Biochemistry*, 43, 1496-1506 (2004).
5. Camp, S., Zhang, L., Marquez, M. and Taylor, P. Knockout Mice with Deletions of Alternatively Spliced Exons of Acetylcholinesterase. *Cholinesterases in the Second Millennium: Biomolecular and Pathological Aspects* pp. 43-47 (2004).

- 6. Bourne, Y., Kolb, H.D., Radic Z., Sharpless, K. B., Taylor, P. and Marchot, P. Freeze-frame Inhibitor Captures Acetylcholinesterase in a Unique Conformation. *Proc. Natl. Acad. Sci.*, 101, 1449-1454 (2004).
- 7. Krasinski, A., Manetsch, R., Radic', Z., Raushel, J., Taylor, P., Sharpless, K.B. and Kolb, H.C. *In Situ* Click Chemistry: Enzyme Inhibitors Made to their own Specifications. *J. Amer. Chem. Soc.* (2004), Submitted for publication.

## Mutant Cholinesterases Possessing Enhanced Capacity for Reactivation of Their Phosphonylated Conjugates<sup>†</sup>

Zrinka Kovarik,<sup>‡,§</sup> Zoran Radić,<sup>‡</sup> Harvey A. Berman,<sup>||</sup> Vera Simeon-Rudolf,<sup>§</sup> Elsa Reiner,<sup>§</sup> and Palmer Taylor\*,<sup>‡</sup>

*Department of Pharmacology, University of California at San Diego, La Jolla, California 92093-0636,  
Institute for Medical Research and Occupational Health, HR-10000 Zagreb, Croatia, and Department of Pharmacology and  
Toxicology, School of Medicine, University at Buffalo, Buffalo, New York 14214*

Received December 5, 2003; Revised Manuscript Received January 12, 2004

**ABSTRACT:** Selective mutants of mouse acetylcholinesterase (AChE; EC 3.1.1.7) phosphonylated with chiral *S*<sub>P</sub>- and *R*<sub>P</sub>-cycloheptyl, -3,3-dimethylbutyl, and -isopropyl methylphosphonyl thiocholines were subjected to reactivation by the oximes HI-6 and 2-PAM and their reactivation kinetics compared with wild-type AChE and butyrylcholinesterase (EC 3.1.1.8). Mutations in the choline binding site (Y337A, Y337A/F338A) or combined with acyl pocket mutations (F295L/Y337A, F297I/Y337A, F295L/F297I/Y337A) were employed to enlarge active center gorge dimensions. HI-6 was more efficient than 2-PAM (up to 29000 times) as a reactivator of *S*<sub>P</sub>-phosphonates ( $k_r$  ranged from 50 to 13000 min<sup>-1</sup> M<sup>-1</sup>), while *R*<sub>P</sub> conjugates were reactivated by both oximes at similar, but far slower, rates ( $k_r < 10$  min<sup>-1</sup> M<sup>-1</sup>). The Y337A substitution accelerated all reactivation rates over the wild-type AChE and enabled reactivation even of *R*<sub>P</sub>-cycloheptyl and *R*<sub>P</sub>-3,3-dimethylbutyl conjugates that when formed in wild-type AChE are resistant to reactivation. When combined with the F295L or F297I mutations in the acyl pocket, the Y337A mutation showed substantial enhancements of reactivation rates of the *S*<sub>P</sub> conjugates. The greatest enhancement of 120-fold was achieved with HI-6 for the F295L/Y337A phosphonylated with the most bulky alkoxy moiety, *S*<sub>P</sub>-cycloheptyl methylphosphonate. This significant enhancement is likely a direct consequence of simultaneously increasing the dimensions of both the choline binding site and the acyl pocket. The increase in dimensions allows for optimizing the angle of oxime attack in the spatially impacted gorge as suggested from molecular modeling. Rates of reactivation reach values sufficient for consideration of mixtures of a mutant enzyme and an oxime as a scavenging strategy in protection and treatment of organophosphate exposure.

Organophosphates are potent inhibitors of acetylcholinesterase (AChE;<sup>1</sup> EC 3.1.1.7) and butyrylcholinesterase (BChE; EC 3.1.1.8). The progressive inhibition of cholinesterases by organophosphates is due to phosphorylation (denotes phosphonylation and phosphorylation) of their active center serine characterized by the formation of conjugates, which react very slowly with water. Inhibition of AChE is the main cause of organophosphate toxicity (*J*). Early studies on reactivation of the enzyme by Wilson and colleagues showed that, by directing nucleophiles to the active site, conjugated organophosphates could be released, regenerating the active enzyme (*2, 3*). Strong nucleophiles such as oximes are particularly effective in reactivating organophosphate-

cholinesterase conjugates. Nucleophilic strength, the orientation of the nucleophile with respect to the conjugated organophosphate, and the rate of aging (postinhibitory dealkylation) are three factors well-known to affect reactivation. During the past several decades, effective oximes have been developed as antidotes to cholinesterase poisoning that greatly improve efficacy of treatment of acute organophosphate poisoning (*4*). The monopyridinium oxime, 2-PAM, and bispyridinium oxime, HI-6, are the most potent reactivating agents in use in antidotal therapy (Figure 1). The effectiveness of oxime reactivators is primarily attributed to the nucleophilic displacement rate of the organophosphates, but efficiency varies with the structure of the bound organophosphate, the source of enzyme and the oxime.

\* This work was supported by Grants DAMD17C8014 and R37-GM18360 to P.T., Grant 0022014 to V.S.-R., and fellowships of the Ministry of Science and Technology of the Republic of Croatia and the Wood-Whelan Research Fellowship (IUBMB) to Z.K.

<sup>†</sup> To whom correspondence should be addressed. Telephone: 858-534-1366. Fax: 858-534-8248. E-mail: pwtaylor@ucsd.edu.

<sup>‡</sup> University of California at San Diego.

<sup>§</sup> Institute for Medical Research and Occupational Health.

<sup>||</sup> University at Buffalo.

<sup>1</sup> Abbreviations: AChE, acetylcholinesterase; ATCh, acetylthiocholine iodide; BChE, butyrylcholinesterase; 2-PAM, 2-(hydroxyiminomethyl)-1-methylpyridinium iodide; HI-6, 1-(2'-hydroxyiminomethyl-1'-pyridinium)-3-(4"-carbamoyl-1"-pyridinium)-2-oxapropene dichloride.

The crystal structures of AChE (*5–7*) provide templates for detailed structural studies on ligand access to the impacted enzyme active center gorge and steric constraints within the active center gorge that govern selectivity in organophosphate inhibition (*8–13*) and oxime reactivation (*14–18*). The site of conjugation by organophosphates lies at the base of a narrow and 18–20 Å deep gorge. The gorge wall of AChE is lined largely by aromatic side chains contributing to a well-defined acyl pocket and choline binding site at the base of the gorge (*19, 20*). Therefore, the orientation of the associated

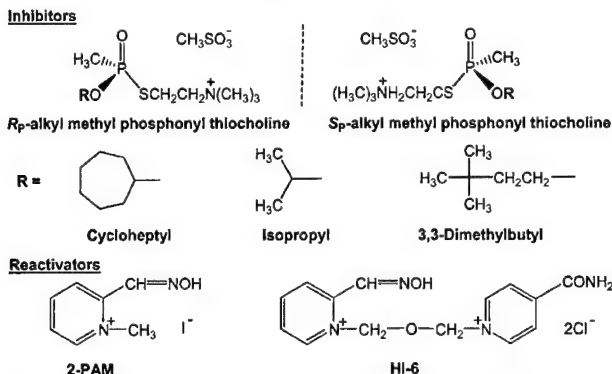


FIGURE 1: Structures of the organophosphonates and oximes used in this study.

and conjugated ligands within narrow confines of the gorge and the rates of nucleophilic attack by oxime at the conjugated phosphorus atom become important determinants of the reactivation mechanism.

In this study, we investigated structural and kinetic bases for reactivation of the enzyme conjugates by oximes using a combined structure–activity approach where both inhibitor and enzyme were modified systematically. Mouse AChE was modified within the choline binding site (Y337A, F338A) and the acyl pocket (F295L, F297I) in various mutation permutations. The mutant AChE species, except for F338A, contained mutations that resemble residues found at structurally equivalent positions in BChE (residue numbering corresponds to mouse AChE). This enabled us to examine the basis of the divergence between oxime reactivation of phosphorylated AChE and BChE. By using a congeneric series of *S*<sub>P</sub>- and *R*<sub>P</sub>-alkyl methylphosphonyl thiocholines and two related oximes of different dimensions, HI-6 and 2-PAM (Figure 1), subtle differences in reactivation capability have been analyzed with the objective of enhancing reactivation rates.

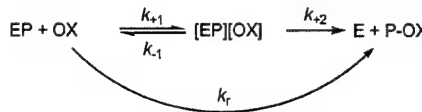
## MATERIALS AND METHODS

**Chemicals.** *S*<sub>P</sub>- and *R*<sub>P</sub>-alkyl methylphosphonyl thiocholines were synthesized and isolated as resolved *S*<sub>P</sub> and *R*<sub>P</sub> enantiomers (8). Stock solutions in acetonitrile were kept at –20 °C, and aliquots were diluted in water immediately before use. HI-6 was a gift of B. P. Doctor at Walter Reed Army Research Center, Washington, DC. 2-PAM, acetylthiocholine iodide (ATCh), 5,5'-dithiobis(2-nitrobenzoic acid), and bovine serum albumin (BSA) were purchased from Sigma Chemical Co., St. Louis, MO. Both oximes, HI-6 and 2-PAM, were kept at –20 °C, and they were dissolved and diluted in water immediately before use.

**Enzymes.** Preparation, expression, purification, and characterization of recombinant wild-type mouse AChE and wild-type mouse BChE and AChE mutants were described in detail in previous studies (9, 13, 19, 21).

**Oxime Reactivation of the Phosphorylated Enzyme.** Wild-type and mutant enzymes (concentrations between 0.01 and 1.0 μM) were reacted with an ~10% molar excess of the corresponding alkyl methylphosphonate until inhibition was greater than 90%. Typical inhibition times were 30 min to 2 h, except for the case of slower inhibition with *R*<sub>P</sub> enantiomers, when the required time was up to 6 h. The inhibited enzyme was passed through a Sephadex G-50 spin column

Scheme 1



(Pharmacia) to remove excess unconjugated organophosphate and incubated with specified concentrations of oxime in 10 mM Tris-HCl buffer, pH 8.0, containing 0.01% BSA, 40 mM MgCl<sub>2</sub>, and 100 mM NaCl. At specified time intervals, 5–10 μL of the reactivation mixture was diluted up to 100-fold, and residual activity was measured at 22 °C by the Ellman method using ATCh as substrate (1.0 mM final concentration) (22). An equivalent sample of uninhibited enzyme was passed through a parallel column, diluted to the same extent as the inhibition mixture, and control activity was measured in the presence of oxime at concentrations used for reactivation. Both activities of the control and reactivation mixture were corrected for oxime-induced hydrolysis of ATCh, whenever oxime concentrations were greater than 1.0 mM.

**Kinetics of Oxime Reactivation.** Oxime reactivation of phosphorylated cholinesterases proceeds according to Scheme 1. In this scheme EP is the phosphorylated enzyme, [EP][OX] is the reversible Michaelis-type complex between EP and the oxime (OX), E is the active enzyme and P-OX the phosphorylated oxime, *k*<sub>+2</sub> is the maximum first-order rate constant, and *k*<sub>r</sub> is the overall second-order rate constant of reactivation.

Scheme 1 is defined by the equation:

$$\ln \frac{[EP]_0}{[EP]_t} = \frac{k_{+2}[OX]}{K_{OX} + [OX]} t = k_{obs} t \quad (1)$$

where [EP]<sub>0</sub> and [EP]<sub>t</sub> are the concentrations of the phosphorylated enzyme at time zero and at time *t*, respectively. *K*<sub>OX</sub> is equal to the ratio (*k*<sub>-1</sub> + *k*<sub>+2</sub>)/*k*<sub>+1</sub>, and it typically approximates the dissociation constant of the [EP][OX] complex. *k*<sub>obs</sub> is the observed first-order rate constant of reactivation at any given oxime concentration.

When *K*<sub>ox</sub> ≫ [OX], eq 1 simplifies to

$$\ln \frac{[EP]_0}{[EP]_t} = \frac{k_{+2}}{K_{OX}} [OX] t = k_r [OX] t = k_{obs} t \quad (2)$$

where from it follows that

$$k_r = \frac{k_{+2}}{K_{OX}} \quad (3)$$

Experimental data were presented as percent of reactivation

$$\% \text{ reactivation} = \frac{v_{(EP+OX)} - v_{(E+OX)}}{v_{(E+OX)}} \times 100 \quad (4)$$

where *v*<sub>(EP+OX)</sub> denotes the activity of the reactivated enzyme at time *t* and *v*<sub>(E+OX)</sub> stands for the activity of the unmodified enzyme incubated with oxime. Both activities were corrected for oxime-induced hydrolysis of ATCh. If the enzyme was not completely inhibited prior to reactivation, both activities in eq 4 were also corrected for the enzyme activity at time

zero. Since  $(100 - \% \text{ reactivation})$  is equal to  $100[\text{EP}] / [\text{EP}]_0$ , one can relate the experimental data to eqs 1 and 2.

At each oxime concentration,  $k_{\text{obs}}$  was calculated from the slope of the initial portion of  $\log(100 - \% \text{ reactivation})$  vs time of reactivation plot as  $k_{\text{obs}} = -2.303 \times \text{slope}$ , assuming an approach to 100% reactivation. When reactivation followed eq 1,  $k_{+2}$  and  $K_{\text{ox}}$  were obtained by the nonlinear fit of the relationship between  $k_{\text{obs}}$  vs  $[\text{OX}]$ ;  $k_r$  was calculated from eq 3. When reactivation followed eq 2,  $k_{\text{obs}}$  vs  $[\text{OX}]$  was linear, and the slope corresponded to  $k_r$ ; in this case constants  $k_{+2}$  and  $K_{\text{ox}}$  could not be determined.

**Molecular Modeling.** Molecular modeling analysis was performed in order to ascertain probable HI-6 orientations inside the active center gorges of  $S_p$ -cycloheptyl methylphosphonylated wild-type mouse AChE and F295L/Y337A mouse AChE, where the HI-6 oxime group was facing the phosphorus conjugated to the AChE active center serine. The model of HI-6 was built as described earlier (14, 18) and docked manually inside active center gorges of either  $S_p$ -cycloheptyl wild-type mouse AChE (taken from ref 18) or  $S_p$ -cycloheptyl F295L/Y337A mutant mouse AChE (generated from phosphonylated wild-type mouse AChE using the Insight II program suite, Accelrys, San Diego) to achieve starting structures of the complex. Molecular dynamics of the complex was then performed using the procedure described earlier (14) and repeated 20 times for both wild-type and mutant complexes. During the computation the conformation of the HI-6 molecule was unrestricted, as were the side chains of AChE residues at positions 295, 297, 338, and phosphonylated serine at 203. The resulting 20 conformers of the complex were analyzed for their total energy and distance between the oxime group oxygen and phosphonate phosphorus.

## RESULTS

**Oxime Reactivation Kinetics.** Recombinant DNA-expressed mouse cholinesterases phosphonylated with  $S_p$ - and  $R_p$ -alkyl methylphosphonyl thiocholines were subjected to reactivation by HI-6 and 2-PAM. The series of reactivation reactions were run over a wide concentration range of oximes to determine constants  $k_{+2}$ ,  $K_{\text{ox}}$ , and  $k_r$  (Figure 2). The results for the 74 distinct oxime–enzyme combinations are listed in Tables 1–6. In 18 reactions, the rates of reactivation were so slow that rate constants could not be reliably determined. For these reactions only the maximum percent of reactivation obtained within the stated time is listed in the tables. For reactivation of the triple mutant F295L/F297I/Y337A only limiting values of constants were calculated because reactivation was measured at one oxime concentration only. For 8 reactions the  $k_{\text{obs}}$  values were a linear function of the oxime concentration; consequently, only the bimolecular  $k_r$  constants could be calculated. For 44 reactions, all three constants ( $k_{+2}$ ,  $K_{\text{ox}}$ ,  $k_r$ ) were obtained as presented in Figure 2 and are displayed in the tables including the maximum percent of reactivation obtained with the highest oxime concentration after the indicated time of reaction. The mean relative standard error of  $k_{+2}$  was 11%, while the corresponding errors of  $K_{\text{ox}}$  and  $k_r$  were larger, 43% and 39%, respectively.

All  $k_{\text{obs}}$  constants were calculated from the initial slope of the reactivation profile. For some of the reactions, typically those where the reactivation was not complete (cf. Tables

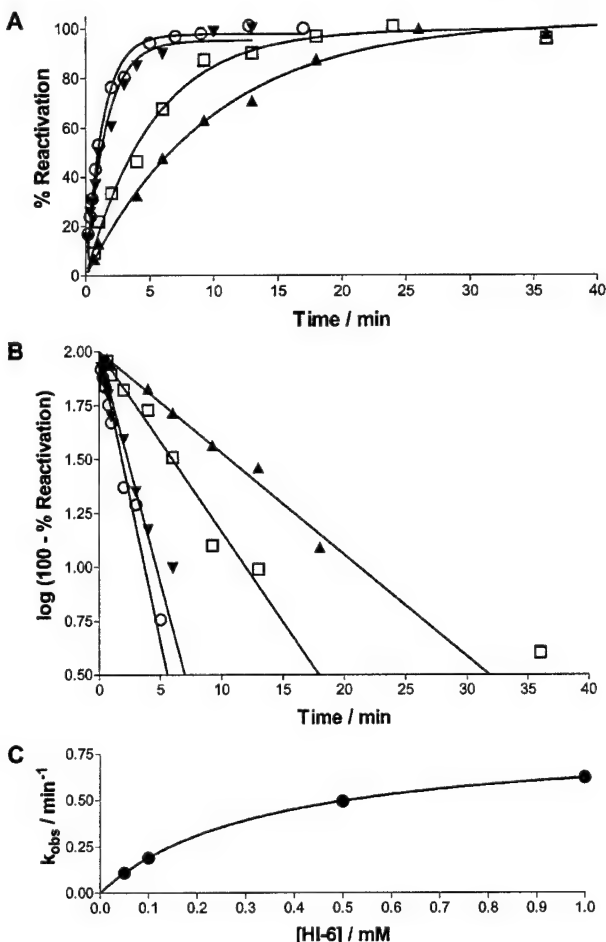


FIGURE 2: Reactivation of the  $S_p$ -isopropyl methylphosphonyl F297I/Y337A conjugate by HI-6. (A) Single datum points indicate calculated percent reactivation by eq 4 after the designated time of reactivation with (○) 1, (▼) 0.5, (□) 0.1, and (▲) 0.05 mM HI-6. (B) Slopes of the reactivation curve yield  $k_{\text{obs}}$  constants. (C)  $k_{\text{obs}}$  is plotted as a function of HI-6 and the line fitted using eq 1.

1–6), the kinetics at the longer time intervals deviated from the first-order process described in eqs 1 and 2. This deviation could be due to a fraction of the phosphonylated enzyme aging with the loss of the alkoxy group, reinhibition of the active enzyme by the phosphonylated oxime, the presence of a minor abundance oxime-resistant conformation, and/or spontaneous reactivation of the phosphonylated conjugates.

Aging of the three  $S_p$ -phosphonate-conjugated Y337A mutants was examined by measuring the extent of reactivation with high HI-6 concentrations added at designated intervals after inhibition with the phosphonate and removal of excess inhibitor. Aging of  $S_p$ -isopropyl and  $S_p$ -3,3-dimethylbutyl methylphosphonyl Y337A conjugates was not detected over 36 h, while the aging rate constant of  $S_p$ -cycloheptyl methyl conjugated Y337A was  $0.005 \text{ min}^{-1}$ . This is faster than the reported aging rate constant of  $S_p$ -cycloheptyl methyl conjugated wild-type AChE ( $0.0004 \text{ min}^{-1}$ ; 18).

In a previous study it was shown that spontaneous reactivation of phosphonylated *Torpedo californica* AChE and human plasma BChE by cycloheptyl, isopropyl, and 3,3-dimethylbutyl methylphosphonyl thiocholine enantiomers

Table 1: Reactivation of Recombinant DNA-Derived Mouse Cholinesterases Phosphorylated with *S<sub>p</sub>*-Cycloheptyl Methylphosphonyl Thiocholine<sup>a</sup>

reactivator (mM)	enzyme	<i>k</i> <sub>+2</sub> (min <sup>-1</sup> )	<i>K</i> <sub>ox</sub> (mM)	<i>k</i> <sub>r</sub> (min <sup>-1</sup> M <sup>-1</sup> )	% react <sub>max</sub>	time
HI-6 (0.2–20)	AChE wt	0.60 ± 0.04	5.4 ± 0.8	112 ± 19	90	5 min
HI-6 (0.02–0.5)	Y337A			2000 ± 90	80	1 min
HI-6 (0.002–0.1)	F295L/Y337A			13180 ± 1414	80	3 min
HI-6 (0.01–5)	F297I/Y337A	6.0 ± 0.5	2.6 ± 0.4	2300 ± 400	100	1 min
HI-6 (0.2–10)	Y337A/F338A	0.051 ± 0.003	0.50 ± 0.12	102 ± 26	80	30 min
HI-6 (10)	F295L/F297I/Y337A <sup>b</sup>			≥24	80	20 min
HI-6 (1, 30)	BChE wt				<10	48 h
2-PAM (1–20)	AChE wt	0.0040 ± 0.0007	6.1 ± 3.0	0.66 ± 0.34	70	15 h
2-PAM (0.1–40)	Y337A	0.0025 ± 0.0001	0.62 ± 0.14	4.1 ± 1.0	80	5 h
2-PAM (0.4–20)	F295L/Y337A	0.016 ± 0.003	10 ± 3	1.7 ± 0.5	70	3 h
2-PAM (2–30)	F297I/Y337A	0.018 ± 0.002	2.7 ± 1.2	6.9 ± 3.3	70	2 h
2-PAM (1–60)	Y337A/F338A	0.00035 ± 0.00002	0.75 ± 0.45	0.47 ± 0.29	40	25 h
2-PAM (40)	F295L/F297I/Y337A <sup>b</sup>			≥0.12	100	5 h
2-PAM (5, 40)	BChE wt				<5	48 h

<sup>a</sup> Constants (±standard errors) are calculated (eqs 1–3) from *k*<sub>obs</sub> constants (8–16 values) obtained in two to seven experiments. The maximal percent of reactivation (% react<sub>max</sub>) measured within the specified time of the experiment is also given. <sup>b</sup> Only one *k*<sub>obs</sub> was determined (0.24 ± 0.04 min<sup>-1</sup> with HI-6 and 0.0048 ± 0.0011 min<sup>-1</sup> with 2-PAM).

Table 2: Reactivation of Recombinant DNA-Derived Mouse Cholinesterases Phosphorylated with *S<sub>p</sub>*-3,3-Dimethylbutyl Methylphosphonyl Thiocholine<sup>a</sup>

reactivator (mM)	enzyme	<i>k</i> <sub>+2</sub> (min <sup>-1</sup> )	<i>K</i> <sub>ox</sub> (mM)	<i>k</i> <sub>r</sub> (min <sup>-1</sup> M <sup>-1</sup> )	% react <sub>max</sub>	time
HI-6 (0.05–5)	AChE wt	0.39 ± 0.09	3.8 ± 1.8	102 ± 53	80	10 min
HI-6 (0.05–5)	Y337A	3.2 ± 0.5	2.8 ± 1.0	1200 ± 490	100	2 min
HI-6 (0.01–1)	F295L/Y337A			1300 ± 60	100	2 min
HI-6 (0.01–10)	F297I/Y337A	1.4 ± 0.1	1.9 ± 0.5	720 ± 180	100	5 min
HI-6 (1–40)	Y337A/F338A	0.10 ± 0.01	2.1 ± 1.2	47 ± 28	80	20 min
HI-6 (10)	F295L/F297I/Y337A <sup>b</sup>			≥31	80	10 min
HI-6 (0.5–20)	BChE wt	0.73 ± 0.14	7.1 ± 3.2	103 ± 51	100	10 min
2-PAM (1–40)	AChE wt			0.18 ± 0.01	90	8 h
2-PAM (5–40)	Y337A			0.041 ± 0.003	80	33 h
2-PAM (0.5–40)	F295L/Y337A	0.0018 ± 0.0002	2.8 ± 1.1	0.66 ± 0.27	90	25 h
2-PAM (10–60)	F297I/Y337A	0.0025 ± 0.0002	9.0 ± 3.6	0.27 ± 0.11	80	15 h
2-PAM (5–60)	Y337A/F338A	0.00023 ± 0.00001	0.54 ± 0.85	0.42 ± 0.65	60	70 h
2-PAM (40)	F295L/F297I/Y337A <sup>b</sup>			≥0.22	90	6 h
2-PAM (3–30)	BChE wt	0.028 ± 0.003	3.2 ± 1.7	8.7 ± 4.6	100	3 h

<sup>a</sup> Constants (±standard errors) are calculated (eqs 1–3) from *k*<sub>obs</sub> constants (5–15 values) obtained in two to four experiments. The maximal percent of reactivation (% react<sub>max</sub>) measured within the specified time of the experiment is also given. <sup>b</sup> Only one *k*<sub>obs</sub> was determined (0.31 ± 0.06 min<sup>-1</sup> with HI-6 and 0.0088 ± 0.0021 min<sup>-1</sup> with 2-PAM).

Table 3: Reactivation of Recombinant DNA-Derived Mouse Cholinesterases Phosphorylated with *S<sub>p</sub>*-Isopropyl Methylphosphonyl Thiocholine<sup>a</sup>

reactivator (mM)	enzyme	<i>k</i> <sub>+2</sub> (min <sup>-1</sup> )	<i>K</i> <sub>ox</sub> (mM)	<i>k</i> <sub>r</sub> (min <sup>-1</sup> M <sup>-1</sup> )	% react <sub>max</sub>	time (min)
HI-6 (0.05–1)	AChE wt	0.20 ± 0.03	0.15 ± 0.09	1330 ± 780	90	10
HI-6 (0.2–20)	Y337A	1.13 ± 0.08	4.7 ± 0.8	240 ± 47	100	2
HI-6 (0.5–30)	F295L/Y337A	0.27 ± 0.01	0.37 ± 0.09	730 ± 180	80	10
HI-6 (0.05–1)	F297I/Y337A	0.95 ± 0.13	0.41 ± 0.14	2330 ± 844	100	5
HI-6 (1–20)	Y337A/F338A	0.26 ± 0.02	1.5 ± 0.6	178 ± 74	90	15
HI-6 (0.05–5)	BChE wt	0.014 ± 0.001	0.064 ± 0.024	215 ± 70	80	90
2-PAM (0.1–10)	AChE wt	0.095 ± 0.013	0.088 ± 0.075	1080 ± 940	100	30
2-PAM (0.2–40)	Y337A	0.21 ± 0.01	2.6 ± 0.3	82 ± 11	80	20
2-PAM (1–40)	F295L/Y337A			3.5 ± 0.4	90	30
2-PAM (0.1–40)	F297I/Y337A	2.9 ± 0.2	5.5 ± 1.3	534 ± 133	90	1
2-PAM (1–40)	Y337A/F338A	0.072 ± 0.004	1.5 ± 0.5	46 ± 14	90	30
2-PAM (0.05–10)	BChE wt	2.98 ± 0.01	2.39 ± 0.02	1250 ± 9	90	1

<sup>a</sup> Constants (±standard errors) are calculated (eqs 1–3) from *k*<sub>obs</sub> constants (6–19 values) obtained in two to five experiments. The maximal percent of reactivation (% react<sub>max</sub>) measured within the specified time of the experiment is also given.

proceeded very slowly, if at all (rate constants less than 0.001 min<sup>-1</sup>) (23). In initial studies, we did not observe spontaneous reactivation with return of AChE activity in several of the methylphosphonyl conjugates studied as we have observed for the dimethyl, diethyl, and diisopropylphosphoryl conjugates of mouse AChE (24). The phosphonyl oxime (product of reactivation) could reinhibit the free enzyme (2, 25, 26),

but we have yet to identify the inhibitory potency and the stability of these reactivation products.

**Oxime Reactivation of the *S<sub>p</sub>*-Alkyl Methylphosphonylated Cholinesterases.** The kinetic parameters for reactivation of the *S<sub>p</sub>*-cycloheptyl, *S<sub>p</sub>*-3,3-dimethylbutyl, and *S<sub>p</sub>*-isopropyl methylphosphonylated cholinesterases by HI-6 and 2-PAM are presented in Tables 1–3. All *S<sub>p</sub>* conjugates were

Table 4: Reactivation of Recombinant DNA-Derived Mouse Cholinesterases Phosphorylated with  $R_p$ -Cycloheptyl Methylphosphonyl Thiocholine<sup>a</sup>

reactivator (mM)	enzyme	$k_{+2}$ (min <sup>-1</sup> )	$K_{ox}$ (mM)	$k_r$ (min <sup>-1</sup> M <sup>-1</sup> )	% react <sub>max</sub>	time (h)
HI-6 (1, 40)	AChE wt				<15	50
HI-6 (0.3–20)	Y337A	0.00042 ± 0.00002	1.0 ± 0.2	0.41 ± 0.06	50	85
HI-6 (1–30)	F295L/Y337A				<25	40
HI-6 (10–40)	F297I/Y337A				<25	72
HI-6 (0.2–2)	Y337A/F338A				<15	40
HI-6 (10–30)	BChE wt				<15	50
2-PAM (1, 40)	AChE wt				<25	50
2-PAM (0.3–5)	Y337A	0.00047 ± 0.00004	0.36 ± 0.16	1.3 ± 0.6	50	85
2-PAM (20–40)	F295L/Y337A				<25	40
2-PAM (5–40)	F297I/Y337A				<40	60
2-PAM (0.3–5)	Y337A/F338A	0.00040 ± 0.00010	0.99 ± 0.87	0.40 ± 0.37	40	20
2-PAM (20–40)	BChE wt			0.027 ± 0.001	70	25

<sup>a</sup> Constants (±standard errors) are calculated (eqs 1–3) from  $k_{obs}$  constants (4–8 values) obtained in one to three experiments. The maximal percent of reactivation (% react<sub>max</sub>) measured within the specified time of the experiment is also given.

Table 5: Reactivation of Recombinant DNA-Derived Mouse Cholinesterases Phosphorylated with  $R_p$ -3,3-Dimethylbutyl Methylphosphonyl Thiocholine<sup>a</sup>

reactivator (mM)	enzyme	$k_{+2}$ (min <sup>-1</sup> )	$K_{ox}$ (mM)	$k_r$ (min <sup>-1</sup> M <sup>-1</sup> )	% react <sub>max</sub>	time (h)
HI-6 (0.2–2)	AChE wt				<15	40
HI-6 (0.2–40)	Y337A	0.00040 ± 0.00002	0.54 ± 0.14	0.74 ± 0.19	70	35
HI-6 (1, 10)	F295L/Y337A				<25	60
HI-6 (10–40)	F297I/Y337A				<25	60
HI-6 (0.2–2)	Y337A/F338A	0.00014 ± 0.00001	0.076 ± 0.051	1.8 ± 1.2	50	40
HI-6 (1–10)	BChE wt				<25	50
2-PAM (0.3–5)	AChE wt				<15	40
2-PAM (0.5–5)	Y337A	0.0007 ± 0.0000	0.38 ± 0.08	1.8 ± 0.4	60	35
2-PAM (5, 30)	F295L/Y337A				<25	60
2-PAM (20–60)	F297I/Y337A				<25	60
2-PAM (0.3–5)	Y337A/F338A				<15	60
2-PAM (3–30)	BChE wt	0.0079 ± 0.0011	13 ± 4	0.62 ± 0.22	80	20

<sup>a</sup> Constants (±standard errors) are calculated (eqs 1–3) from  $k_{obs}$  constants (4–8 values) obtained in one or two experiments. The maximal percent of reactivation (% react<sub>max</sub>) measured within the specified time of the experiment is also given.

Table 6: Reactivation of Recombinant DNA-Derived Mouse Cholinesterases Phosphorylated with  $R_p$ -Isopropyl Methylphosphonyl Thiocholine<sup>a</sup>

reactivator (mM)	enzyme	$k_{+2}$ (min <sup>-1</sup> )	$K_{ox}$ (mM)	$k_r$ (min <sup>-1</sup> M <sup>-1</sup> )	% react <sub>max</sub>	time (h)
HI-6 (0.2–40)	AChE wt	0.0075 ± 0.0003	4.3 ± 0.7	1.7 ± 0.3	70	10
HI-6 (0.2–30)	Y337A	0.0071 ± 0.0004	0.97 ± 0.23	7.3 ± 1.8	80	8
HI-6 (1–30)	F295L/Y337A	0.0013 ± 0.0001	0.95 ± 0.56	1.3 ± 0.8	70	16
HI-6 (5–40)	F297I/Y337A	0.0021 ± 0.0003	16 ± 8	0.13 ± 0.07	50	16
HI-6 (1–30)	BChE wt	0.00035 ± 0.00004	1.1 ± 0.9	0.23 ± 0.25	40	25
2-PAM (0.3–40)	AChE wt	0.0029 ± 0.0004	1.9 ± 1.1	1.5 ± 0.9	70	20
2-PAM (0.3–40)	Y337A	0.0026 ± 0.0001	0.60 ± 0.21	4.3 ± 1.5	80	8
2-PAM (5–30)	F295L/Y337A	0.0096 ± 0.0039	10 ± 11	0.95 ± 1.09	80	10
2-PAM (5–60)	F297I/Y337A			0.041 ± 0.003	100	25
2-PAM (5–30)	BChE wt	0.024 ± 0.006	27 ± 13	0.88 ± 0.47	100	4

<sup>a</sup> Constants (±standard errors) are calculated (eqs 1–3) from  $k_{obs}$  constants (6–10 values) obtained in two to four experiments. The maximal percent of reactivation (% react<sub>max</sub>) measured within the specified time of the experiment is also given.

reactivated nearly completely with the exception of  $S_p$ -cycloheptyl methylphosphonylated BChE (cf. Table 1). The  $S_p$ -cycloheptyl methylphosphonylated F295L/F297I/Y337A mutant, structurally the most similar to BChE in substituted active center gorge residues, was reactivated between 80% and 100% by both oximes.

Reactivation of all  $S_p$ -phosphonylated AChE and mutant conjugates by HI-6 was appreciably faster than by 2-PAM. The difference in  $k_r$  between oximes is primarily dictated by the unimolecular reaction step,  $k_{+2}$ , which is more than 100-fold slower for 2-PAM than HI-6. Single or double substitutions involving F295L, F297I, and Y337A within the AChE gorge enhanced the  $k_r$  in reactivation of mutants phosphonylated with bulky methylphosphonates (cycloheptyl

and 3,3-dimethylbutyl; Tables 1 and 2), while only the F297I/Y337A double mutation enhanced reactivation of all three  $S_p$  conjugates. The greatest enhancement of  $k_r$  (about 120-fold) over the wild-type AChE was obtained in reactivation of  $S_p$ -cycloheptyl methylphosphonyl F295L/Y337A AChE by HI-6 (cf. Table 1); the determined  $k_r$  was the greatest for all reactions reported in this paper.

Both wild-type AChE and BChE phosphonylated with  $S_p$ -isopropyl methylphosphonate were reactivated by both oximes more rapidly (higher  $k_r$  value) than the wild-type enzymes phosphonylated by the more bulky  $S_p$ -3,3-dimethylbutyl and  $S_p$ -cycloheptyl methylphosphonates (cf. Table 3 vs Tables 1 and 2). Although  $k_r$  for 2-PAM reactivation of wild-type AChE and BChE was similar, the component  $K_{ox}$

and  $k_{+2}$  constants differed by 30-fold where phosphorylated AChE had a higher affinity (i.e., lower  $K_{ox}$ ) and lower  $k_{+2}$  for 2-PAM, and on the other hand, phosphorylated BChE had a higher maximum reactivation rate constant ( $k_{+2}$ ).

**Oxime Reactivation of the  $R_P$ -Alkyl Methylphosphonylated Cholinesterases.** Tables 4–6 present results for reactivation of the  $R_P$ -cycloheptyl,  $R_P$ -3,3-dimethylbutyl, and  $R_P$ -isopropyl methylphosphonylated enzymes. HI-6 and 2-PAM showed similar but low reactivation efficiency (from 34 conjugates only 18 were reactivated). For the bulky  $R_P$ -cycloheptyl (Table 4) and  $R_P$ -3,3-dimethylbutyl (Table 5) methylphosphonylated wild-type AChE reactivation was not evident with either HI-6 or 2-PAM, while the corresponding BChE conjugates were reactivated by 2-PAM nearly completely albeit at slow rates. Hence, 2-PAM reactivation showed an inverted stereoselectivity for the cycloheptyl methylphosphonyl BChE conjugate: the  $S_P$  conjugate was resistant to reactivation (cf. Table 1), while the  $R_P$  conjugate was reactivated.

Reactivation kinetics of mouse single residue mutants of AChE conjugated with these methylphosphonates was previously studied by Wong et al. (18). Data given in the present paper agree with the reported results except for the reactivation of wild-type AChE conjugated with  $R_P$ -3,3-dimethylbutyl methylphosphonate (Table 5). In the present experiments this conjugate was found not to be reactivatable, while in previous experiments substantial reactivation was observed by both oximes (18). In the previous study inhibition was carried out at a 14-fold excess of organophosphate, on average (range of 4-fold to 22-fold), and inhibition by a minor abundance of the  $S_P$  contaminant may have predominated under this condition. This situation was avoided in the current studies by using inhibitors in only 10% stoichiometric excess.

Reactivation rates of the less bulky  $R_P$ -isopropyl methylphosphonylated enzymes presented in Table 6 were generally more rapid than the conjugates phosphorylated with the larger two  $R_P$ -phosphonates. The highest bimolecular reactivation rate for the  $R_P$  conjugate of Y337A was  $7.3 \text{ min}^{-1} \text{ M}^{-1}$  for HI-6 and  $4.3 \text{ min}^{-1} \text{ M}^{-1}$  for 2-PAM. Comparing these reactivation rates with the rates of  $R_P$ -Y337A conjugates in Tables 4 and 6, it follows that  $R_P$ -isopropyl methylphosphonylated Y337A had the highest  $k_{+2}$  value. The Y337A mutation coupled with F338A also showed appreciable rates of reactivation of  $R_P$ -cycloheptyl methylphosphonyl Y337A/F338A AChE by 2-PAM and  $R_P$ -3,3-dimethylbutyl methylphosphonyl Y337A/F338A AChE by HI-6, but reactivation was not complete.

**Molecular Modeling.** Models of the reversible Michaelis-type complexes (Figure 3; [EP][OX] in Scheme 1) between HI-6 and either  $S_P$ -cycloheptyl methylphosphonylated wild-type mouse AChE or F295L/Y337A mouse AChE resulting from molecular dynamics calculation indicate that, with the wild-type enzyme, HI-6 can assume only one distinct productive orientation with the slender molecule extended through the narrow gorge (Figure 3B). Within the enlarged gorge of the F295L/Y337A mutant AChE additional orientations appear likely. The HI-6 chain coils back into the enlarged choline binding site where the nonreactive carbamoyl pyridinium moiety is stabilized (cf. Figure 3A,C). The distance between the oxime oxygen and the phosphorus in wild-type conformations ( $4.2 \pm 1.0 \text{ \AA}$ ,  $n = 20$ ) and mutant

gorge conformations ( $4.5 \pm 0.9 \text{ \AA}$ ,  $n = 20$ ) appeared very similar and consistent with distances found for similar oxime–AChE complex models obtained by other authors (about  $4.4 \text{ \AA}$  measured for the structure deposited by Pang et al.: PDB accession codes 1JGA and 1JGB; 27).

## DISCUSSION

Reactivation by the two oximes demonstrates the superiority of HI-6 over 2-PAM for reactivation of wild-type AChE and mutant  $S_P$ -phosphonate conjugates. Moreover, the enzyme conjugates showed a high degree of stereoselectivity for HI-6 reactivation, with preference of  $S_P$  over  $R_P$  enantiomers. Taken together with previous findings on organophosphate inactivation (9, 10, 13) and reactivation (18, 25, 28), oxime-mediated reactivation is governed by several principles.

Similar to inhibition by phosphonates, reactivation efficiency is enhanced by phosphonyl oxygen insertion into the oxyanion hole in the presumed transition state. Owing to the spatial constraints of the acyl pocket, the bulky  $R_P$ -methylphosphonates cannot achieve optimal positioning of alkoxy groups without distortion of structure. Accordingly, just as the  $R_P$  inhibitors react far more slowly with AChE (9, 10, 13), they are either resistant to reactivation or reactivate slowly (18). For  $R_P$  conjugates suboptimal positioning of the phosphonyl oxygen in the oxyanion hole and limitations on oxime access to the phosphonate both slow reactivation rates. However, a single mutation of the choline binding site, Y337A, enabled reactivation of the  $R_P$  conjugates. Reactivation was increased presumably because of an improved clearance in the formation of the pentacoordinate transition state and the reduction in steric constraints around residue 337. The tetrahedral phosphonate may move slightly toward the vacant area created by removal of the aromatic side chain at position 337, allowing a more favorable angle of oxime attack.

The spatial constraints of the gorge give rise to a dimensionally impacted organophosphate with a limited angle of access for the attacking nucleophile. Our previous studies of acyl pocket mutations suggest a nucleophilic attack route to the phosphorus atom coming from the acyl pocket direction (18). We show in this paper that enhancing clearance in the vicinity of Y337 has an influence on reactivation rates. Indeed, the double mutation involving F295 and Y337 yields the greatest rate enhancement. This suggests that the route of oxime attack still occurs from the acyl pocket side, but the tethered phosphonate is able to adopt an exposed position more amenable to attack, or new orientations of the attacking oxime allowed by the vacant area created near residue 337 optimize the attack angle.

The likely position of HI-6 in the mutant F295L/Y337A for the attack on phosphorylated serine is shown in Figure 3A. Simply opening the AChE choline binding site in all dimensions to enhance access of the oxime group to the phosphorus atom is not sufficient to increase reactivation. Additional substitution by F338A leading to a more open gorge appeared counterproductive for reactivation (cf. Table 1). Certain aromatic residues may be required in order to stabilize the oxime in the proper orientation between F338 and F297 as shown in Figure 3. Hence, reactivation of  $S_P$ -cycloheptyl methylphosphonyl Y337A/F338A conjugate was

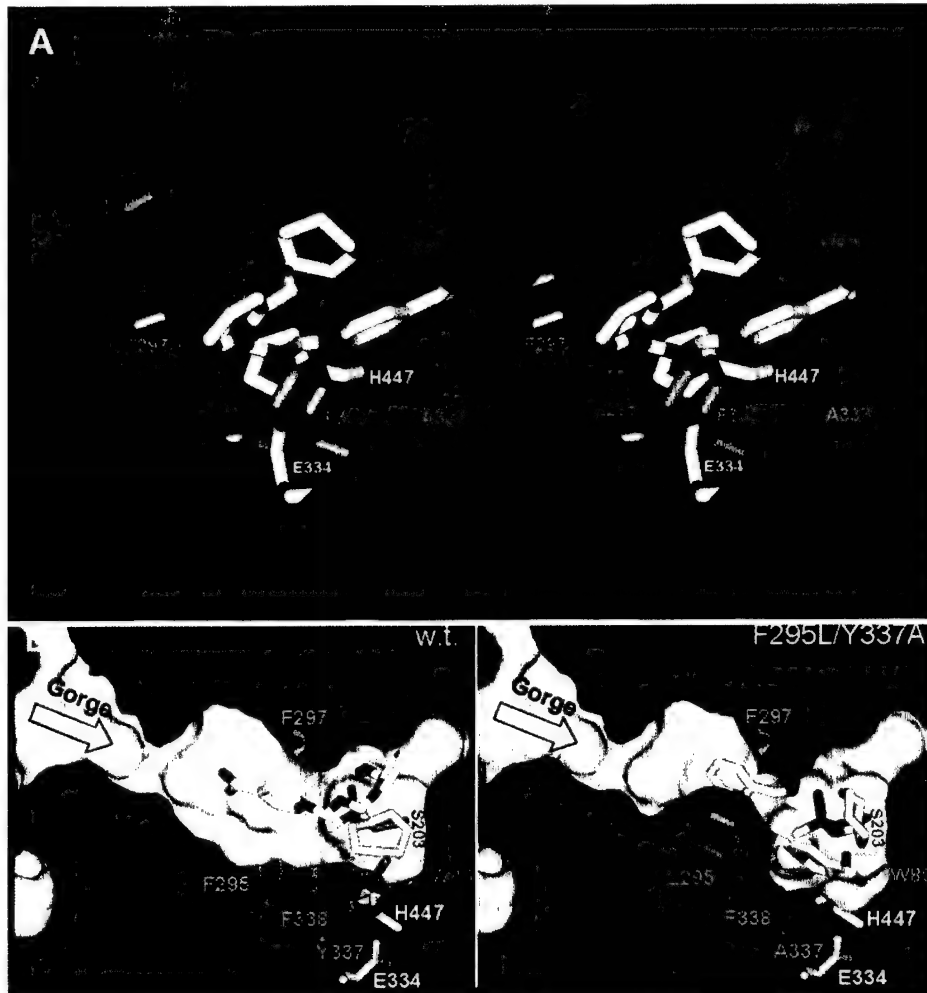


**FIGURE 3:** (A) Stereo image of an energy-minimized HI-6 conformation (carbon atoms in yellow, nitrogen in blue, oxygen in red) in the F295L/Y337A mouse AChE (in blue ribbon)  $S_P$ -cycloheptyl methylphosphonylated active center gorge. The active center is viewed through the gorge opening. The lowest energy conformer is shown, out of a cluster of 20 similar resulting conformations. The dotted white line indicates the direction of nucleophilic attack of HI-6. Only selected AChE residues are displayed in blue, white (catalytic triad), and orange (residues mutated in this study). (B, C) Cutaway diagrams at identical angles of the HI-6 complex with wild-type mouse AChE (panel B) and in the F295L/Y337A mutant mouse AChE (panel C). The AChE represented by Connolly solvent-accessible surface was cut approximately in half to reveal the position, size, and depth of the active center gorge in the wild-type and mutant AChE. The orange arrow indicates the position of the F297 side chain hidden behind a surface.

not as efficient as was reactivation of the F295L/Y337A conjugate.

While opening of the gorge can greatly enhance oxime efficacy, a gorge devoid of critical aromatic residues or a tethered phosphonate with many degrees of freedom and torsional movement, as found for BChe, yields an environment not conducive to efficient reactivation by HI-6, whereas reactivation by the smaller, but less efficient, 2-PAM molecule is less influenced by this difference. Hence, efficacy of oximes is dependent not only on the oxime structure but also on the position of the conjugated phosphorus residue. Attack by the oxime is believed to proceed through a pentavalent (trigonal bipyramidal) intermediate and formation of the phosphorylated oxime. Both 2-PAM and HI-6 have their oxime groups in the *ortho* position to the cationic pyridinium nitrogen, and their attacking orientations should have distinctive steric constraints. Hence, the inability of 2-PAM and HI-6 to cause reactivation of certain conjugates, particularly  $R_P$  conjugates, may not prevail for all oximes. Obidoxime and TMB-4, two symmetric dioximes with oxime

groups *para* to the pyridinium ring, reactivate  $R_P$  conjugates to near completion although at very slow rates (18, 23). Fortunately, the  $R_P$  enantiomers that are resistant to oxime reactivation are also less reactive as phosphorylation agents (9, 10, 13). Hence, they will be the less reactive and toxic of the chiral pair.

A practical outgrowth of these studies is the application of mutant AChE–oxime combinations to catalyze the hydrolysis of organophosphates both in vitro and in vivo. Cholinesterases in the plasma are efficient scavengers of organophosphates in terms of reactivity; however, their capacity is limited by virtue of the 1:1 stoichiometry between the small organophosphate (100–200 Da) and the ~70 kDa subunit bearing the catalytic serine. Hence, an enzyme–reactivator combination catalytic to the organophosphate hydrolysis, rather than stoichiometric to conjugation, would greatly reduce doses needed for scavenging.

Lockridge et al. (17) generated mutations in butyrylcholinesterase that catalyze the hydrolysis of organophosphates. However, mutations that enable organophosphate turnover

also compromise its capacity to react initially with the organophosphate, thus limiting the potential of butyrylcholinesterase in vivo. By contrast, the mutations described here that enhance oxime reactivation react efficiently with the methylphosphonates as described previously (13), and the limitations in scavenging capacity then depend on efficiency of the oxime to continually regenerate active AChE. By enhancing the rate some 120-fold, we approach a range where scavenging efficiency has a practical outcome. Efficiency of scavenging is also a pharmacokinetic consideration since the introduced organophosphate must be scavenged in the plasma before it distributes into extracellular space and/or accesses the blood-brain barrier. As shown here, the enhanced scavenging capacity is manifested to the greatest extent in those bulky  $S_p$  enantiomers that are most intractable to reactivation. Of the offending methylphosphonates, cyclosarin and soman would fall into this category.

## REFERENCES

1. Chambers, H. W. (1992) Organophosphorus compounds: An Overview, in *Organophosphates: Chemistry, Fate, and Metabolism* (Chambers, J. E., and Levi, P. E., Eds.) pp 3–17, Academic Press, San Diego, CA.
2. Wilson, I. B., and Ginsburg, S. (1955) A powerful reactivator of alkylphosphate-inhibited acetylcholinesterase, *Biochim. Biophys. Acta* 18, 168–170.
3. Froede, H. C., and Wilson, I. B. (1971) Acetylcholinesterase, in *The Enzymes* (Boyer, P. D., Ed.) 3rd ed., Vol. 5, pp 87–114, Academic Press, New York and London.
4. Flanagan, J., and Jones, A. L. (2001) *Antidotes*, pp 245–267, Taylor and Francis, London and New York.
5. Sussman, J. L., Harel, M., Frolow, F., Oefner, C., Goldman, A., Toker, L., and Silman, I. (1991) Atomic structure of acetylcholinesterase from *Torpedo californica*: A prototypic acetylcholine-binding protein, *Science* 253, 872–897.
6. Bourne, Y., Taylor, P., and Marchot, P. (1995) Acetylcholinesterase inhibition by fasciculin: crystal structure of the complex, *Cell* 83, 503–512.
7. Kryger, G., Harel, M., Giles, K., Toker, L., Velan, B., Lazar, A., Kronman, C., Barak, D., Ariel, N., Shafferman, A., Silman, I., and Sussman, J. L. (2000) Three-dimensional structure of a complex of E2020 with acetylcholinesterase from *Torpedo californica*, *Acta Crystallogr., Sect. D* 56, 1385–1394.
8. Berman, H. A., and Leonard, K. (1989) Chiral reactions of acetylcholinesterase probed with enantiomeric methylphosphonothioates, *J. Biol. Chem.* 264, 3942–3950.
9. Hosea, N. A., Berman, H. A., and Taylor, P. (1995) Specificity and orientation of trigonal carboxylesters and tetrahedral phosphonylestes in cholinesterase, *Biochemistry* 34, 11528–11536.
10. Hosea, N. A., Radić, Z., Tsigelny, I., Berman, H. A., Quinn, D. M., and Taylor, P. (1996) Aspartate 74 as a primary determinant in acetylcholinesterase governing specificity to cationic organophosphates, *Biochemistry* 35, 10995–11004.
11. Taylor, P., Hosea, N. A., Tsigelny, I., Radić, Z., and Berman, H. A. (1997) Determining ligand orientation and transphosphorylation mechanism on acetylcholinesterase by  $R_p$ ,  $S_p$  enantiomer selectivity and site-specific mutagenesis, *Enantiomer* 2, 249–260.
12. Ordentlich, A., Barak, D., Kronman, C., Benschop, H. P., De Jong, L. P. A., Ariel, N., Barak, R., Segall, Y., Velan, B., and Shafferman, A. (1999) Dissection of the human acetylcholinesterase active center determinants of substrate specificity—Identification of residues constituting the anionic site, the hydrophobic site, and the acyl pocket, *Biochemistry* 38, 3055–3066.
13. Kovarik, Z., Radić, Z., Berman, H. A., Simeon-Rudolf, V., Reiner, E., and Taylor, P. (2003) Acetylcholinesterase active centre and gorge conformations analysed by combinatorial mutations and enantiomeric phosphonates, *Biochem. J.* 373, 33–40.
14. Ashani, Y., Radić, Z., Tsigelny, I., Vellom, D. C., Pickering, N., Quinn, D. M., Doctor, B. P., and Taylor, P. (1995) Amino acid residues controlling reactivation of organophosphonyl conjugates of acetylcholinesterase by mono- and bisquaternary oximes, *J. Biol. Chem.* 270, 6370–6380.
15. Grosfeld, H., Barak, D., Ordentlich, A., Velan, B., and Shafferman, A. (1996) Interactions of oxime reactivators with diethylphosphoryl adducts of human acetylcholinesterase and its mutant derivatives, *Mol. Pharmacol.* 50, 639–649.
16. Masson, P., Froment, M.-T., Bartels, C. F., and Lockridge, O. (1997) Importance of aspartate-70 in organophosphate inhibition, oxime re-activation and aging of human butyrylcholinesterase, *Biochem. J.* 325, 53–61.
17. Lockridge, O., Blong, R. M., Masson, P., Froment, M.-T., Millard, C. B., and Broomfield, C. A. (1997) A single amino acid substitution, Gly117His, confers phosphotriesterase (organophosphorus acid anhydride hydrolase) activity on human butyrylcholinesterase, *Biochemistry* 36, 786–795.
18. Wong, L., Radić, Z., Brüggemann, R. J. M., Hosea, N., Berman, H. A., and Taylor, P. (2000) Mechanism of oxime reactivation of acetylcholinesterase analyzed by chirality and mutagenesis, *Biochemistry* 39, 5750–5757.
19. Radić, Z., Pickering, N. A., Vellom, D. C., Camp, S., and Taylor, P. (1993) Three distinct domains in the cholinesterase molecule confer selectivity for acetylcholinesterase and butyrylcholinesterase inhibitors, *Biochemistry* 32, 12074–12084.
20. Ordentlich, A., Barak, D., Kronman, C., Flashner, Y., Leitner, M., Segall, Y., Ariel, N., Cohen, S., Velan, B., and Shafferman, A. (1993) Dissection of the human acetylcholinesterase active center determinants of substrate specificity—Identification of residues constituting the anionic site, the hydrophobic site, and the acyl pocket, *J. Biol. Chem.* 268, 17083–17095.
21. Marchot, P., Ravelli, R. B. G., Raves, M. L., Bourne, Y., Vellom, D. C., Kanter, J., Camp, S., Sussman, J. L., and Taylor, P. (1996) Soluble monomeric acetylcholinesterase from mouse—expression, purification, and crystallization in complex with fasciculin, *Protein Sci.* 5, 672–679.
22. Ellman, G. L., Courtney, K. D., Andres, V., Jr., and Featherstone, R. M. (1961) A new and rapid colorimetric determination of acetylcholinesterase activity, *Biochem. Pharmacol.* 7, 88–95.
23. Berman, H. A. (1998) A view from the gorge. Reactivation and importance of water, in *Structure and Function of Cholinesterases and Related Proteins* (Doctor, B. P., Taylor, P., Quinn, D. M., Rotundo, R. L., and Gentry, M. K., Eds.) pp 413–417, Plenum Press, New York and London.
24. Jennings, L. L., Malecki, M., Komives, E. A., and Taylor, P. (2003) Direct analysis of the kinetic profiles of organophosphate-acetylcholinesterase adducts by MALDI-TOF mass spectrometry, *Biochemistry* 42, 11083–11091.
25. Luo, C., Saxena, A., Smith, M., Garcia, G., Radić, Z., Taylor, P., and Doctor, B. P. (1999) Phosphoryl oxime inhibition of acetylcholinesterase during oxime reactivation is prevented by edrophonium, *Biochemistry* 38, 9937–9947.
26. Ashani, Y., Bhattacharjee, A. K., Leader, H., Saxena, A., and Doctor, B. P. (2003) Inhibition of cholinesterase with cationic phosphonyl oximes highlights distinctive properties of the charged pyridine groups of quaternary oxime reactivators, *Biochem. Pharmacol.* 33, 191–202.
27. Pang, Y.-P., Kollmeyer, T. M., Hong, F., Lee, J.-C., Hammond, P. I., Haugabouk, S. P., and Brimijoin, S. (2003) Rational design of alkylene-linked bis-pyridiniumaldoximes as improved acetylcholinesterase reactivators, *Chem. Biol.* 10, 491–502.
28. Luo, C., Leader, H., Radić, Z., Maxwell, D. M., Taylor, P., Doctor, B. P., and Saxena, A. (2003) Two possible orientations of the HI-6 molecule in the reactivation of organophosphate-inhibited acetylcholinesterase, *Biochem. Pharmacol.* 66, 387–392.

## Nanosecond Dynamics of the Mouse Acetylcholinesterase Cys<sup>69</sup>-Cys<sup>96</sup> Omega Loop\*

Received for publication, April 9, 2003, and in revised form, May 16, 2003  
Published, JBC Papers in Press, May 19, 2003, DOI 10.1074/jbc.M303730200

Jianxin Shi<sup>†‡§</sup>, Kaihsu Tai<sup>†¶</sup>, J. Andrew McCammon<sup>¶</sup>, Palmer Taylor<sup>†\*\*</sup>, and David A. Johnson<sup>†‡</sup>

From the <sup>†</sup>Department of Pharmacology, University of California, San Diego, La Jolla, California 92093-0636, <sup>¶</sup>Howard Hughes Medical Institute and Departments of Pharmacology and of Chemistry and Biochemistry, University of California, San Diego, La Jolla, California 92093-0365, and <sup>‡</sup>Division of Biomedical Sciences, University of California, Riverside, California 92521-0121

The paradox of high substrate turnover occurring within the confines of a deep, narrow gorge through which acetylcholine must traverse to reach the catalytic site of acetylcholinesterase has suggested the existence of transient gorge enlargements that would enhance substrate accessibility. To establish a foundation for the experimental study of transient fluctuations in structure, site-directed labeling in conjunction with time-resolved fluorescence anisotropy were utilized to assess the possible involvement of the omega loop ( $\Omega$  loop), a segment that forms the outer wall of the gorge. Specifically, the flexibility of three residues (L76C, E81C, and E84C) in the Cys<sup>69</sup>-Cys<sup>96</sup>  $\Omega$  loop and one residue (Y124C) across the gorge from the  $\Omega$  loop were studied in the absence and presence of two inhibitors of different size, fasciculin and huperzine. Additionally, to validate the approach molecular dynamics was employed to simulate anisotropy decay of the side chains. The results show that the  $\Omega$  loop residues are significantly more mobile than the non-loop residue facing the interior of the gorge. Moreover, fasciculin, which binds at the mouth of the gorge, well removed from the active site, decreases the mobility of 5-(((2-acetyl)amino)ethyl)amino)naphthalene-1-sulfonic acid reporter groups attached to L76C and Y124C but increases the mobility of the reporter groups attached to E81C and E84C. Huperzine, which binds at the base of active-site gorge, has no effect on the mobility of reporter groups attached to L76C and Y124C but increases the mobility of the reporter groups attached to E81C and E84C. Besides showing that fluctuations of the  $\Omega$  loop residues are not tightly coupled, the results indicate that residues in the  $\Omega$  loop exhibit distinctive conformational fluctuations and therefore are likely to contribute to transient gorge enlargements in the non-ligated enzyme.

Acetylcholinesterase (AChE),<sup>1</sup> ranking among the most catalytically efficient enzymes known, catalyzes the hydrolysis of the neurotransmitter acetylcholine with a turnover number of  $10^4$  s<sup>-1</sup> (1, 2). Curiously, catalysis shows high efficiency despite the cross-sectional dimension of acetylcholine is nearly equal to the width of the narrowest portion of the 20-Å-long and tortuous gorge leading to the catalytic center (Fig. 1A) (3–7). This paradox suggests the existence of an enlarged solution conformational state(s) of the active-center gorge. Molecular dynamics simulations support the existence of breathing or gating motions that could enhance substrate accessibility to the active site (8–10).

One segment of the gorge that may play a major role in gorge enlargement is the large  $\Omega$  loop (defined by the Cys<sup>69</sup>-Cys<sup>96</sup> disulfide bond) that corresponds to the activation loop (Cys<sup>60</sup>-Cys<sup>97</sup>) of *Candida rugosa* lipase, a related carboxy esterase with an  $\alpha,\beta$ -hydrolase fold (11, 12). X-ray crystallographic analysis of the apo form of this lipase shows the activation loop occluding the active site in the absence of substrate and folding backward allowing substrate access when lipid is bound. We previously demonstrated by examining the steady-state emission from selective acrylodan-labeled side chains that AChE-inhibitor binding induces distinctive conformational changes in certain regions of the mouse AChE Cys<sup>69</sup>-Cys<sup>96</sup>  $\Omega$  loop (13).

To determine whether the Cys<sup>69</sup>-Cys<sup>96</sup>  $\Omega$  loop could contribute to gorge enlargement, we used site-directed labeling with IAEDANS at various positions in conjunction with time-resolved fluorescence anisotropy to compare the backbone flexibility of three residues in the  $\Omega$  loop (L76C, E81C, and E84C) with the flexibility of a residue in the active-site gorge, but not part of the  $\Omega$  loop (Y124C). We also examined the influence of two inhibitors on conformational flexibility, one of which interacts directly with the  $\Omega$  loop at the gorge entry (fasciculin), whereas the other (huperzine) associates with side chains of the loop near the gorge base. IAEDANS replaced acrylodan in this study, because it is conjugated more readily to active-site gorge residues than thioactive fluorescein derivatives, and because its relatively long emission lifetime allows better resolution of whole body from local depolarization processes. Additionally, molecular dynamics simulations of side chain motions of the four individual residues where cysteine was substituted showed agreement with anisotropy decay parameters of the wild type (wt) enzyme. We found that the conjugated  $\Omega$  loop residues were significantly more flexible than the non-

\* This work was supported in part by the United States Public Health Service Grants R37-GM18360 and P42-ES10337, by Department of Army Medical Defense Grant 17C-1-8014 (to P. T.), by the National Science Foundation, the National Institutes of Health, San Diego Supercomputer Center and National Biomedical Computational Resource, the W. M. Keck Foundation, and Accelrys Inc. (to J. A. McC.). The costs of publication of this article were defrayed in part by the payment of page charges. This article must therefore be hereby marked "advertisement" in accordance with 18 U.S.C. Section 1734 solely to indicate this fact.

† Predoctoral fellow supported by National Institutes of Health Grant T32-GM07752.

‡ Predoctoral fellow of the La Jolla Interfaces in Science Training Program and supported by the Burroughs Wellcome Fund.

\*\* To whom correspondence should be addressed: Dept. of Pharmacology, University of California, San Diego, La Jolla, CA 92093-0636. E-mail: pwtaylor@ucsd.edu.

<sup>1</sup> The abbreviations used are: AChE, acetylcholinesterase; mAChE, mouse acetylcholinesterase; acrylodan, 6-acryloyl-2-dimethylaminonaphthalene; IAEDANS, 5-(((2-iodoacetyl)amino)ethyl)amino)naphthalene-1-sulfonic acid; AEDANS, 5(((acetyl)amino)ethyl)amino)naphthalene-1-sulfonic acid; wt, wild type; PDB, protein data bank; wt, wild type.

TABLE I  
Effect of huperzine and fasciculin on steady-state emission parameters of IAEDANS-labeled mouse AChE

Data are shown as mean values of at least three determinations.

Mutant	Emission maxima (nm) <sup>a</sup>			Relative quantum yield <sup>b</sup>	
	Control	Huperzine	Fasciculin	Huperzine	Fasciculin
L76C	485	485	478	1.0	1.11
E81C	489	494	492	0.82	0.90
E84C	484	491	486	0.77	0.97
Y124C	482	482	469	1.0	1.55

<sup>a</sup> The excitation wavelength was 340 nm.

<sup>b</sup> Relative quantum yields were determined by comparison of areas under the emission spectra of each labeled mutant in the absence of ligand with its spectra in the presence of the indicated ligand. Concentrations of fasciculin and huperzine were 1.3 and 4  $\mu$ M, respectively.

loop residue. Also, the effects of the inhibitors were consistent with the flexibility of the  $\Omega$  loop contributing to transient gorge enlargement that could enhance substrate accessibility and product egress.

#### EXPERIMENTAL PROCEDURES

**Materials**—Acetylthiocholine iodide, 5,5'-dithiobis(2-nitrobenzoic acid) (Ellman's reagent), and dithiothreitol were purchased from Sigma. (−)-Huperzine A was purchased from Calbiochem. 5-(((2-Iodoacetyl)amino)ethyl)amino)naphthalene-1-sulfonic acid (IAEDANS) was obtained from Molecular Probes (Eugene OR). Fasciculin 2 (purified from the venom of *Dendroaspis angusticeps*) was a gift of Dr. Pascale Marchot (University of Marseille, France). Drs. Yacov Ashani and Bhupendra P. Doctor (Walter Reed Army Research Center, Washington, D. C.) kindly provided procainamide-linked Sepharose CL-4B resin. All other chemicals were of the highest grade commercially available.

**Expression, Mutagenesis, and Purification of mAChE**—Mouse AChE was produced by transfection of expression plasmid (pcDNA3, Invitrogen) containing an encoding cDNA where the AChE sequence was terminated at position 548. The plasmid was transfected into human embryonic kidney (HEK293) cells. Cells were selected with G418 to obtain stable producing cell lines, and AChE was expressed as a secreted soluble enzyme in serum-free media. Mutant enzymes were generated by standard mutagenesis procedures, and cassettes containing the mutation were subcloned into pcDNA3. Nucleotide sequences of the cassettes were confirmed by double-stranded sequencing to ensure that spurious mutations were not introduced into the coding sequence. Affinity chromatography using (m-aminophenyl) trimethyl ammonium linked through a long chain to Sepharose CL-4B resin (Sigma) permitted one-step purification of L76C, E81C, and E84C mAChE. Procainamide-linked Sepharose CL-4B resin was utilized in the purification of Y124C mAChE. From 4 to 6 liters of media, mutant and wild type enzyme were purified in quantities ranging between 5 and 25 mg (14). Purity was ascertained by SDS-PAGE and by measurements of specific activity.

**IAEDANS Labeling**—Mutant and wt enzymes were pretreated with 0.25 mM dithiothreitol for 30 min at room temperature to ensure the introduced cysteine was in a reduced state. Dithiothreitol was removed by use of a G-50 Sephadex spin column (Roche Applied Science) equilibrated in 10 mM Tris, 100 mM NaCl, 40 mM MgCl<sub>2</sub>, pH 8.0. IAEDANS (1  $\mu$ l) at 100 times the enzyme concentration was slowly mixed with the enzyme to achieve approximately a 10-fold molar excess of IAEDANS to enzyme. Labeling was allowed to proceed for 12–16 h at 4 °C, and excess reagent was removed by fractionation on a Sephadex G-25 (Amersham Biosciences) column equilibrated with 0.1 M sodium phosphate buffer, pH 7. Enzyme concentrations were determined from absorbance at 280 nm,  $\epsilon = 1.14 \times 10^5 \text{ M}^{-1} \text{ cm}^{-1}$  (14). Labeling stoichiometries were determined to be close to 1.0 from the ratio of absorption at 340 to 280 nm for the labeled enzymes. Because the absorption peak wavelength of IAEDANS at 340 nm,  $\epsilon = 5.7 \times 10^3 \text{ M}^{-1} \text{ cm}^{-1}$ , is close to that for the protein, these ratios only provide rough estimates of labeling. Specificity of labeling was assessed by comparison of areas under the fluorescence emission curves for IAEDANS-treated mutant with wild type enzymes.

**Steady-state Emission Spectra**—Steady-state emission spectra were measured at room temperature using a Jobin Yvon/Spex FluoroMax II spectrophotometer (Instrument S.A., Inc., Edison, NJ) with the excitation and emission bandwidths set at 5 nm.

**Time-resolved Fluorescence Anisotropy**—Time-resolved emission anisotropy was monitored on time-correlated single photon-counting instrument. Its custom-built fabrication included an IBH (Edinburgh,

UK) UV-NanoLED™ flash lamp run at 1 MHz and an IBH model TBX-04 photon detector. Vertically ( $I_{\parallel}(t)$ ) and orthogonally ( $I_{\perp}(t)$ ) polarized emission components were collected by exciting samples with vertically polarized light while orienting the emission polarizer (Polaroid HNP'B dichroic film) in either a vertical or orthogonal direction. Excitation and emission bands were selected with a Corning 7-60 interference filter and a Schott KV-450 nm cut-on filter, respectively. Typically,  $2 \times 10^4$  peak counts were collected in 1–2 min when the emission polarizer was vertically oriented. The orthogonal emission decay profile was generated over the same time interval used to generate the vertical emission decay profile. Samples were held at 22 °C. To minimize convolution artifacts, flash lamp profiles were recorded by removing the emission filter and monitoring light scatter from a suspension of latex beads. The data analysis software corrected the wavelength-dependent temporal dispersion of the photoelectrons by the photomultiplier. The polarization bias ( $G$ ) of the detection instrumentation was determined by measuring the integrated photon counts/ $6 \times 10^6$  lamp flashes that were detected while the samples were excited with orthogonally polarized light and the mission monitored with a polarizer oriented in the vertical and orthogonal direction ( $G = 0.9936$ ).

Emission anisotropy,  $r(t)$ , is given by the expression shown in Equation 1,

$$r(t) = \frac{I_{\parallel}(t) - G \cdot I_{\perp}(t)}{I_{\parallel}(t) + 2G \cdot I_{\perp}(t)} \quad (\text{Eq. 1})$$

From this and the expression for the total emission,  $S(t)$ , for a macroscopically isotropic sample,

$$S(t) = I_{\parallel}(t) + 2G \cdot I_{\perp}(t) \quad (\text{Eq. 2})$$

was deconvolved simultaneously from the individual polarized emission components expressed as shown in Equations 3 and 4,

$$I_{\parallel}(t) = \frac{S(t)}{3} (1 + 2r(t)) \quad (\text{Eq. 3})$$

and

$$I_{\perp}(t) = \frac{S(t)}{3} (1 - r(t)) \quad (\text{Eq. 4})$$

Thus, both  $I_{\parallel}(t)$  and  $I_{\perp}(t)$  were determined by the same fitting functions,  $S(t)$  and  $r(t)$ , and fitting parameters.

Fluorescence lifetimes were determined by initially generating a total emission profile from  $I_{\parallel}(t)$  and  $I_{\perp}(t)$  with Equation 2, and then fitting this decay profile to a biexponential decay expression with the Globals Unlimited™ (Laboratory for Fluorescence Dynamics, Urbana, IL) software package. The resulting lifetimes were entered and fixed in the second step of the analysis process where  $I_{\parallel}(t)$  and  $I_{\perp}(t)$  were simultaneously analyzed for the parameters of  $S(t)$  and  $r(t)$  with the Globals Unlimited™ program. Here  $r(t)$  is a nonassociative anisotropy decay function as shown in Equation 5.

$$r(t) = r_0 f_{xb} \exp(-t/\phi_{fast}) + r_0 (1 - f_{xb}) \exp(-t/\phi_{slow}) \quad (\text{Eq. 5})$$

where  $r_0$  is the amplitude of the anisotropy at time 0;  $f_{xb}$  is the fraction of the anisotropy decay associated with the fast decay processes, and  $\phi$  is rotational correlation time of the anisotropy decay. Rotational correlation times are measured for the two (fast and slow) processes. This nonassociative model assumes that the rotational correlation times are common to each of the emission relaxation times. Goodness of fit was evaluated from the value of  $\chi^2$  and visual inspection of the difference between the experimental data and the empirical anisotropy decay

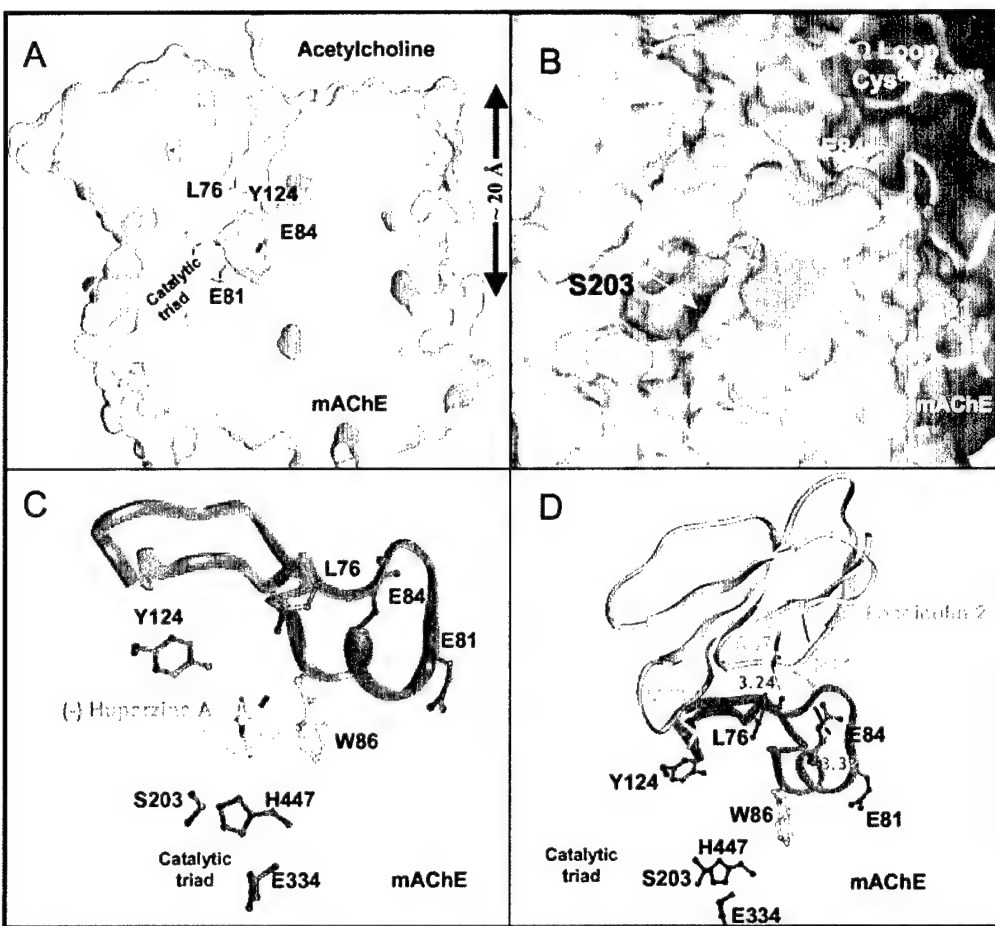


**FIG. 1. Locations of substituted cysteines for fluorophore conjugation.** *A*, cutaway view of mAChE crystallographic structure showing an active-site gorge 20 Å in depth (PDB code 1MAA). The view is taken from the side with catalytic triad (Ser<sup>203</sup>, Glu<sup>334</sup>, and His<sup>447</sup>) on the bottom left. *B*, Connolly surface presentation of mAChE looking into the gorge entry with catalytic serine highlighted in red at its base. Residues 76, 81, and 84 displayed in blue are at the tip (76) and outer portion (81, 84) of the Cys<sup>69</sup>-Cys<sup>96</sup> loop. Residue 124 displayed in green is on an opposing face of the gorge and makes up part of the peripheral anionic site. *C*, model of mAChE in complex with huperzine based on crystal structure of huperzine: *Torpedo californica* AChE (PDB code 1VOT). Huperzine binds at the bottom of active-site gorge and makes surprisingly few specific contacts in the active-site gorge. *D*, fasciculin 2 complexed to mAChE adapted from PDB code 1KU6. Note: hydrogen bonding between the guanidino nitrogen moieties of Arg<sup>11</sup> and Arg<sup>37</sup> in fasciculin and carbonyl oxygen moieties of Glu<sup>84</sup> (3.33 Å) and Leu<sup>76</sup> (3.24 Å) on mAChE, respectively.

model. (It is worth noting that the observed  $r_0$  values typically are less than the fundamental anisotropy of the reporter group (0.33). This most probably reflects the fact that the very fast depolarizing motions produced by tether arm movements are not resolvable by commercial instruments.)

**Molecular Dynamics Simulation of Anisotropy Decay**—The decay of anisotropy because of side chain and segmental motions was simulated utilizing the approach developed by Ichiye and Karplus (15). Specifically, the anisotropy decay of a fluorophore conjugated to a protein side chain was represented as the decay in the time correlation function shown in Equation 6,

$$\rho(\tau) = \langle P_2[\hat{\mu}(t) \cdot \hat{\mu}(t - \tau)] \rangle, \quad (\text{Eq. 6})$$

where  $\hat{\mu}$  is a normalized vector properly chosen to represent the local motion being reported by the fluorophore. In our calculations,  $\hat{\mu}$  was chosen to be a normalized vector representing the direction that goes from the  $\alpha$ -carbon to an atom near the tip of the wild type residue. To wit, for the glutamate residue, we used the average of the two normalized  $C_{\alpha}-O_e$  vectors; for leucine, the normalized  $C_{\alpha}-H_y$  vector; and for tyrosine, the normalized  $C_{\alpha}-O_H$  vector.

For this study, the previously reported 10-ns molecular dynamics simulation of the unliganded wt mAChE (16) was extended to afford a 15-ns trajectory. Frames (snapshots of the trajectory containing the coordinates of all the atoms) were calculated at 1-ps time intervals, and the rotational degrees of freedom were removed by superimposing all frames into a reference frame, minimizing the root mean squared deviations. With these trajectories on a nanosecond time scale, it was

possible to simulate anisotropy decay due to just the combination of side chain and segmental motions; deconstruction of the vectors to resolve the side chain and the segmental motions was not attempted.

## RESULTS AND DISCUSSION

**Characterization of Labeled Mutants**—Acetylthiocholine hydrolysis kinetics of the cysteine-substituted mutants were shown previously to be similar to the wt enzyme suggesting that all mutant enzymes fold correctly despite the presence of the substituted cysteines (13). Moreover, the specific labeling for each mutant was estimated to be 71–80%, 89–93%, 79–80%, and 74–84% for L76C, E81C, E84C, and Y124C, respectively. Substrate and inhibitor recognition by the IAEDANS-labeled mutants is evident from both fasciculin (1.3  $\mu$ M) and huperzine (4  $\mu$ M) producing greater than 95% inhibition of the rate of acetylthiocholine hydrolysis (data not shown). This is not surprising, because previous kinetic studies showed that  $k_{on}$  and  $k_{off}$  of fasciculin were unaltered in the cysteine mutants (17).

In the absence of ligand, the emission maxima of the four IAEDANS-labeled mutants were similar ranging between 482 and 489 nm (Table I). The active-site ligand, (−)-huperzine A, a herbal alkaloid used in Chinese traditional medicine, binds at the base of active-site gorge and should have no direct interac-

tion with all cysteine-conjugated sites based on the x-ray crystal structure of the huperzine-AChE complex (Fig. 1C) (18). Huperzine only affected the steady-state emission properties of the E81C- and E84C-labeled mutants, red shifting the emission maxima 5 and 7 nm and decreasing the relative quantum yields by 18 and 23%, respectively (Table I). This pattern suggests that the huperzine increases the polarity of the microenvironment around the Glu<sup>81</sup> and Glu<sup>84</sup> but not around the Leu<sup>76</sup> and Tyr<sup>124</sup> side chains.

Fasciculin, a peptidic peripheral site inhibitor that caps the mouth of the active-site gorge, influences the microenvironment of the substituted positions in a complex manner. The crystal structure of fasciculin-mAChE complex shows hydrogen bonding between the guanidino moieties of Arg<sup>11</sup> and Arg<sup>37</sup> in fasciculin and the carbonyl oxygens of Glu<sup>84</sup> and Leu<sup>76</sup> on the AChE, respectively (Fig. 1D) (4). Met<sup>33</sup> of fasciculin also is in close proximity but not "in van der Waals contact" with Tyr<sup>124</sup> in the AChE. The largest spectral changes were observed with the labeled Y124C mutant where fasciculin blue-shifted the emission maxima 13 nm and increased the relative quantum yield by 55% (Table I). A similar pattern was seen with the L76C conjugate, but the blue shift was 7 nm, and the relative quantum yield enhancement was 11%. The emission properties of E81C- and E84C-labeled mutants were much less affected by fasciculin binding; the emission maxima were red-shifted 3 and 2 nm, and the relative intensities were decreased by 10 and 3%, respectively (Table I). These results indicate that fasciculin dramatically decreased the polarity around the reporter groups attached to Y124C and to a lesser extent around L76C. Also, fasciculin slightly increased the polarity around the reporter groups attached to E81C and E84C, which is qualitatively the result found using acrylodan instead of IAEDANS (13).

**Emission and Anisotropy Decay**—For brevity, just the parallel and perpendicular emission decay profiles of one labeled mutant (E84C) along with the corresponding anisotropy decay profile are illustrated in Fig. 2. The total emission decay profiles ( $S(t)$ , Equation 2) of all the mutants were best fit to a three-exponential decay function whose geometric averaged lifetimes are summarized in Table II and ranged from 10.0 to 14.6 ns. The ranges of values of the short, intermediate, and long lifetimes of the various conjugates studied were 1.1–3.4, 9.3–16.0, and 18.2–27.9 ns, respectively (data not shown).

Anisotropy decay profiles for the IAEDANS conjugates, with the exception of the labeled Y124C mutant complexed to fasciculin, were well fit by a nonassociative biexponential model (Equation 5). These profiles are illustrated in Fig. 3, and the best fit parameters are summarized in Table II. Except for the huperzine-bound E84C mutant, the processes associated with the "slow" rotational correlation times accounted for 60–80% of the total resolvable anisotropy decay, and the values of these rotational correlation times ranged between 69 and 132 ns (Table II). This range of values is greater than what might be predicted from a protein with 547 amino acids and three *N*-linked oligosaccharides of average mass determined by matrix-assisted laser desorption ionization-mass spectrometry. However, sedimentation equilibrium measurements for this protein correlate best with a molecular mass of 122,000 Da, suggesting that at higher concentrations the molecule may form a reversibly associating dimer.<sup>2</sup> The longest emission lifetimes (18.2–27.9 ns) are long enough to allow estimation of a global rotational correlation time. The crystal structure shows mAChE to have limited dimensional asymmetry so only a single rotational correlation would be resolvable. Because faster emission decay step(s) are also present, deconvolution of components of the

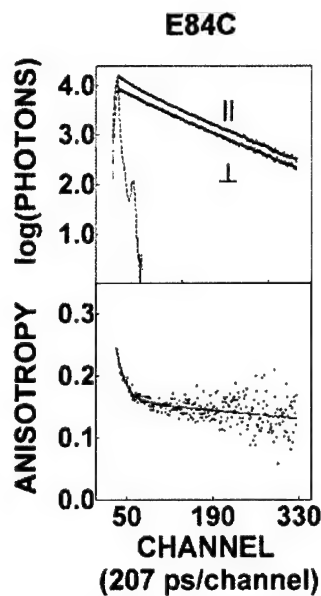


**FIG. 2. Emission and anisotropy decay of IAEDANS-E84C mAChE.** The upper panel illustrates the parallel (||) and perpendicular (⊥) emission decays (single data points). A smooth line through these points was generated with the best fit parameters for a double exponential decay equation. The flash lamp profile is shown as a dotted line. The lower panel shows the time-resolved anisotropy decay (single data points), and a smooth line through these points was generated with the best fit parameters (Table II) for a double exponential nonassociative model (Equation 5). The concentration of the labeled mutants was 1.68  $\mu\text{M}$ .

intermediate and slow phase is subject to uncertainty. Consequently, slow internal fluctuations contributing to the decay rate cannot be ruled out. For the case of huperzine-bound E84C mutant, the  $\phi_{\text{slow}}$  values ranged between 80 and 260 ns. This broader range of values probably reflects a greater uncertainty in  $\phi_{\text{slow}}$  measurements when the slow decay processes represent a small fraction of the total resolvable anisotropy decay, as was the case for the huperzine-bound E84C mutant (31%; Table II).

Comparison of the fast anisotropy decay components of the apo form of the labeled mutants show two features. First, reporter groups attached to substituted cysteines whose native side chains in the crystal structure project into the active-site gorge (L76C and Y124C) are less mobile than reporter groups attached to  $\Omega$  loop-substituted cysteines located on the outer surface of the enzyme (E81C and E84C). This conclusion is seen in the time 0 anisotropy and  $f_{\text{xb}}/\phi_{\text{fast}}$  values (Table II). The time 0 anisotropy values ( $r_0$ ), which likely reflect very fast and unresolvable tether-arm motions (19–21), are higher for the L76C (0.27) and Y124C (0.28) than the E81C (0.25) and E84C (0.25) labeled mutants (Table II). This would suggest, not surprisingly, greater hindrance to the tether-arm movements of the gorge-residing residues. The  $f_{\text{xb}}/\phi_{\text{fast}}$  values of reporter groups attached to the residues that project into the gorge are smaller (L76C, 0.07 and Y124C, 0.05) than the  $f_{\text{xb}}/\phi_{\text{fast}}$  values of reporter groups that are on the outer surface of the enzyme (E81C, 0.13 and E84C, 0.15; Table II). Because the  $f_{\text{xb}}/\phi_{\text{fast}}$  ratio is on the time scale of backbone motions and can be analyzed in terms of the diffusion rate in a "diffusion-in-a-cone model" (22), these results indicate that the ranking of segmental mobility of the residues examined is as follows: E84C > E81C > L76C > Y124C. The second feature that emerges from a comparison of the fast anisotropy decay parameters,  $r_0$  and  $f_{\text{xb}}/\phi_{\text{fast}}$ , is that the reporter groups attached to the substituted cysteines in the Cys<sup>69</sup>–Cys<sup>96</sup>  $\Omega$  loop (L76C, E81C, and E84C)

<sup>2</sup> D. Comoletti, unpublished observations.

TABLE II  
Effect of huperzine and fasciculin on the anisotropy decay parameters of mouse AChE-labeled with IAEDANS

Data are shown as means ( $\pm$ S.D.) from at least three determinations. The vertically and orthogonally polarized emission decays were initially analyzed for the  $S(t)$  parameter (Equation 2), and then for the  $r(t)$  parameter (Equation 5) with the Globals Unlimited™ computer program. The experimental details are described under "Experimental Procedures." The mutants were present at the following concentrations: AEDANS-L76C, 1.63  $\mu$ M; AEDANS-E81C, 1.63  $\mu$ M; AEDANS-E84C, 1.68  $\mu$ M; and AEDANS-Y124C, 2.75  $\mu$ M. To ensure saturation of enzyme with inhibitors, concentrations of huperzine (4  $\mu$ M) and fasciculin (3.17  $\mu$ M) were added to AEDANS-L76C, AEDANS-E81C, and AEDANS-E84C; huperzine (4.8  $\mu$ M) and fasciculin (4  $\mu$ M) were added to AEDANS-Y124C.

Mutant	Inhibitor	$r_0^a$	$f_{xb}^b$	$\phi_{fast}^c$	$f_{xb}/\phi_{fast}$	$\phi_{slow}^d$	$\psi_r^{2e}$	$\tau^f$
L76C	None	0.27 $\pm$ 0.01	0.26 $\pm$ 0.01	3.5 $\pm$ 0.3	0.07 $\pm$ 0.01	84–111	1.2	10.0 $\pm$ 0.1
	Huperzine	0.28 $\pm$ 0.02	0.26 $\pm$ 0.01	3.5 $\pm$ 0.6	0.07 $\pm$ 0.01	84–119	1.3	9.7 $\pm$ 0.1
	Fasciculin	0.27 $\pm$ 0.01	0.22 $\pm$ 0.01	4.8 $\pm$ 0.3	0.05 $\pm$ 0.01	92–118	1.2	10.2 $\pm$ 0.2
E81C	None	0.25 $\pm$ 0.01	0.29 $\pm$ 0.01	2.3 $\pm$ 0.2	0.13 $\pm$ 0.01	76–105	1.3	14.6 $\pm$ 0.1
	Huperzine	0.26 $\pm$ 0.01	0.40 $\pm$ 0.01	2.3 $\pm$ 0.1	0.18 $\pm$ 0.01	84–118	1.2	13.6 $\pm$ 0.1
	Fasciculin	0.26 $\pm$ 0.01	0.34 $\pm$ 0.02	2.2 $\pm$ 0.1	0.16 $\pm$ 0.01	77–100	1.3	13.6 $\pm$ 0.1
E84C	None	0.25 $\pm$ 0.01	0.42 $\pm$ 0.02	2.9 $\pm$ 0.1	0.15 $\pm$ 0.01	90–132	1.3	12.6 $\pm$ 0.2
	Huperzine	0.22 $\pm$ 0.02	0.69 $\pm$ 0.02	2.8 $\pm$ 0.2	0.25 $\pm$ 0.03	80–260	1.2	10.2 $\pm$ 0.2
	Fasciculin	0.26 $\pm$ 0.01	0.24 $\pm$ 0.02	4.6 $\pm$ 0.8	0.05 $\pm$ 0.01	69–87	1.1	11.3 $\pm$ 0.7
Y124C	None	0.28 $\pm$ 0.01	0.16 $\pm$ 0.01	3.6 $\pm$ 0.6	0.05 $\pm$ 0.01	75–89	1.2	14.5 $\pm$ 0.2
	Huperzine	0.29 $\pm$ 0.02	0.18 $\pm$ 0.01	4.0 $\pm$ 0.7	0.04 $\pm$ 0.01	74–91	1.4	13.8 $\pm$ 0.4
	Fasciculin	ND <sup>g</sup>	ND	ND	ND	ND	ND	18.2 $\pm$ 0.1

<sup>a</sup> The time 0 anisotropy.

<sup>b</sup> The fraction of the observed anisotropy decay associated with the "fast" depolarization processes.

<sup>c</sup> Fast rotational correlation time.

<sup>d</sup> The range of the "slow" rotational correlation times that yield  $\chi^2$  values 5% above the minimum.

<sup>e</sup> The reduced  $\chi^2$ .

<sup>f</sup> Geometric averaged lifetimes ( $\Sigma \alpha_i \tau_i$ , where  $\Sigma \alpha_i = 1$ ).

<sup>g</sup> ND, not determined.

are more mobile than the reporter group attached to the non- $\Omega$  loop residue (Y124C) (Table II).

**Ligand Binding and Anisotropy Decay**—The influence of huperzine and fasciculin on the anisotropy decay parameters of the labeled mutants studied is complex and ligand-dependent.

Huperzine, which should not interact with the modified  $\Omega$  loop residues (Fig. 1C), selectively increased the mobility of just the labeled E81C and E84C residues without affecting the mobility of the labeled L76C or Y124C residues. This is evidenced in the  $f_{xb}/\phi_{fast}$  values of the labeled-E81C and E84C mutants that increased upon huperzine binding from 0.13 to 0.18 and from 0.15 to 0.25, respectively (Table II; Fig. 3). The fact that the fluctuations of just the E81C and E84C were perturbed, and not L76C in the  $\Omega$  loop, is indicative of a lack of conformational coupling between Leu<sup>76</sup> and Glu<sup>81</sup>/Glu<sup>84</sup> positions in the  $\Omega$  loop. Hence, the  $\Omega$  loop does not behave as a rigid flap.

Consistent with the crystal structure showing fasciculin hydrogen bonding (from the guanidino moiety of Arg<sup>37</sup>) to the carbonyl oxygen of Leu<sup>76</sup> (2.83 Å; Fig. 1), the  $f_{xb}/\phi_{fast}$  value of the labeled L76C mutant decreases upon fasciculin binding from 0.07 to 0.05 (Table II) suggesting decreased segmental mobility around L76C. For the E81C mutant, where the wild type crystal structure does not predict any direct interaction with fasciculin, the  $f_{xb}/\phi_{fast}$  value increased from 0.13 to 0.16 (Table II), indicating a modest increase in segmental mobility of the E81C residue, a behavior similar to that seen for huperzine. Combining hydrophobic and electrostatic interactions, the fasciculin-mAChE complex encompasses an interface of 1100 Å. It is surprising that, despite strong suppression of mobility throughout, we observed enhanced dynamic motion around E81C.

For the E84C mutant, whose side chain may come in closer contact with fasciculin than E81C, fasciculin binding may introduce multiple factors that control decay of anisotropy. Fasciculin slowed the fast anisotropy decay processes suggesting a reduced segmental mobility ( $f_{xb}/\phi_{fast}$  decreases from 0.15 to 0.05) and accelerated the slow anisotropy decay processes (the range of  $\phi_{slow}$  values decreased from 90–132 to 69–87 ns; Table II). These seemingly complex decay profile emerges without

direct occlusion between the fluorophore and toxin as evidenced by the fact that fasciculin binding produced no significant change in  $r_0$  and only a minimal change in the steady-state and emission lifetime parameters (Tables I and II). However, the fasciculin molecule should stabilize the  $\Omega$  loop near the rim of the gorge, and Arg<sup>11</sup> on fasciculin may electrostatically interact with the sulfonic acid moiety of the conjugated AEDANS. A possible explanation for the complex decay profile at Glu<sup>84</sup> is that fasciculin induced large amplitude, slow backbone fluctuations around E84C that both slowed the segmental fluctuation rate and increased its amplitude. Such internal fluctuations might occur if the C-terminal half of the  $\Omega$  loop starting at about Glu<sup>81</sup> became less tethered to the core of the molecule and underwent larger angular excursions on a time scale between ~10 and ~50 ns. Such conformational fluctuations would accelerate the observed slow rotational correlation time. From this perspective, fasciculin has a disordering effect at both E81C and E84C. Clearly, additional studies are required to establish the mechanistic basis for these increased fluctuations.

For the labeled Y124C mutant, the anisotropy decay could not be reasonably fit to a simple decay model. Instead of continuously decreasing from time 0, the anisotropy increased very slightly for a few nanoseconds and then decreased. Moreover, the total depolarization process was much slower than any other decay profiles examined (Fig. 3). This pattern of decay probably results from a complex association of emission lifetimes with specific rotary diffusional processes (23). Combined with the very substantial (55%) increase in the total emission described above and the close proximity of Tyr<sup>124</sup> to fasciculin in the crystal structure of mAChE (PDB code 1KU6), which would presumably be closer in the 5(((acetyl)amino)ethyl)amino)naphthalene-1-sulfonic acid (AEDANS)-labeled mutant, the complex anisotropy decay of the fasciculin-bound and labeled Y124C mutant strongly suggests a direct reporter group-fasciculin interaction and subsequent reduction in the mobility of Y124C. This direct interaction makes problematic an assessment of the effect of fasciculin on the segmental motion around the Tyr<sup>124</sup> residue in the wild type enzyme.

FIG. 3. Effect of huperzine and fasciculin on the anisotropy decay of the IAEDANS-labeled mAChE mutants. The time-resolved anisotropy decay (single data points) and a smooth line through these points were generated with the best fit parameters (Table II) for a double exponential nonassociative decay model (Equation 5). Data points represent enzymes without inhibitors (●), with huperzine (+), or with fasciculin (▲). The peak of the flash lamp profile arbitrarily defined the zero time point. To ensure saturation of enzyme with inhibitors, concentrations of huperzine ( $4 \mu\text{M}$ ) and fasciculin ( $3.17 \mu\text{M}$ ) were added to IAEDANS-E81C (A), IAEDANS-E84C (B), and IAEDANS-L76C (C); huperzine ( $4.8 \mu\text{M}$ ) and fasciculin ( $4 \mu\text{M}$ ) were added to IAEDANS-Y124C (D). The concentrations of IAEDANS-L76C, IAEDANS-E81C, IAEDANS-E84C, and IAEDANS-Y124C were  $1.63$ ,  $1.69$ ,  $1.68$ , and  $2.75 \mu\text{M}$ , respectively.

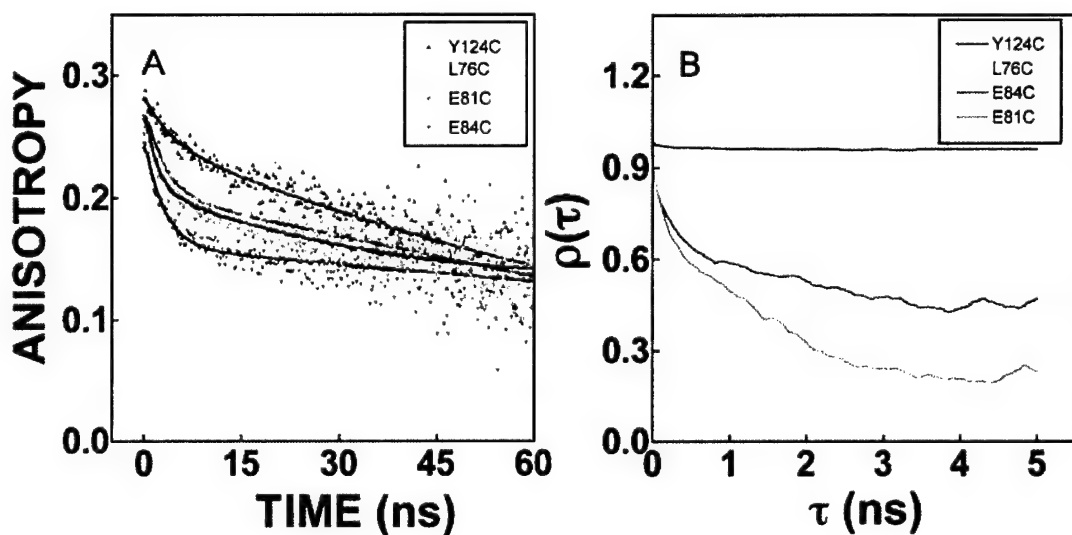
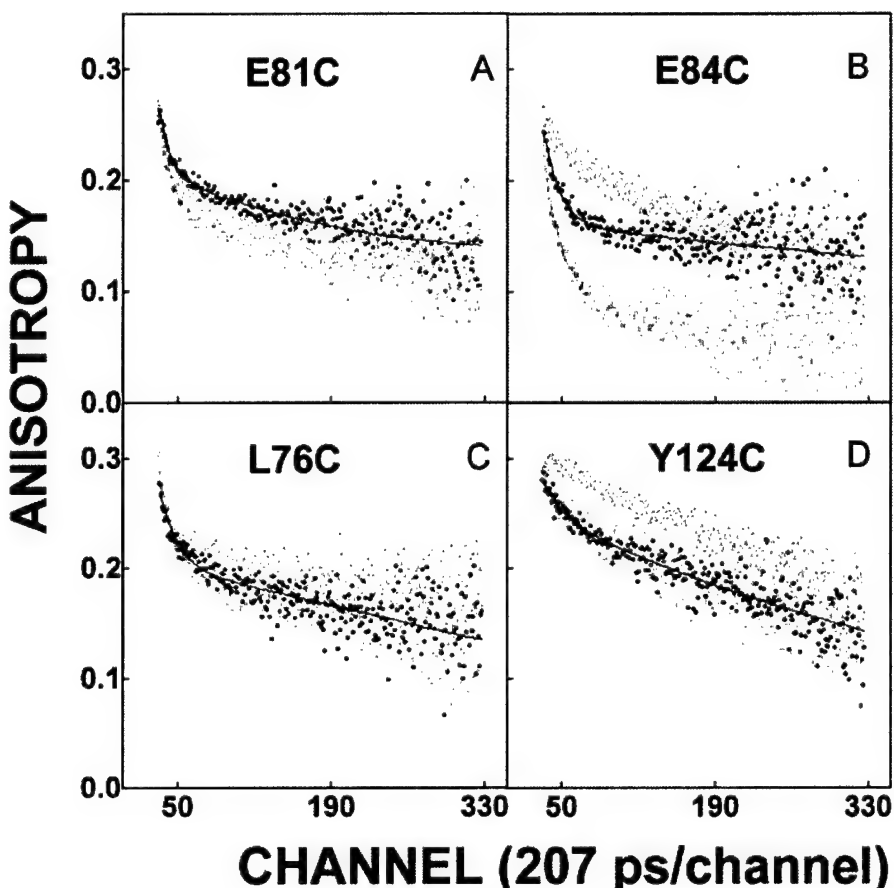


FIG. 4. Comparison of the experimental and simulated anisotropy decay. A, overlay of experimental anisotropy decays of unliganded AEDANS-L76C (+) (green), AEDANS-E81C (●) (orange), AEDANS-E84C (▼) (red), and AEDANS-Y124C (▲) (blue) mAChE. B, the time correlation function  $\rho(\tau)$  from the 15-ns mAChE molecular dynamics simulation based on PDB code 1MAH.

**Comparison of Experimental and Simulated Anisotropy Decay**—To validate further fluorescence anisotropy decay to measure segmental mobility, the anisotropy parameters were compared with the calculated decay in the time correlation function  $\rho(\tau)$  (where  $\rho(\tau)$  is time correlation function of a vector representing the direction that goes from the  $\alpha$ -carbon to an atom near the tip of the wt side chain) for each mutated site. The results of this comparison for the apoenzyme are illustrated in Fig. 4. Because  $\rho(\tau)$  has the characteristics of a time

correlation function, it becomes less trustworthy as  $\tau$  increases and the number of samples diminishes. Therefore, only the first one-third of the 15-ns  $\rho(\tau)$  profile is shown (Fig. 4B). For the unliganded mAChE, the simulated mobility ranking for the four sites of interest was E81C > E84C > L76C > Y124C. This is similar, but not identical, to the experimental anisotropy measures of segmental mobility,  $f_{xb}/\phi_{\text{fast}}$ , whose mobility ranking was E84C > E81C > L76C > Y124C.

Why the theoretical calculations show the motions of residue

81 randomizing more rapidly than residue 84, whereas the experimental data show the opposite, is unclear. However, there are several explanations to be considered. First, experimental anisotropy decay is dependent upon the orientation of the emission transition dipole relative to the major directions of the movement of the reporter group, and the correlation function is not. Second, cysteine substitutions and fluorophore conjugation could have perturbed the local environment differentially affecting the mobilities of the substituted side chains. Finally, the experimental  $f_{xb}/\phi_{fast}$  ratio is not measuring the same motions as  $\rho(\tau)$ .  $\rho(\tau)$  reflects both side chain and segmental motions of the studied residue, whereas  $f_{xb}/\phi_{fast}$  is more reflective of ensemble averaged segmental motions of the fluorophore conjugated and adjacent amino acid residues (20).

**General Conclusions**—As discussed above, several lines of evidence point toward the existence of transient gorge enlargements that would facilitate substrate binding and product egress. These include molecular dynamics simulations that predict breathing or gating movements (8–10) and the paradoxically high substrate turnover number in relation to the small diameter of the active-site gorge when compared with the cross-sectional size of acetylcholine. This report adds further credence to the existence of transient gorge enlargements by experimentally demonstrating that the outer wall of the active-site gorge, the Cys<sup>69</sup>–Cys<sup>96</sup> Ω loop, is conformationally flexible and capable of undergoing residue-specific and ligand-dependent changes in backbone motions. The fact that all published AChE crystal structures depict only a narrow active-site gorge does not provide conclusive evidence for a static, narrow active-site gorge in solution (5–7). A growing body of evidence suggests that the conditions of AChE crystallization simply favor a narrow gorge conformational state (13).

Although we only have a fragmentary experimental picture of the conformational dynamics of the mAChE, this report and an ongoing study using site-directed labeling with fluorescein maleimide of three additional sites near the gorge shows only a partial degree of coupling of the fluctuations between residues. If this reflects a general feature of AChE conformational dynamics, then it would suggest that the transient gorge enlargements result from random or near random (non-concerted) fluctuations that periodically result in gorge enlargement. These near random fluctuations leading to periodic gorge enlargements would presumably occur in a time frame of nanoseconds or subnanoseconds (24). Despite the high catalytic efficiency of AChE with a turnover number of  $10^4 \text{ s}^{-1}$ , this time interval for gorge fluctuations is short in relation to the time required for individual catalytic steps or appreciable diffusion of substrate.

In summary, we examined the possibility that the Cys<sup>69</sup>–Cys<sup>96</sup> Ω loop, which forms the outer wall of the active-site gorge of mAChE, plays a role in transient gorge enlargement by using site-directed labeling in conjunction with time-resolved fluorescence anisotropy. A molecular dynamics simulation of the side chain and segmental motions of the mutated residues was also performed to further validate this approach. The results indicate

the Ω loop residues examined show torsional motion and segmental fluctuations and therefore could contribute to transient gorge enlargements. In turn, these rapid fluctuations occur in a time frame that is short with respect to diffusional translation of substrate (24) and could be expected to enhance substrate accessibility and product egress. Examination of the effects of two inhibitors, one of which interacts directly with the outer portion of the Ω loop (fasciculin) and one of which does not (huperzine), also reveals internal loop flexibility and that the backbone movements are not all tightly coupled. This later observation suggests the possibility that transient gorge enlargements result from random or near random (non-concerted) fluctuations that periodically widen the gorge. Systematic mapping of other positions on the AChE surface should be able to further delineate regions involved and ultimately reveal solution conformations of AChE not discernible in a static crystal structure.

**Acknowledgments**—We thank Dr. Zoran Radic for advice and many valuable discussions related to this study, Dr. Davide Comeletti for analytical ultracentrifugation, and Dr. Lori Jennings for matrix-assisted laser desorption ionization time-of-flight-mass spectrometric analysis of mAChE.

#### REFERENCES

- Rosenberry, T. L. (1975) *Adv. Enzymol. Relat. Areas Mol. Biol.* **43**, 103–218
- Quinn, D. M. (1987) *Chem. Rev.* **87**, 955–979
- Sussman, J. L., Harel, M., Frolov, F., Oefner, C., Goldman, A., Toker, L., and Silman, I. (1991) *Science* **253**, 872–879
- Bourne, Y., Taylor, P., and Marchot, P. (1995) *Cell* **83**, 503–512
- Harel, M., Schalk, I., Ehretabatier, L., Bouet, F., Goeldner, M., Hirth, C., Axelsen, P. H., Silman, I., and Sussman, J. L. (1993) *Proc. Natl. Acad. Sci. U. S. A.* **90**, 9031–9035
- Harel, M., Quinn, D. M., Nair, H. K., Silman, I., and Sussman, J. L. (1996) *J. Am. Chem. Soc.* **118**, 2340–2346
- Bourne, Y., Taylor, P., Bougis, P. E., and Marchot, P. (1999) *J. Biol. Chem.* **274**, 2963–2970
- Gilson, M. K., Straatsma, T. P., McCammon, J. A., Ripoll, D. R., Faerman, C. H., Axelsen, P. H., Silman, I., and Sussman, J. L. (1994) *Science* **263**, 1276–1278
- Wlodek, S. T., Clark, T. W., Scott, L. R., and McCammon, J. A. (1997) *J. Am. Chem. Soc.* **119**, 9513–9522
- Shen, T., Tai, K., Henchman, R. H., and McCammon, J. A. (2002) *Acc. Chem. Res.* **35**, 332–340
- Grochulski, P., Li, Y., Schrag, J. D., Bouthillier, F., Smith, P., Harrison, D., Rubin, B., and Cygler, M. (1993) *J. Biol. Chem.* **268**, 12843–12847
- Grochulski, P., Li, Y., Schrag, J. D., and Cygler, M. (1994) *Protein Sci.* **3**, 82–91
- Shi, J., Boyd, A. E., Radic, Z., and Taylor, P. (2001) *J. Biol. Chem.* **276**, 42196–42204
- Marchot, P., Ravelli, R. B., Raves, M. L., Bourne, Y., Vellom, D. C., Kanter, J., Camp, S., Sussman, J. L., and Taylor, P. (1996) *Protein Sci.* **5**, 672–679
- Ichiye, T., and Karplus, M. (1983) *Biochemistry* **22**, 2884–2893
- Tai, K., Shen, T., Borjesson, U., Philippopoulos, M., and McCammon, J. A. (2001) *Biophys. J.* **81**, 715–724
- Boyd, A. E., Marnett, A. B., Wong, L., and Taylor, P. (2000) *J. Biol. Chem.* **275**, 22401–22408
- Raves, M. L., Harel, M., Pang, Y. P., Silman, I., Kozikowski, A. P., and Sussman, J. L. (1997) *Nat. Struct. Biol.* **4**, 57–63
- Lakowicz, J. R. (1999) *Principles of Fluorescence Spectroscopy*, 2nd Ed., pp. 321–345, Kluwer Academic and Plenum Publishers, New York
- Gangal, M., Cox, S., Lew, J., Clifford, T., Garrad, S. M., Aschbacher, M., Taylor, S. S., and Johnson, D. A. (1998) *Biochemistry* **37**, 13728–13735
- Gangal, M., Clifford, T., Deich, J., Cheng, X., Taylor, S. S., and Johnson, D. A. (1999) *Proc. Natl. Acad. Sci. U. S. A.* **96**, 12394–12399
- Kinosita, K., Jr., Kawato, S., and Ikegami, A. (1977) *Biophys. J.* **20**, 289–305
- Steiner, R. F. (1991) in *Topics in Fluorescence Spectroscopy* (Lakowicz, J. R., ed.) pp. 13–14, Plenum Press, New York
- Zhou, H. X., Wlodek, S. T., and McCammon, J. A. (1998) *Proc. Natl. Acad. Sci. U. S. A.* **95**, 9280–9285

## Nanosecond Dynamics of Acetylcholinesterase Near the Active Center Gorge\*

Received for publication, February 10, 2004  
Published, JBC Papers in Press, April 12, 2004, DOI 10.1074/jbc.M401482200

Aileen E. Boyd‡§, Cristina S. Dunlop‡¶, Lilly Wong‡, Zoran Radić‡, Palmer Taylor‡||, and David A. Johnson\*\*

From the ‡Department of Pharmacology, University of California, La Jolla, California 92093-0636 and the

\*\*Division of Biomedical Sciences, University of California, Riverside, California 92521-0121

To delineate the role of peptide backbone flexibility and rapid molecular motion in acetylcholinesterase catalysis and inhibitor association, we investigated the decay of fluorescence anisotropy at three sites of fluorescein conjugation to cysteine-substitution mutants of the enzyme. One cysteine was placed in a loop at the peripheral site near the rim of the active center gorge (H287C); a second was in a helical region outside of the active center gorge (T249C); a third was at the tip of a small, flexible  $\Omega$  loop well separated from the gorge (A262C). Mutation and fluorophore conjugation did not appreciably alter catalytic or inhibitor binding parameters of the enzyme. The results show that each site examined was associated with a high degree of segmental motion; however, the A262C and H287C sites were significantly more flexible than the T249C site. Association of the active center inhibitor, tacrine, and the peripheral site peptide inhibitor, fasciculin, had no effect on the anisotropy decay of fluorophores at positions 249 and 262. Fasciculin, but not tacrine, on the other hand, dramatically altered the decay profile of the fluorophore at the 287 position, in a manner consistent with fasciculin reducing the segmental motion of the peptide chain in this local region. The results suggest that the motions of residues near the active center gorge and across from the Cys<sup>69</sup>-Cys<sup>96</sup>  $\Omega$  loop are uncoupled and that ligand binding at the active center or the peripheral site does not influence acetylcholinesterase conformational dynamics globally, but induces primarily domain localized decreases in flexibility proximal to the bound ligand.

Catalysis of the hydrolysis of acetylcholine by the serine hydrolase, acetylcholinesterase (AChE),<sup>1</sup> occurs at or near the diffusion limit (1, 2). The crystal structure of AChE reveals the enzyme active center to be at the base of a narrow, aromatic side chain lined gorge, some 18–20 Å in depth (3–5). How the

\* This work was supported in part by United States Public Health Services Grants R37-GM18360 and P42-E10337, Department of Army Medical Defense Grant 17C-951-5027, and a University of California Intercampus Grant. The costs of publication of this article were defrayed in part by the payment of page charges. This article must therefore be hereby marked "advertisement" in accordance with 18 U.S.C. Section 1734 solely to indicate this fact.

† Supported by National Institutes of Health Training Grant GM07752.

‡ Present address: Wayne State University School of Medicine, Detroit, MI 48201.

¶ To whom correspondence should be addressed: Dept. of Pharmacology, University of California, La Jolla, CA 92093-0636. Tel.: 858-534-4028; Fax: 858-534-8248; E-mail: pwtaylor@ucsd.edu.

|| The abbreviations used are: AChE, acetylcholinesterase; FM, fluorescein 5-maleimide; IAF, 5-iodoacetamido-fluorescein.

substrate can rapidly traverse this tortuous route, acylate the active center serine with concomitant choline departure, and then deacylate with acetate departure in each catalytic cycle of ~100 μs has been a source of puzzlement. A large dipole moment aligned with the gorge entry portal enhances diffusional ingress (6–8). Alternative portals have been proposed as routes for access or removal of H<sub>2</sub>O, H<sup>+</sup>, or products (9–11); however, the finding that mutations in the vicinity of the proposed alternative portals do not alter steady-state catalytic parameters argues against a second access route being a rate-limiting step (12, 13).

Molecular dynamic simulations have pointed to flexibility and/or fluctuations in gating that may enhance accessibility to the active center (14, 15). A 10-ns molecular dynamic simulation of mouse AChE analyzed in terms of projections on the principal components suggests that collective motions on many time scales contribute to the opening of the gorge (16). Residues at the gorge opening and constriction point generally have larger correlation vectors pointing away from the gorge than do residues located peripheral to the gorge, suggesting large amplitude gorge opening motions.

Although molecular dynamic simulations support the existence of a conformationally active gorge, little experimental support exists. Analysis of the various published crystal structures of the apo and ligand-bound enzyme from various sources yield no indication that the gorge exists in "open" and "closed" states. On the other hand, Laue crystallography, with its diminished exposure time of x-ray radiation, has the potential to detect short lifetime intermediates in formation of AChE complexes (17). Also, we have reported that both active center and peripheral site inhibitors alter dramatically the emission maxima of acrylodan conjugated to mouse AChE cysteine mutants (18). Because many of the affected residues do not directly contact the bound ligand, the findings reveal ligand-dependent conformational changes in the Cys<sup>69</sup>-Cys<sup>96</sup>  $\Omega$ -loop, which forms one of the walls of the active center gorge (18, 19). Additionally, we have found substantial internal flexibility at this  $\Omega$ -loop as well as changes in flexibility induced by ligand binding (20).

To extend our observations on the AChE conformational dynamics to additional areas around the active center gorge, we measured the effects of two inhibitors on the backbone flexibility of three surface sites across the active center gorge from the Cys<sup>69</sup>-Cys<sup>96</sup>  $\Omega$ -loop using site-directed labeling in combination with time-resolved fluorescence anisotropy. Specifically, we chose three aligned sites for cysteine substitution and fluorescein conjugation, starting at the rim of the gorge (H287C), extending radially to an adjacent surface  $\alpha$ -helix (T249C), and then to the tip of a small and mobile  $\Omega$ -loop (A262C), some 20 Å away from the gorge rim (Fig. 1). Time-

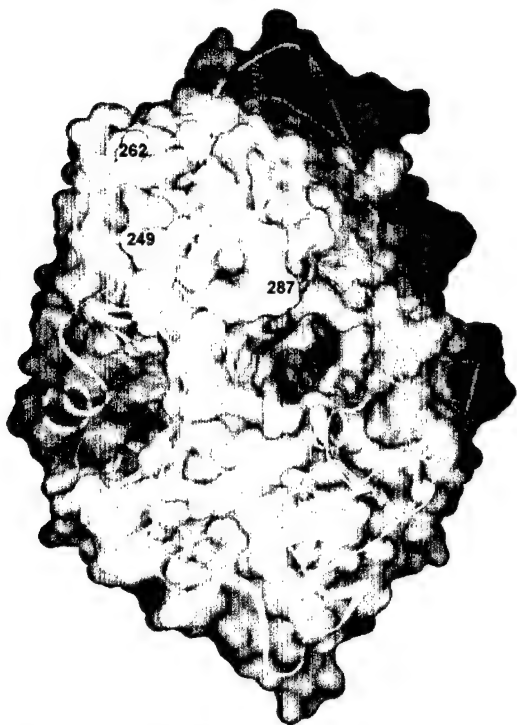


**FIG. 1. Locations of the sites of cysteine substitution and fluorescein conjugation.** Illustrated is a surface presentation of mouse AChE looking into the active center gorge (Protein Data Bank code 1KU6) with the Cys<sup>69</sup>-Cys<sup>96</sup> Ω-loop, highlighted in green, and the three sites of cysteine substitution and fluorescein conjugation (Thr<sup>249</sup>, Ala<sup>262</sup>, and His<sup>287</sup>), highlighted in yellow. The position of bound tacrine, shown in red, was derived from the crystallographic coordinates of the *Torpedo californica* AChE-tacrine complex (Protein Data Bank code 1ACJ) and overlaid into the mouse AChE structure.

resolved fluorescence anisotropy yields information on the excited state of the fluorophore in the picosecond to nanosecond time frame (21), a time domain much shorter than the AChE catalytic cycle. With this approach we hoped to assess the basic characteristics of the motion at sites near the gorge but across from the Cys<sup>69</sup>-Cys<sup>96</sup> Ω-loop. We reasoned that if the opening motions were conformationally linked, ligand association, which would influence peptidyl backbone flexibility adjacent to the bound ligand, should also affect motion and flexibility parameters at more distal loci. The results reveal distinct modes of molecular motion in the individual regions examined. Also, the very limited effects of ligand binding upon anisotropy decay suggest uncoupled movements of the regions examined, a finding consistent with a model for transient gorge openings that is dominated by random segmental movements.

#### EXPERIMENTAL PROCEDURES

**Materials**—Acetylthiocholine iodide, 5,5'-dithio-bis(2-nitrobenzoic acid) (Ellman's reagent), dithiothreitol, and tacrine (9-amino-1,2,3,4-tetrahydroacridine hydrochloride hydrate) were purchased from Sigma. Fluorescein 5-maleimide (FM) and 5-iodoacetaminofluorescein (IAF) were obtained from Molecular Probes. Fasciculin 2 (purified from the venom of *Dendroaspis angusticeps*) was a gift of Dr. Pascale Marchot (University of Marseille, France). Drs. Yacov Ashani and Bhupendra P. Doctor (Walter Reed Army Research Center, Washington, D. C.) kindly provided 7-[(methylthoxy)phosphinyl]-oxyl-1-methylquinolinium iodide. All other chemicals came from commercial sources and were, at least, reagent grade.

**Enzyme Preparation**—Mutagenesis procedures to generate the cysteine-substituted mutants are described elsewhere (22). Briefly, cDNAs encoding a monomeric form of the mouse enzyme truncated at position 548 were placed in the mammalian expression vector, pcDNA3 (Invitrogen), and were subjected to PCR-mediated (QuikChange<sup>TM</sup>, Stratagene) mutagenesis. Restriction enzyme analyses allowed detection of the mu-

tations. To ensure the absence of spurious mutations, cassettes encompassing the mutated site were subcloned into pcDNA3 vectors that had not been exposed to the mutagenesis procedure, and their nucleotide sequences were verified by double stranded sequencing.

Human embryonic kidney (HEK 293) cells, purchased from American Type Culture Collection (Manassas, VA), were plated in Dulbecco's modified Eagle's medium supplemented with 10% fetal bovine serum at a density of  $1.5 \times 10^6$  cells per 10-cm dish, 24 h prior to transfection. Standard HEPES/calcium phosphate precipitation methods were used to apply 10 µg of plasmid DNA per plate to the cell monolayers. The next day, cells were rinsed with phosphate-buffered saline and supplied with serum-free media for continued growth (Ultraculture, Bio-Whittaker, Walkersville, MD). Large scale productions of mutant enzymes entailed creation of stable cell lines that exhibited G418 (Gemini Bio-Products, Woodland, CA) resistance following cotransfection with a neomycin resistance gene as described elsewhere (22, 23). Harvests of mutant AChE in serum-free media from confluent cells in three-tiered flasks (Nalge Nunc Int., Rochester, NY) typically continued for several weeks after which expression levels began to decline.

Affinity chromatography with trimethyl (*m*-aminophenyl)ammonium linked through a long tether arm to Sepharose CL-4B resin (Sigma) permitted one-step purification of AChE, both mutant and wild-type in amounts between 5 and 25 mg, as previously described (24–26). Purity was assessed by SDS-PAGE and by comparisons of specific activity with absorbance at 280 nm to measure protein concentration ( $\epsilon_{280} = 1.14 \times 10^5 \text{ M}^{-1} \text{ cm}^{-1}$  (27)).

**Catalytic Activity**—The catalytic activity of each unlabeled and labeled mutant was measured with the Ellman assay (28).  $K_m$  and  $K_{ss}$  (the dissociation constant of a ternary complex resulting in substrate inhibition or activation) were evaluated as described in previous kinetic schemes (23). The  $x$  intercept of a plot of the residual catalytic activity versus the concentration of the irreversible inhibitor 7-[(methylthoxy)phosphinyl]-oxyl-1-methylquinolinium iodide yielded the enzyme concentration, and, in turn,  $k_{cat}$  (29).

**Fluorescein Labeling**—The mutant enzymes were pretreated with 0.25 mM dithiothreitol for 30 min at room temperature to ensure that all of the free cysteines were reduced, and free dithiothreitol was removed with a G-50 Sephadex spin column (Roche Diagnostics) equilibrated in 0.1 M sodium phosphate buffer, pH 7. FM and IAF were dissolved in dimethylformamide to make stock concentrations between 6 and 15 mM. The thioactive probes, FM and IAF, at 100 times the enzyme concentration, were added to the enzyme solutions to achieve either a 3-fold molar excess in the case of the A262C mutant or a 20-fold molar excess in the case of the T249C and H287C mutants. Labeling was allowed to proceed for 12 h at 4 °C for the A262C mutant and for 2 h at 37 °C for the T249C and H287C mutants.

Unconjugated fluorescein derivatives were removed by gel-filtration with G-25 Sephadex (Amersham Biosciences), equilibrated with 0.1 M sodium phosphate buffer, pH 7. Parallel labeling reactions with wild-type mouse AChE were performed to assess nonspecific labeling. Stoichiometries of fluorescein-labeled mutants were estimated spectrophotometrically by substitution of the measured absorbance values at 280 nm ( $A_{280}$ ) and 495 nm ( $A_{495}$ ) into the following expression.

$$\frac{[\text{Fluorescein}]}{[\text{AChE}]} = \frac{A_{495}/83,000}{(A_{280} - 0.18A_{495})/114,000} \quad (\text{Eq. 1})$$

**Steady-state Emission**—Steady-state emission spectra were measured at room temperature using a FluoroMax II spectrofluorometer (Jobin Yvon Inc., Edison, NJ).

**Time-resolved Fluorescence Anisotropy**—Emission anisotropy was determined by time-correlated single photon-counting measurements (30) with an IBH (Edinburgh, UK) 480-nm NanoLED<sup>TM</sup> flash lamp run at 1 MHz and IBH model TBX-04 photon detector. The vertically [ $I_0(t)$ ] and orthogonally [ $I_1(t)$ ] polarized emission components were collected by exciting samples with vertically polarized light while orienting the emission polarizer (Polaroid HNPB dichroic film) in either a vertical or orthogonal direction. Excitation and emission bands were selected with an Oriel 500-nm short-pass interference filter (catalog number 59876) and a Corning 3-68 cut on filter with a half-maximum transmission of 540 nm, respectively. Typically,  $2 \times 10^4$  peak counts were collected (in 1–2 min) when the emission polarizer was vertically oriented. The orthogonal emission decay profile was generated over the same time interval that was used to generate the vertical emission decay profile. Samples were held at 22 °C. To minimize convolution artifacts, flash lamp profiles were recorded by removing the emission filter and monitoring light scatter from a suspension of latex beads. The data analysis software corrected the wavelength-dependent temporal

dispersion of the photoelectrons by the photomultiplier. The polarization bias ( $G$ ) of the detection instrumentation was determined by measuring the integrated photon counts/ $6 \times 10^6$  lamp flashes while the samples were excited with orthogonally polarized light and the emission was monitored with a polarizer oriented in the vertical and orthogonal directions ( $G = 1.028$ ).

The emission anisotropy decay,  $r(t)$ , given by the expression,

$$r(t) = \frac{I_{\parallel}(t) - G \cdot I_{\perp}(t)}{I_{\parallel}(t) + 2G \cdot I_{\perp}(t)} \quad (\text{Eq. 2})$$

and total emission decay,  $S(t)$ , for a macroscopically isotropic sample,

$$S(t) = I_{\parallel}(t) + 2G \cdot I_{\perp}(t) \quad (\text{Eq. 3})$$

were deconvolved simultaneously from the individual polarized emission components expressed as,

$$I_{\parallel} = \frac{S(t)}{3} [1 + 2r(t)] \quad (\text{Eq. 4})$$

and the following.

$$I_{\perp}(t) = \frac{S(t)}{3} [1 - r(t)] \quad (\text{Eq. 5})$$

Thus, both  $I_{\parallel}(t)$  and  $I_{\perp}(t)$  are determined by the same fitting functions,  $S(t)$  and  $r(t)$ , and fitting parameters.

The fluorescence lifetimes for each sample were determined by initially generating a total emission decay profile from  $I_{\parallel}(t)$  and  $I_{\perp}(t)$  with Equation 3 and then globally fitting  $I_{\parallel}(t)$  and  $I_{\perp}(t)$  decay profiles to Equations 4 and 5 with the lifetime parameters fixed and with the following anisotropy decay expression.

$$r(t) = r_0 f_{\text{sb}} \exp(-t/\phi_{\text{fast}}) + r_0(1 - f_{\text{sb}}) \exp(-t/\phi_{\text{slow}}) \quad (\text{Eq. 6})$$

Here,  $r_0$  is the amplitude of the anisotropy at time 0,  $f_{\text{sb}}$  is the fraction of the anisotropy decay associated with the fast decay processes, and  $\phi$  is the rotational correlation time of the anisotropy decay. The subscripts *fast* and *slow* denote the fast and slow decay processes, respectively. A nonassociative model was assumed, indicating that the emission relaxation times are common to all the rotational correlation times. The fluorescence data were analyzed using the Globals software package developed at the Laboratory for Fluorescence Dynamics at the University of Illinois, Urbana-Champaign. Goodness of fit was evaluated from the values of the reduced  $\chi^2$  and by visual inspection of the weighted-residual plots.

To better define the uncertainty of the measured slow, presumably whole body, rotational correlation times, a range (not a mean  $\pm$  S.D.) of  $\phi_{\text{slow}}$  values was determined for each data set that produced a reasonably acceptable fit to the anisotropy decay. Specifically, a unidimensional search procedure was performed that involved directed searches along the  $\phi_{\text{slow}}$  parameter axis, not allowing other fitting parameters to vary, to find the minimum and maximum  $\phi_{\text{slow}}$  values that raised the  $\chi^2$  values by 5%.

**Estimation of Stokes' Radius**—The Stokes' radius of wild-type AChE was estimated by gel filtration with a Superdex 200 HR 10/30 column (Amersham Biosciences) equilibrated with 0.1 M ammonium acetate buffer, pH 7.2. The elution volumes of wild-type AChE and proteins with known Stokes' radii were measured. The estimated value of the wild-type AChE Stokes' radius of wild-type AChE was read from a curve derived using the known Stokes' radii and the elution parameters of the standards, following the equation of Porath (31).

**Molecular Dynamic Simulations of FM-H287C Mutant**—A series of short, 3-ps molecular dynamic simulations were performed on the mouse AChE-fasciculin complex coordinates (Protein Data Bank code 1KU6) with FM attached to Cys<sup>287</sup> to assess the effects of bound fasciculin on the torsional rotation of the succinimidylthioether (maleimide) tether arm connecting the fluorescein reporter group to the  $\alpha$ -carbonyl backbone. The hydrogens were added in InsightII prior to calculations, and the pH was set to 7.0. Sets of 21 molecular dynamic simulations were run with an SGI Octane computer (Silicon Graphics, Inc., Mountain View, CA) using the Discover 2.9 module within the InsightII 2000.1 computer program (Accelrys, San Diego, CA), both in the presence and absence of fasciculin. With the exception of the 19 AChE residues (from Gln<sup>279</sup> to Phe<sup>297</sup>) forming a surface loop, including FM attached to Cys<sup>287</sup>, all the atoms of mouse AChE and fasciculin were "frozen" during simulation. No water was present, the dielectric constant was set to 80, and the structure was not minimized prior to the

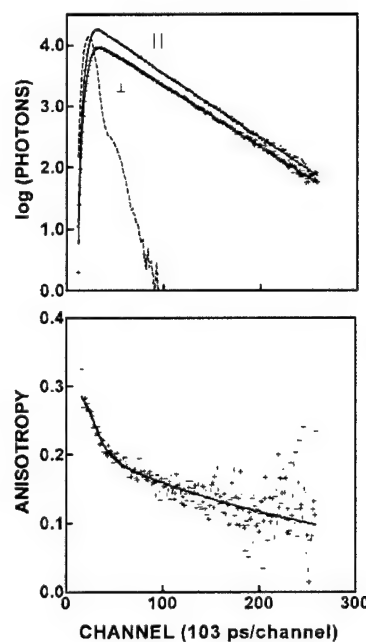


**FIG. 2. Emission and anisotropy decay of the FM-T249C mouse AChE mutant.** The upper panel shows the parallel (●) and perpendicular (+) emission decays (single data points), the fit of these data points to a single exponential decay equation (smooth lines), and the flash lamp profile (dashed line). The lower panel shows the time-resolved anisotropy decay (+), and a solid line through these points that was generated with the best-fit parameters (Table I) for a double exponential nonassociative decay model (Equation 6). The concentration of the labeled mutant was 150 nM.

subsequent molecular dynamic simulations. The protocol included initial equilibration of the system at 300 K, heating to 700 K, then slow cooling in 50-K increments back to 300 K, followed by minimization of the system.

## RESULTS

**Characterization of Unlabeled and Labeled Mutants**—SDS-PAGE analysis of the labeled and unlabeled mutants revealed a single, wide band of silver staining migrating with the variably glycosylated wild-type mouse AChE. Comparison of the steady-state emission from labeled mutants and parallel, wild-type AChE showed 6–7% nonspecific labeling. Based upon spectrophotometric ratios, stoichiometries of labeling for the labeled mutants were: T249C,  $0.2 \pm 0.04$ ; A262C,  $0.4 \pm 0.1$ ; and H287C,  $0.3 \pm 0.06$ . The  $K_m$ ,  $K_{ss}$ , and  $k_{cat}$  values for the cysteine mutants, the conjugated cysteine mutants, and wild-type AChE preparations were within experimental error of each other (data not shown). Because labeling was not stoichiometric, we also looked for a fractional component in the substrate concentration dependence curves that showed a different  $K_m$ , but were unable to detect two components in the curves. Moreover, titration with both tacrine and fasciculin produced virtually complete inhibition of catalytic activity of the labeled mutants with similar  $K_I$  values as observed for the wild-type AChE. Together, these findings indicate that labeled mutants fold correctly despite cysteine substitution and reporter group conjugation at these positions.

**Fluorescence Emission**—The uncorrected emission ( $517 \pm 1$  nm) and excitation ( $494 \pm 1$  nm) maxima for the conjugated enzymes are typical of fluorescein in an aqueous environment. Neither fasciculin nor tacrine had a significant effect upon the excitation or emission spectra of either the T249C or A262C conjugates; however, fasciculin red shifted slightly (2–3 nm) the emission spectrum and enhanced the apparent quantum yield by ~12% of the IAF-labeled H287C mutant, indicating a

TABLE I  
Effect of fasciculin and tacrine on the anisotropy decay parameters of FM-labeled mouse AChE mutants

Data are shown as mean ( $\pm$ S.D.) from at least three determinations. The vertically and orthogonally polarized emission decays were initially analyzed for the  $S(t)$  parameter (Equation 3), and then for the  $r(t)$  parameter (Equation 6) with the Globals Unlimited™ computer program. The experimental details are described under "Experimental Procedures." The mutants were present at the following concentrations: FM-T249C, 150 nM; FM-A262C, 190 nM; FM-H287C, 135 nM. To ensure saturation of enzyme with inhibitors, concentrations of fasciculin (4.7 to 5.7  $\mu$ M) and tacrine (40  $\mu$ M) were 10-fold over the total enzyme concentration and at least 100-fold over the  $K_i$  of tacrine or fasciculin for wild-type mouse AChE.

Mutant	Inhibitor	$r_0^a$	$f_{xb}^b$	$\phi_{fast}^c$	$\phi_{slow}^d$	$\psi_r^2 e$	$\tau^f$
T249C	None	$0.30 \pm 0.01$	$0.32 \pm 0.01$	$1.2 \pm 0.2$	ns	ns	ns
	Fasciculin	$0.30 \pm 0.01$	$0.33 \pm 0.01$	$1.3 \pm 0.3$	$35-49$	1.3	$4.16 \pm 0.01$
	Tacrine	$0.31 \pm 0.03$	$0.33 \pm 0.01$	$1.0 \pm 0.4$	$33-48$	1.2	$4.26 \pm 0.01$
A262C	None	$0.29 \pm 0.03$	$0.47 \pm 0.01$	$0.8 \pm 0.2$	$41-72$	1.5	$4.26 \pm 0.01$
	Fasciculin	$0.29 \pm 0.02$	$0.47 \pm 0.01$	$0.8 \pm 0.2$	$43-71$	1.4	$4.27 \pm 0.01$
	Tacrine	$0.28 \pm 0.02$	$0.46 \pm 0.01$	$0.8 \pm 0.2$	$40-63$	1.5	$4.27 \pm 0.01$
H287C	None	$0.30 \pm 0.01$	$0.50 \pm 0.01$	$0.9 \pm 0.1$	$31-44$	1.3	$4.11 \pm 0.01$
	Fasciculin	$0.30 \pm 0.01$	$0.34 \pm 0.01$	$1.8 \pm 0.1$	$36-49$	1.2	$4.28 \pm 0.02$
	Tacrine	$0.32 \pm 0.03$	$0.49 \pm 0.01$	$0.9 \pm 0.2$	$29-41$	1.4	$4.10 \pm 0.01$

<sup>a</sup> The time 0 anisotropy.

<sup>b</sup> The fraction of the observed anisotropy decay associated with the fast depolarization processes.

<sup>c</sup> Fast rotational correlation time.

<sup>d</sup> The range of the slow rotational correlation times that yield  $\chi_r$  values 5% above the minimum.

<sup>e</sup> The reduced  $\chi^2$ .

<sup>f</sup> Geometric averaged lifetimes ( $\Sigma \alpha_i \tau_i$ , where  $\Sigma \alpha_i = 1$ ).

ligand-induced change of the microenvironment around the reporter group attached to the H287C site of conjugation (data not shown).

**Estimation of Rotational Correlation Times**—From the gel filtration measurements, wild-type AChE was estimated to have a Stokes' radius of 51 Å. Substituting this value into the Stokes-Einstein equation yielded a rotational correlation time of 128 ns.

**Time-resolved Fluorescence Anisotropy of FM Conjugates**—For brevity, the emission and the anisotropy decay profiles of only the FM-T249C conjugate are illustrated (Fig. 2). The time course of emission decay of each mutant examined was well fit to a biexponential decay model. For simplicity, only the geometric averaged excited state lifetimes are summarized (Table I) and ranged between 4.11 and 4.26 ns. The actual range of short and long wavelength emission lifetimes for the various nonliganded mutants were 4.26–4.82 and 2.98–4.01 ns, respectively. The amplitudes of the longer lifetime components ranged between 31 and 87% of the total decay amplitude (data not shown).

Time-resolved fluorescence anisotropy directly monitors the reorientation of the emission transition dipole moment of a fluorescent reporter group in the picosecond/nanosecond time domain. When conjugated to a specific protein side chain, the  $I_{||}(t)$  and  $I_{\perp}(t)$  emission profiles are usually well fit to a model-free nonassociative biexponential equation (Equation 6). Under conditions where the protein-conjugated reporter group diffuses relatively freely at the end of its tether arm and where there are no significant internal motions in the time domain between the whole body diffusion and local backbone movements, the main types of motions (tether arm, local backbone, and whole body) should be resolvable from each other and are represented in the basic elements of the biexponential equation (time 0 amplitude,  $r_0$ ), the rotational correlation time, and fractional amplitude of the fast components ( $\phi_{fast}$  and  $f_{xb}$ ) and slow rotational correlation time ( $\phi_{slow}$ ) processes (32). In the present case, the whole body rotational correlation time predicted by the Stokes-Einstein equation (128 ns) is slower than the observed  $\phi_{slow}$  values, which ranged between 31 and 72 ns (Table I). This disparity may reflect the existence of internal motions of intermediate decay rates that obscure the depolarization from whole body rotational diffusion or arise from the inherent limitation of quantifying rotational diffusion times that are more than 10 times slower than the emission lifetime of the reporter group.

Visual comparison of the time-resolved anisotropy decays of the three mutants (Fig. 3) shows that the fluorescein attached to A262C and H287C mutants reorients (depolarizes) more rapidly than the fluorescein attached to the T249C mutant, but with similar time 0 anisotropy values. Quantitatively, these similarities and differences were primarily observed in the fractional amplitude of the measurable fast decay processes ( $f_{xb}$ ). The  $f_{xb}$  values for the FM-A262C and FM-H287C conjugates represent about half of the resolvable anisotropy decay (0.47 and 0.50, respectively), but only a third (0.32) of the FM-T249C mutant. The values for the time 0 anisotropy ( $r_0$ ; range 0.29–0.30) and the fast rotational correlation time ( $\phi_{fast}$ ; range 0.8–1.2 ns) were essentially the same for all the mutants studied. Taken together, these results indicate a high level of  $\alpha$ -carbon flexibility around each residue examined, although the Thr<sup>249</sup> residue is significantly less flexible than the Ala<sup>262</sup> and His<sup>287</sup> residues.

**Influence of Ligand Binding on Anisotropy Decay of FM Conjugates**—Active and peripheral site inhibitors, tacrine and fasciculin, respectively, were bound to AChE at a concentration of at least 100 times their dissociation constants to ensure >99% occupation (23, 33). Alteration in the decay of anisotropy was observed only upon binding of fasciculin to FM-H287C mutant (Table I and Fig. 4). Specifically, fasciculin reduced the amplitude of the fast decay process by 32% and doubled the fast decay time without significantly affecting either the time 0 anisotropy or the slow decay, presumably reflecting whole body rotational diffusion (Table I). Additionally, some fasciculin-induced change in the microenvironment of the fluorophore is evident, because fasciculin increased slightly the emission lifetime (from 4.11 to 4.28 ns, Table I) and caused a 2–3-nm red shift in the emission maximum of the fluorescein (data not shown). These results suggest that, whereas the microenvironment around the reporter group changed slightly, the tether arm motions of the reporter group were not significantly hindered by a direct interaction with bound fasciculin. The fasciculin-induced alterations in anisotropy decay, therefore, result from reduced segmental flexibility around H287C at the edge or rim of the active site gorge.

This interpretation is supported by molecular dynamic simulations of the mouse AChE coordinates with FM attached to H287C in both the presence and absence of fasciculin. Visual examination of the pattern of positions of FM at the end of these simulations (Fig. 5) shows only a small difference pro-

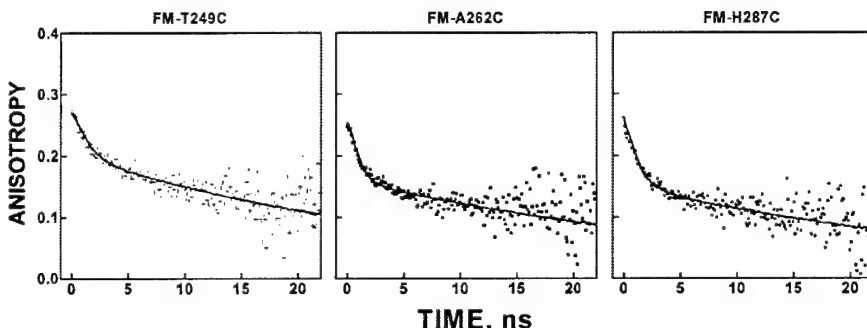


**FIG. 3. Anisotropy decays of FM-T249C, FM-A262C, and FM-H287C mouse AChE mutants.** Shown are the time-resolved anisotropy decays (single data points), and the solid lines through these points that were generated with the best-fit parameters (Table I) for a double exponential nonassociative decay model (Equation 6). The peak of the flash lamp profile arbitrarily defined the zero time point. The concentrations of FM-T249C (+), FM-A262C (■), and FM-H287C (●) were 150, 190, and 135 nm, respectively.

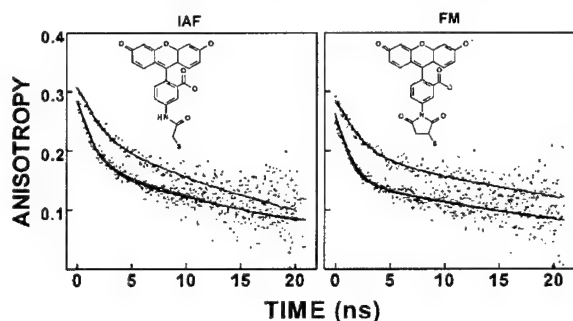


**FIG. 4. Effect of fasciculin and tacrine on the anisotropy decay of the FM- and IAF-labeled H287C mutants.** The time-resolved anisotropy decay (single data points) and the solid lines through these points were generated with the best-fit parameters (Table II) for a double exponential nonassociative decay model (Equation 6). Data points represent enzyme without inhibitors (●), with tacrine (+), or with fasciculin (□). The peak of the flash lamp profile arbitrarily defined the zero time point. The concentrations of FM-H287C, IAF-H287C, fasciculin, and tacrine were 135 nm, 145 nm, 4.7  $\mu$ M, and 40  $\mu$ M, respectively.

duced by the presence of fasciculin. The pattern of final positions of FM appears slightly more spherical in the absence of fasciculin. Quantitatively, the mean distance in movements of the  $C_{\alpha}$  of Cys<sup>287</sup> from its initial position was  $2.6 \pm 1.9$  Å (for FM-mouse AChE alone) and  $0.96 \pm 0.59$  Å for FM-mouse AChE complexed to fasciculin. These findings support the experimental results that fasciculin significantly lowers flexibility of the  $C_{\alpha}$  at position 287.

**Anisotropy Decay with IAF**—To confirm that the changes in anisotropy decay induced by fasciculin were not unique to the tether arm, we also examined the influence of fasciculin and tacrine on the anisotropy decay parameters of an IAF-H287C mutant conjugate. The anisotropy decay profile of this conjugate was very similar to the FM conjugated to the same position, where fasciculin, but not tacrine, reduced the amplitude and slowed the rate of the fast depolarization processes (Fig. 4 and Table II). Thus, the influence of fasciculin on the decay parameters appears independent of the tether arm joining fluorescein to the cysteine side chain. Here, the length of the tether arms of both conjugates are the same, but the FM derivative with its succinimidylthioether linkage should have less torsional freedom than the acetamidothioether linkage of the IAF conjugate.

#### DISCUSSION

The apparent paradox of diffusion-limited catalysis of esters occurring within the confines of a narrow gorge in AChE has prompted computational and mutational investigations into

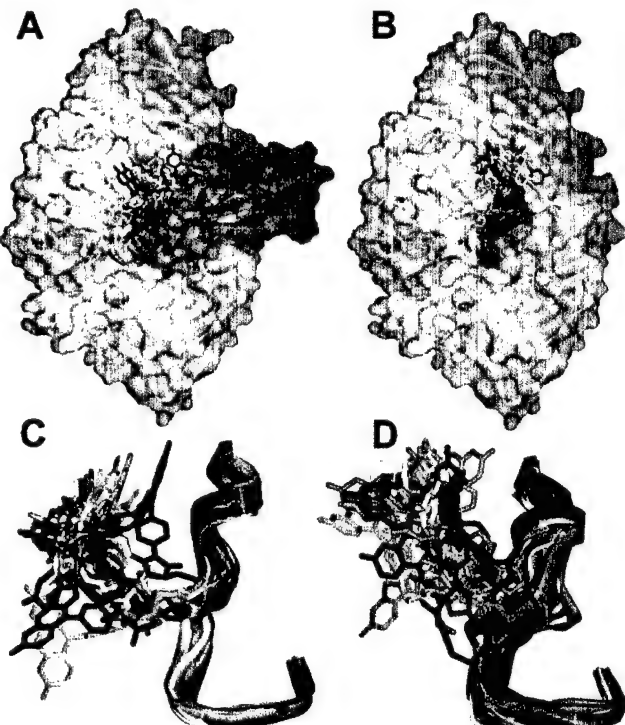


**FIG. 5. Molecular dynamic simulations of the effect of fasciculin binding on the torsional movements of Cys<sup>287</sup> and attached FM.** Twenty-one 3-ps simulations were performed on the x-ray coordinates of the mouse AChE-fasciculin complex with FM attached to Cys<sup>287</sup> in the presence (A and C) and absence (B and D) of fasciculin as described under "Experimental Procedures." Only the residues between Gln<sup>279</sup> and Phe<sup>297</sup> and attached FM were allowed to move; the rest of mouse AChE and fasciculin atoms were "frozen" for the simulations. The positions of the FM bonds and the Gln<sup>279</sup> to Phe<sup>297</sup> backbone are shown in a different color for each simulation. Transparent Connolly surfaces of mouse AChE and fasciculin are shown in gray and brown, respectively. In panels C and D, the views of the positions of the FM bonds and the Gln<sup>279</sup> to Phe<sup>297</sup> backbone are rotated by  $\sim 60^\circ$  around the vertical axis and enlarged from the panel (A and B) above.

the dynamics of substrate entry and product egress from the active center. Although alternative entry routes have been suggested from molecular dynamic calculations (9–11), mutational studies have not supported additional entry or exit portals for the charged substrate or product (12, 13). Accordingly, more recent computational studies have been directed to analyzing how conformational flexibility within AChE may give rise to greater access to the active center than is evident in the static crystal structure (16). The current investigation of decay of anisotropy of site-directed fluorophores presents an ap-

**TABLE II**  
*Effect of fasciculin and tacrine on the anisotropy decay parameters of IAF-labeled H287C mouse AChE mutant*

Data are shown as mean ( $\pm$ S.D.) from at least three determinations. The mutant was present at a concentration of 145 nM. To ensure saturation of enzyme with inhibitors, concentrations of fasciculin (4.7  $\mu$ M) and tacrine (40  $\mu$ M) were 10-fold over the total enzyme concentration and at least 100-fold over the  $K_i$  of tacrine or fasciculin for wild-type mouse AChE.

Condition	$r_0^a$	$f_{xb}^b$	$\phi_{fast}^c$	$\phi_{slow}^d$	$\psi_r^{2,e}$	$\tau^f$
None	0.32 $\pm$ 0.02	0.42 $\pm$ 0.01	ns	22–29	1.3	3.83 $\pm$ 0.02
Fasciculin	0.34 $\pm$ 0.01	0.29 $\pm$ 0.01	1.5 $\pm$ 0.3	23–29	1.3	4.04 $\pm$ 0.03
Tacrine	0.30 $\pm$ 0.02	0.44 $\pm$ 0.01	1.3 $\pm$ 0.2	23–30	1.4	3.80 $\pm$ 0.01

<sup>a</sup> The time zero anisotropy.

<sup>b</sup> The fraction of the observed anisotropy decay associated with the fast depolarization processes.

<sup>c</sup> Fast rotational correlation time.

<sup>d</sup> The range of the slow rotational correlation times that yield  $\psi_r^2$  values 5% above the minimum.

<sup>e</sup> The reduced  $\psi_r^2$ .

<sup>f</sup> Geometric averaged lifetimes ( $\Sigma \alpha_i \tau_i$ , where  $\Sigma \alpha_i = 1$ ).

proach to extending analysis of conformation from static equilibrium measurements of fluorescence to time-resolved analysis in the picosecond to nanosecond time frame.

Time-resolved fluorescence anisotropy enables one to monitor directly reorientation of a fluorophore in the time frame of several excited state lifetimes. When a fluorophore is tethered to the macromolecule, depolarization is achieved by multiple relaxation modes that most likely occur in distinct time frames. Torsional motion around the tether arm, if unhindered, will occur in a subnanosecond time frame, not resolvable with commercial instruments. Restriction of motion around the tether will diminish the amplitude and slow the decay rate of this phase. Segmental motion of a domain within the molecule containing the fluorophore will give rise to a fast, but usually measurable depolarization; the rate and amplitude of which will depend upon the mass of the domain, the extent of the angular excursion, and the orientation of the absorbance/emission transition moments relative to the diffusion cone angle. Finally, global motion of the entire protein where the fluorophore is affixed to the macromolecule will in most cases produce the slowest rate of anisotropy decay. The latter will be governed by the multiple rotational correlation times of the macromolecule, which are not resolvable unless the molecule is highly dimensionally asymmetric.

**Decay of Anisotropy of the FM Conjugates**—The structure of the small  $\Omega$ -loop bounded by the disulfide bond at Cys<sup>257</sup> and Cys<sup>272</sup> is not well resolved in AChE crystal structures unless the loop is stabilized by interaction with the symmetry related molecule (34). The large thermal or *B* factors for this region in the crystal structures suggest that the tip of this disulfide loop is either highly flexible or experiences static disorder in the crystal (35). Indeed, when FM is conjugated to A262C, the amplitudes of the very fast ( $r_i - r_0$ ) and fast ( $r_0 f_{xb}$ ) decay phases represent ~17 and 39% of the total anisotropy decay, where  $r_i$  is the fundamental anisotropy of the fluorophore. Hence, independent motions of the fluorescein tether arm through torsional motion ( $r_i - r_0$ ) and flexible domain motion ( $r_0 - f_{xb}$ ) in the AChE molecule are the dominant modes of anisotropy decay at the 262 position.

When fluorescein is attached to the H287C mutant, we note similar amplitudes for the very rapid and rapid decay phases, 14 and 43%. Again, the major mode of depolarization of the fluorescein conjugated at position 287 occurs by modes other than the global rotation of the molecule. The average crystallographic *B* factors for the  $\alpha$ -carbon chain atoms of residue His<sup>287</sup> are far smaller than that seen for residue 262 (Table III). The disparity between *B* factors at the 287 and 262 positions, in the face of similar large components of rapid depolarization of the attached fluorescein, suggests either that His<sup>287</sup> is stabilized in the crystalline state or that the large average *B* factors associated with Ala<sup>262</sup> arise from a equilibrium (*i.e.* static dis-

**TABLE III**  
*Comparison of the average main chain atom crystallographic *B* factors for residues Thr<sup>249</sup>, Ala<sup>262</sup>, and His<sup>287</sup>*

Residue	<i>B</i> factor <sup>a</sup>	Normalized <i>B</i> factor <sup>b</sup>
Thr <sup>249</sup>	19.6	-1.74
Ala <sup>262</sup>	79.2	1.83
His <sup>287</sup>	33.9	-0.88

<sup>a</sup> The *B* factors listed here are the average main chain atom values (amino nitrogen, carboxy carbon, and  $\alpha$  carbon) of the indicated residue for chain A of the tetrameric crystal structure of mouse AChE (Protein Data Bank code 1MAA (34)).

<sup>b</sup> Calculated by subtracting the average main-chain atom *B* factors of all residues forming chain A (average equals 48.59) from the average main chain atoms of the indicated residue and then dividing by the standard deviation of the *B* factors of all residues forming chain A (standard deviation equals 16.67).

order) between multiple positions of the small  $\Omega$ -loop in the crystal structure. Stabilization of His<sup>287</sup> by crystallization forces could be part of the process that favors a closed gorge state in the crystal and explains why no open gorge crystal structures of AChE have been observed.

By contrast, when fluorescein is conjugated at T249C, a smaller fraction of the anisotropy decay occurs by the rapid modes, 14 and 27%. This difference most likely arises from a more structured  $\alpha$ -carbon backbone in the vicinity of Thr<sup>249</sup>, a region shown to be helical in the crystal structure (Ala<sup>241</sup>-Val<sup>255</sup>) (34).

**Influence of Ligand Binding on the Anisotropy Decay Parameters**—To examine whether ligand binding influences anisotropy decay and hence dynamic parameters at various locations near the active center gorge, we initially selected two ligands whose complexes with AChE have been determined crystallographically. Tacrine binds at the active center at the base of the gorge with its aromatic ring system stacked between the indole moiety of Trp<sup>84</sup> and the phenyl ring of Phe<sup>330</sup> in Torpedo AChE (36) corresponding to Trp 86 and Tyr 337 of mouse AChE. In fact, the latter residue shows a conformational movement associated with tacrine binding causing a parallel stacking of the tacrine ring between the two aromatic side chains. By contrast, fasciculin, a peptide of 61 amino acids, associates at the mouth of the gorge greatly limiting ligand access to the catalytic center (4, 37). The AChE crystal structure shows that His<sup>287</sup> approaches a van der Waals distance to the bound fasciculin residues.

The binding of tacrine, despite it being inhibitory to all of the conjugated enzymes, has no effect on the lifetime or anisotropy decay parameters for fluorescein conjugated at positions 249, 262, and 287. Hence, this result would indicate that ligand binding does not cause a global conformation change that would be evident at these three disparate locations on the macromolecule. However, this finding does not preclude li-

gands inducing changes in conformation and side chain mobility in regions of the AChE molecule that are not reflected in our three labeling positions (11, 18, 19, 38).

Fasciculin, which binds with a  $K_d$  for the wild-type enzyme in the range of 4 pm (33) and whose crystal structure shows a van der Waals peptide to protein contact area of 1100 Å<sup>2</sup> (4), also does not affect the anisotropy decay parameters at positions 262 and 249. However, conjugated fluorescein at position 287 shows a small change in the Stokes' shift and emission lifetime, and a major change in the decay of anisotropy. The reduction of the amplitudes of the rapid decay phases and the slowing of the rapid decay phase likely reflect a small torsional restraint on the tethered fluorescein and a stabilization of movement of the loop encompassing residue 287 produced by the bound fasciculin.

The differential influence of fasciculin on the anisotropy decay of three fluorophores positioned in distinct locations on the AChE molecule, again, indicates that this ligand does not induce global changes in the conformational dynamics of the enzyme. Based on the limited number of sites examined, fasciculin appears to have stabilized a local domain of the molecule reducing the intrinsic flexibility in the region around His<sup>287</sup> and probably in neighboring areas of direct contact.

**Implications**—These results combined with our previous analysis of the segmental dynamics of three sites on the Cys<sup>69</sup>–Cys<sup>96</sup> Ω-loop (20) paint a consistent picture of AChE with conformationally active surface backbone elements whose movements are poorly coupled to one another. Such a conformationally dynamic structure supports a model for transient gorge openings that is dominated by random segmental movements.

Also, the above studies further demonstrate the potential of time-resolved studies of fluorescence anisotropy to examine molecular motion in distinct regions of a molecule and its ligand-associated complexes whose overall structural template has been delineated through x-ray crystallography. The principal advantages of the technique stem from measurements conducted in solution and under conditions simulating ligand binding *in situ*. Cysteine substitution mutagenesis enables one to select individual side chains in strategic regions of the molecule and examine each locus in a systematic fashion with multiple fluorophores. The individual fluorophores selected for conjugation can differ in lifetime, spectroscopic parameters, and capacity to modify the substituted cysteines. Hence, a comprehensive analysis of time-resolved fluorescence typically requires analysis of a variety of residue positions often with more than a single probe. This presents a particular challenge for larger extracellular proteins because their production usually requires eukaryotic expression systems that typically yield limited quantities of protein. Also, glycosylation and intrinsic disulfide bonds characteristic of extracellular proteins may add further complexity to achieving appropriate expression. Our study establishes that the residue-directed fluorophore approach to labeling can yield valuable information even when the macromolecule is a large glycosylated protein.

In summary, we have extended our previous study of the conformational dynamics of the AChE Cys<sup>69</sup>–Cys<sup>96</sup> Ω-loop, a segment that forms the outer wall of the active center gorge, to include three additional sites positioned roughly in a line that starts at the rim of the gorge across from the Ω-loop and projecting radially ~20 Å away from the gorge. Similar to our previous study, site-directed labeling in conjunction with time-resolved fluorescence anisotropy was utilized. The results reveal both distinct modes of molecular motion as well as a high

degree of backbone flexibility. Additionally, there appears to be limited coupling of the conformational fluctuations between the sites examined, because ligand binding only affected the one site that was in close proximity to the bound inhibitor. This indicates that ligand association did not produce global changes in the conformational flexibility of the enzyme. Moreover, these results combined with our previous analysis of the conformational dynamics of the Cys<sup>69</sup>–Cys<sup>96</sup> Ω-loop add support to the view that the area around the active center gorge rim is conformationally active and is consistent with a model for transient gorge openings that are dominated by random segmental movements.

## REFERENCES

- Rosenberry, T. L. (1975) *Adv. Enzymol. Relat. Areas Mol. Biol.* **43**, 103–218
- Quinn, D. M. (1987) *Chem. Rev.* **253**, 955–979
- Sussman, J. L., Harel, M., Frolov, F., Oefner, C., Goldman, A., Toker, L., and Silman, I. (1991) *Science* **253**, 872–879
- Bourne, Y., Taylor, P., and Marchot, P. (1995) *Cell* **83**, 503–512
- Kryger, G., Harel, M., Giles, K., Toker, L., Velan, B., Lazar, A., Kronman, C., Barak, D., Ariel, N., Shafferman, A., Silman, I., and Sussman, J. L. (2000) *Acta Crystallogr. Sect. D* **56**, 1385–1394
- Ripoll, D. R., Faerman, C. H., Axelsen, P. H., Silman, I., and Sussman, J. L. (1993) *Proc. Natl. Acad. Sci. U. S. A.* **90**, 5128–5132
- Radić, Z., Kirchhoff, P. D., Quinn, D. M., McCammon, J. A., and Taylor, P. (1997) *J. Biol. Chem.* **272**, 23265–23277
- Włodek, S. T., Shen, T., and McCammon, J. A. (2000) *Biopolymers* **53**, 265–271
- Gilson, M. K., Straatsma, T. P., McCammon, J. A., Ripoll, D. R., Faerman, C. H., Axelsen, P. H., Silman, I., and Sussman, J. L. (1994) *Science* **263**, 1276–1278
- Włodek, S. T., Clark, T. W., Scott, L. R., and McCammon, J. A. (1997) *J. Am. Chem. Soc.* **119**, 9513–9522
- Tara, S., Straatsma, T. P., and McCammon, J. A. (1999) *Biopolymers* **50**, 35–43
- Kronman, C., Ordentlich, A., Barak, D., Velan, B., and Shafferman, A. (1994) *J. Biol. Chem.* **269**, 27819–27822
- Faerman, C., Ripoll, D., Bon, S., Le Feuvre, Y., Morel, N., Massoulie, J., Sussman, J. L., and Silman, I. (1996) *FEBS Lett.* **386**, 65–71
- Zhou, H. X., Włodek, S. T., and McCammon, J. A. (1998) *Proc. Natl. Acad. Sci. U. S. A.* **95**, 9280–9283
- Shen, T. Y., Tai, K., and McCammon, J. A. (2001) *Phys. Rev. E Stat. Nonlin. Soft Matter Phys.* **63**, 041902
- Tai, K., Shen, T., Borjesson, U., Philippopoulos, M., and McCammon, J. A. (2001) *Biophys. J.* **81**, 715–724
- Ravelli, R. B., Raves, M. L., Ren, Z., Bourgeois, D., Roth, M., Kroon, J., Silman, I., and Sussman, J. L. (1998) *Acta Crystallogr. Sect. D* **54**, 1359–1366
- Shi, J., Boyd, A. E., Radić, Z., and Taylor, P. (2001) *J. Biol. Chem.* **276**, 42196–42204
- Shi, J., Radić, Z., and Taylor, P. (2002) *J. Biol. Chem.* **277**, 43301–43308
- Shi, J., Tai, K., McCammon, J. A., Taylor, P., and Johnson, D. A. (2003) *J. Biol. Chem.* **278**, 30905–30911
- Steiner, R. F. (1991) in *Topics in Fluorescence Spectroscopy* (Lakowicz, J. R., ed) Vol. 2, Plenum Press, New York
- Boyd, A. E., Marnett, A. B., Wong, L., and Taylor, P. (2000) *J. Biol. Chem.* **275**, 22401–22408
- Radić, Z., Pickering, N. A., Vellom, D. C., Camp, S., and Taylor, P. (1993) *Biochemistry* **32**, 12074–12084
- Berman, J. D., and Young, M. (1971) *Proc. Natl. Acad. Sci. U. S. A.* **68**, 395–398
- De la Hoz, D., Doctor, B. P., Ralston, J. S., Rush, R. S., and Wolfe, A. D. (1986) *Life Sci.* **39**, 195–199
- Marchot, P., Ravelli, R. B., Raves, M. L., Bourne, Y., Vellom, D. C., Kanter, J., Camp, S., Sussman, J. L., and Taylor, P. (1996) *Protein Sci.* **5**, 672–679
- Taylor, P., Jones, J. W., and Jacobs, N. M. (1974) *Mol. Pharmacol.* **10**, 78–92
- Ellman, G. L., Courtney, K. D., Andres, V. J., and Featherstone, R. M. (1961) *Biochem. Pharmacol.* **7**, 88–95
- Levy, D., and Ashani, Y. (1986) *Biochem. Pharmacol.* **35**, 1079–1085
- Yguerabide, J. (1972) *Methods Enzymol.* **26**, 498–578
- Siegel, L. M., and Monty, K. J. (1966) *Biochim. Biophys. Acta* **112**, 346–362
- Gangal, M., Cox, S., Lew, J., Clifford, T., Garrod, S. M., Aschbacher, M., Taylor, S. S., and Johnson, D. A. (1998) *Biochemistry* **37**, 13728–13735
- Radić, Z., Duran, R., Vellom, D. C., Li, Y., Cervenansky, C., and Taylor, P. (1994) *J. Biol. Chem.* **269**, 11233–11239
- Bourne, Y., Taylor, P., Bougis, P. E., and Marchot, P. (1999) *J. Biol. Chem.* **274**, 2963–2970
- Glusker, J. P., and Trueblood, K. N. (1985) *Crystal Structure Analysis: A Primer*, 2nd Ed., Oxford University Press, New York
- Harel, M., Schalk, I., Ehret-Sabatier, L., Bouet, F., Goeldner, M., Hirth, C., Axelsen, P. H., Silman, I., and Sussman, J. L. (1993) *Proc. Natl. Acad. Sci. U. S. A.* **90**, 9031–9035
- Harel, M., Klewegt, G. J., Ravelli, R. B., Silman, I., and Sussman, J. L. (1995) *Structure* **3**, 1355–1366
- Tara, S., Helms, V., Straatsma, T. P., and McCammon, J. A. (1999) *Biopolymers* **50**, 347–359

## Structural Characterization of Recombinant Soluble Rat Neuroligin 1: Mapping of Secondary Structure and Glycosylation by Mass Spectrometry<sup>†</sup>

Ross C. Hoffman,<sup>‡,§</sup> Lori L. Jennings,<sup>\*,§,¶</sup> Igor Tsigelny,<sup>§</sup> Davide Comoletti,<sup>§</sup> Robyn E. Flynn,<sup>§</sup> Thomas C. Sudhof,<sup>||</sup> and Palmer Taylor<sup>§</sup>

*Department of Pharmacology and Howard Hughes Medical Institute Mass Spectrometry Facility, University of California, San Diego, La Jolla, California 92093, and Department of Molecular Genetics and Howard Hughes Medical Institute, University of Texas Southwestern Medical Center, Dallas, Texas 75235*

Received July 18, 2003; Revised Manuscript Received December 4, 2003

**ABSTRACT:** Neuroligins (NLs) are a family of transmembrane proteins that function in synapse formation and/or remodeling by interacting with  $\beta$ -neurexins ( $\beta$ -NXs) to form heterophilic cell adhesions. The large N-terminal extracellular domain of NLs, required for  $\beta$ -NX interactions, has sequence homology to the  $\alpha/\beta$  hydrolase fold superfamily of proteins. By peptide mapping and mass spectrometric analysis of a soluble recombinant form of NL1, several structural features of the extracellular domain have been established. Of the nine cysteine residues in NL1, eight are shown to form intramolecular disulfide bonds. Disulfide pairings of Cys 117 to Cys 153 and Cys 342 to Cys 353 are consistent with disulfide linkages that are conserved among the family of  $\alpha/\beta$  hydrolase proteins. The disulfide bond between Cys 172 and Cys 181 occurs within a region of the protein encoded by an alternatively spliced exon. The disulfide pairing of Cys 512 and Cys 546 in NL1 yields a structural motif unique to the NLs, since these residues are highly conserved. The potential N-glycosylation sequons in NL1 at Asn 109, Asn 303, Asn 343, and Asn 547 are shown occupied by carbohydrate. An additional consensus sequence for N-glycosylation at Asn 662 is likely occupied. Analysis of N-linked oligosaccharide content by mass matching paradigms reveals significant microheterogeneous populations of complex glycosyl moieties. In addition, O-linked glycosylation is observed in the predicted stalk region of NL1, prior to the transmembrane spanning domain. From predictions based on sequence homology of NL1 to acetylcholinesterase and the molecular features of NL1 established from mass spectrometric analysis, a novel topology model for NL three-dimensional structure has been constructed.

NLs<sup>1</sup> (1–4) comprise a family of membrane proteins that interact with  $\beta$ -NXs (1–3) to function as heterophilic cell adhesion molecules (4). NL1 localizes to postsynaptic densities of excitatory synapses (5). The production of NL1 and NL2 in nonneuronal cells has been shown to induce the *in vitro* formation of presynaptic structures in axons of cocultured neurons from the central nervous system (6). NXs present in presynaptic elements of neuronal pontine explants have been shown to function as NL partners in synapse formation; stimulation of synaptic differentiation by NL1 recruits NXs to newly forming synapses (7).

NLs are type 1 membrane proteins believed to be composed of five distinct domains: a cleaved N-terminal

signal peptide, a large extracellular domain, a linker domain resembling an O-glycosylation cassette, a single transmembrane region, and a cytoplasmic C-terminal tail (1). An N-terminal hydrophobic sequence of NLs, followed by a typical cleavage site, was suggestive of a signal peptide and confirmed by amino acid sequence analysis (2). The large extracellular domain of NLs shares significant sequence identity (32–36%) with certain members (e.g., AChE) of the  $\alpha/\beta$  hydrolase fold protein superfamily (1, 8). However, the NLs lack amino acid residues critical for the characteristic catalytic triad that confers hydrolase activity. Through comparisons with the crystal structure of AChE (9, 10), tertiary protein structures for NLs have been proposed (1, 2) and topology models constructed (7). The hydrolase homology domain of NLs is required for their interaction with  $\beta$ -NXs, whereas the intracellular C-terminus region contains a PDZ binding domain and functions to associate with partnering proteins (6).

NLs contain several potential N-linked glycosylation sequons that result in heterogeneously glycosylated proteins. An O-carbohydrate-rich stalk is predicted in the linker region between the hydrolase homology domain and the transmembrane region, on the basis of the homology to O-linked glycosylation cassettes in other cell surface receptors (2). For NL1, purified from rat brain by affinity chromatography

<sup>†</sup> This work was supported by Grants USPHS P42-ES10337 and R37 GM-18360 to P.T.

\* To whom correspondence should be addressed: Phone: (858) 534-1366. Fax: (858) 534-8248. E-mail: ljenning@ucsd.edu.

<sup>‡</sup> Howard Hughes Medical Institute Mass Spectrometry Facility, University of California, San Diego.

<sup>§</sup> Department of Pharmacology, University of California, San Diego.

<sup>||</sup> University of Texas Southwestern Medical Center.

<sup>¶</sup> These authors contributed equally to this work.

<sup>1</sup> Abbreviations: AChE, acetylcholinesterase; ACN, acetonitrile; AMU, atomic mass unit; CNBr, cyanogen bromide; DMEM, Dulbecco's modified Eagle's medium; DTT, dithiothreitol; IAA, iodoacetic acid; LC-MS, liquid chromatography–mass spectrometry; *m/z*, mass (Da) to charge ratio; NLs, neuroligins; NXs, neurexins; TIC, total ion current; TFA, trifluoroacetic acid; TOF, time of flight; 4-VP, 4-vinylpyridine; XIC, extracted ion current.

with immobilized  $\beta$ -neurexin, deglycosylation with glycohydrolases for N- and O-linked sugars accounted for the approximate 21 kDa size difference between the native protein and its primary translation product (1).

The disulfide bonding pattern of NLs has been proposed from sequence homology to the  $\alpha/\beta$  hydrolase fold protein superfamily (1, 2), since four of the six disulfide-bonded cysteines in AChE are conserved in all esterases in this family. An alternatively spliced sequence in NL1 contains two cysteines that may form an internal disulfide loop. The alternatively spliced regions of NLs are found at loop positions in the AChE crystal structure (9, 10) and may indicate these regions form a tertiary structure of extended surface loops. NLs contain a conserved cysteine residue between predicted disulfide loops that does not appear involved in intermolecular disulfide bonds, since NLs have similar migration when resolved by reducing and nonreducing SDS gel electrophoresis (2). An additional cysteine pair is present in the C-terminal region of the ectodomain, conserved among the NLs, but in a region where sequence identity to the hydrolase protein family diverges.

Although the configuration of the NLs has been predicted on the basis of the primary sequence, consensus sequons for glycosylation, and homology to esterases and other  $\alpha/\beta$  hydrolase proteins, direct biochemical evidence establishing structural features of NLs has yet to be reported. We have made a detailed structural characterization of soluble NL (NL1-691), truncated prior to the membrane-spanning region, that contains the entire hydrolase-like domain and the perimembrane linker region. A systematic approach of peptide mapping and mass spectrometric analysis has been performed to (i) deduce disulfide pairing of cysteine residues, (ii) determine the occupancy and major oligosaccharide content of predicted N-linked glycosyl sequons, and (iii) establish the presence of O-linked carbohydrates in the Ser/Thr-rich region near the membrane-spanning segment.

## MATERIALS AND METHODS

**Chemicals and Reagents.** Sequence-grade modified trypsin was purchased from Promega (Madison, WI), and endoproteinase Glu-C was from Roche Diagnostics (Indianapolis, IN). Peptide-N-glycosidase F (PNGase F), endo- $\alpha$ -N-acetylgalactosaminidase ( $O$ -glycanase), sialidase A,  $\beta$ -(1-4)-galactosidase,  $\beta$ -N-acetylhexosaminidase, and  $\alpha$ -(1-2,3,4,5,6)-fucosidase were purchased from Prozyme (San Leandro, CA). pFLAG-CMV-1 expression plasmid, M2 anti-FLAG immunoaffinity gel, and other general chemical supplies were purchased from Sigma (St. Louis, MO). Mutagenesis of recombinant DNA constructs was performed with a Stratagene Quickchange kit (San Diego, CA). Dulbecco's modified Eagle's medium (DMEM) and pcDNA3 expression plasmid were purchased from Invitrogen (Carlsbad, CA). Ultraculture serum-free medium was purchased from BioWhittaker (Walkersville, MD). Centrifugal spin filter devices were purchased from Millipore (Bedford, MA).

**Expression and Purification.** The sequence encoding rat NL1 was subcloned into pFLAG-CMV1 expression plasmid to generate a construct that encoded a protrypsin leader peptide, a FLAG octapeptide epitope tag at the N-terminus, a 10-residue linker peptide, and NL1. The coding sequence for NL1 begins at Gln 46, the first amino acid residue of

the mature protein (1, 2). The construct was subcloned into pcDNA3 expression plasmid to generate NL1/FLAG-pcDNA3. For production of soluble NL1, a stop codon was introduced at Tyr 692 to truncate the protein prior to the transmembrane-spanning segment. Soluble recombinant rat NL1 (NL1-691) was produced by transfection of NL1/FLAG-pcDNA3 expression plasmid into human embryonic kidney (HEK293) cells, maintained in DMEM with 10% fetal bovine serum at 37 °C, 10% CO<sub>2</sub>. By selection of expressing cells using G418 resistance, cultures were established that secreted milligram quantities of soluble NL1 into the growth media. FLAG-tagged NL1-691 was purified from serum-free growth media by immunoaffinity chromatography on M2 anti-FLAG gel according to the manufacturer's instructions. For subsequent analysis by mass spectrometry, purified NL1-691 was buffer exchanged into 50 mM NH<sub>4</sub>HCO<sub>3</sub>, pH 7.8, by spin filtration, aliquoted, lyophilized, and stored at -20 °C. Purification to homogeneity was confirmed by SDS-polyacrylamide gel electrophoresis and silver staining (results not shown). The protein quantity was determined by the method of Bradford (11).

**Trypsin and Endoproteinase Glu-C Digestion.** NL1-691 (50 µg) was digested with sequence-grade modified trypsin using the conditions 1.0 mg/mL protein in 100 mM Tris-HCl, pH 8.0, and 1:50 trypsin/protein (w/w) and incubated at 37 °C for 20 h. Digestion of NL1-691 (50 µg) with endoproteinase Glu-C was performed in a similar manner in 25 mM NH<sub>4</sub>HCO<sub>3</sub>, pH 8.0, buffer and 1:50 Glu-C/protein (w/w). Simultaneous digestion with protease and removal of N-linked oligosaccharides by PNGase F were carried out on an aliquot of NL1-691 (50 µg) using the same conditions as described, with the addition of 15 mU of PNGase F to the incubation mixture. Digests were stored at -20 °C and thawed as needed.

**CNBr Cleavage.** NL1-691 (50 µg) was cleaved with CNBr using the conditions 1.0 mg/mL protein in 70% TFA and a 500-fold molar excess of CNBr to Met residues in protein (nine Met residues, 0.322 mg of CNBr) and incubated at room temperature in the dark for 20 h. Immediately following incubation, the digest was spin vacuumed to dryness, resolubilized to 1.0 mg/mL protein in 100 mM NH<sub>4</sub>HCO<sub>3</sub>, pH 8.0, buffer, and stored at -20 °C. A sample of 20 µg of CNBr-cleaved NL1-691 was de-N-glycosylated by treatment with PNGase F using the conditions 1.0 mg/mL protein in 100 mM NH<sub>4</sub>HCO<sub>3</sub>, pH 8.0, and 6 mU PNGase F and incubated at 37 °C for 20 h. Digests were stored at -20 °C and thawed as needed.

**Reduction of Disulfide Bonds.** Proteolytic digests of NL1-691 were reduced by the addition of an aliquot of freshly prepared DTT (1.0 mg/mL solution), such that a 10-fold molar excess of DTT to cysteine residues was present. DTT-treated samples were incubated at 37 °C for 1 h prior to LC-MS.

**Differential Alkylation of Cys Residues.** NL1-691 (100 µg) was treated with IAA to carboxymethylate any free cysteine residues using the conditions 1.0 mg/mL protein in 50 mM NH<sub>4</sub>HCO<sub>3</sub>, pH 7.8, buffer and 50 mM IAA and incubated for 2 h. The samples were spin filtered to remove excess IAA, buffer exchanged to 6 M guanidine-HCl, pH 6.5, and incubated for 1 h. Disulfide linkages were reduced by treatment with 10 mM DTT for 1 h, after which the remaining cysteine residues were pyridylethylated by the

addition of 50 mM 4-VP and incubated for 2 h. All incubations were performed at 37 °C in the dark. The protein was spin filtered to remove the alkylating reagents, buffer exchanged with 50 mM NH<sub>4</sub>HCO<sub>3</sub>, pH 7.8, buffer, and lyophilized. Also, samples of NL1-691 were denatured by the addition of 6 M guanidine-HCl, pH 6.5, to the lyophilized protein and incubated for 1 h, prior to differential alkylation in a manner similar to that described above. Samples of alkylated NL1-691 were stored at -20 °C, until they were thawed for subsequent digestion with trypsin and PNGase F.

**O-Deglycosylation.** NL1-691 (100 µg) was treated with a cocktail of glycosidases for the removal of O-linked glycans using the conditions 1.0 mg/mL protein in 50 mM Na<sub>2</sub>HPO<sub>4</sub>, pH 5.5, buffer, 4 mU O-glycanase, 20 mU sialidase A, 12 mU β(1-4)-galactosidase, 160 mU β-N-acetylhexosaminidase, and 100 mU α-fucosidase and incubated for 5 d at 37 °C. The de-O-glycosylated protein was buffer exchanged to 50 mM NH<sub>4</sub>HCO<sub>3</sub>, pH 7.8, by spin filtration and lyophilized. Samples were stored at -20 °C, until they were thawed for subsequent digestion with proteases and de-N-glycosylation, in a manner similar to that described previously.

**Liquid Chromatography-Mass Spectrometry (LC-MS).** Proteolytic digests of NL1-691 were separated by reversed-phase fractionation on a Michrom Magic 2002 microbore HPLC instrument (Michrom BioResources, Inc., Auburn, CA). A 1.0 × 150 mm, 5 µM, 200A Magic C<sub>18</sub> column, operated at a flow rate of 50 µL/min and column temperature of 22 °C, was used. A standard gradient was employed for all LC-MS/MS runs of 2% A isocratic for 5 min, immediately followed by a 2–62% B gradient over 40 min. A is 2% (v/v) ACN and 0.05% (v/v) TFA, and B is 90% (v/v) ACN and 0.0475% (v/v) TFA. Typical injections were of 5–10 µg of digested protein. The eluant was run unsplit, directly into the electrospray mass spectrometer.

Mass spectra were recorded on an Applied Biosystems QSTAR, a hybrid quadrupole TOF mass spectrometer, equipped with the electrospray source (Applied Biosystems, Foster City, CA). Standard electrospray operating conditions were curtain gas 20, nebulizer gas (GS1) 80, and ion spray voltage (ISV) 5.20 kV. The instrument was set to scan mass (Da) to charge ratios of 400–2000 every 1.00071 s. The data were analyzed with the Analyst & BioAnalyst software packages (Applied Biosystems).

**Topology Modeling of Neuroligin.** A structural model of NL1 was generated with the programs Homology and InsightII (Accelrys, Inc., 2002) using the crystal structure of mouse AChE (1mah in the PDB database) as a template for the extracellular domain. For the modeling of the C-terminal ectodomain of NL1, the following templates were used: hydrolase (1blp), nitrogenase (2nip), binding protein (1ola), and citrate synthase (1csc). After homology modeling, the structure of NL1 was energy minimized for 10000 iterations using the distance-dependent dielectric constant with the program Discover (Accelrys, Inc., 2002).

## RESULTS

**Peptide Mapping.** Peptide mapping was performed on the 664 amino acid residue recombinant soluble rat NL1-691 using LC-MS/MS techniques. Digestion of the protein with trypsin, GluC, or CNBr was followed by injection of peptides

to a microbore HPLC system plumbed directly into a hybrid quadrupole TOF mass spectrometer, QSTAR. The resultant datasets were analyzed and the peptides assigned on the basis of mass. This was facilitated by the excellent mass accuracy of the QSTAR; typical errors for mass-based assignments were below 25 ppm. Trypsin, GluC, and CNBr digests were analyzed, in nonreduced and reduced conditions, to elucidate disulfide pairings and obtain lower mass peptides for the characterization of glycosylation sites. Aliquots of NL1-691 were de-N-glycosylated by treatment with PNGase F to characterize the occupancy of N-glycosylation sites. PNGase F hydrolyzes N-linked oligosaccharides from Asn side chains, converting the Asn to Asp, if N-glycan is present. PNGase F treated tryptic digests of NL1-691, in nonreduced, reduced, and differentially alkylated states, were analyzed by LC-MS/MS techniques to confirm peptide assignments based on mass. Additionally, NL1-691 was subjected to a cocktail containing O-glycanase and other glycosidases to effect de-O-glycosylation of the protein and to characterize the O-glycosylation sites.

Following this strategy, 97% of the amino acid sequence of NL1-691 was accounted for with assignment of the peptides from trypsin LC-MS/MS datasets (see the Supporting Information) and confirmed by GluC and CNBr LC-MS datasets. Three tryptic peptides were not resolved, spanning the contiguous sequence of K661–K679. The released amino acid K661 and tryptic peptide Q675–K679 are most likely too hydrophilic to be retained on the C18 column and eluted from HPLC separations in the void volume. The tryptic peptide N662–K674 contains a potential N-glycosylation site at Asn 662 and several sites that are predicted to be O-glycosylated by the algorithm NetOGlyc of Hansen and co-workers (12–14). The combination of N- and O-linked glycosylation most likely accounts for the absence of the peptide in resolved datasets.

**Disulfide Mapping.** The disulfide pairing of nine cysteine residues present in NL1-691 was determined by comparison of the nonreduced, reduced, and differentially alkylated trypsin + PNGase F digests and the nonreduced and reduced GluC + PNGase F digests. PNGase F was utilized to remove N-glycans attached to asparagine residues (Asn 109, Asn 343, Asn 547) close in sequence to three cysteine residues (Cys 117, Cys 342, Cys 546). This strategy simplified the disulfide assignment process by removing microheterogeneity introduced by N-glycans and decreased the mass of the peptides involved.

In trypsin + PNGase F digests, two interpeptide disulfides and two intrapeptide disulfides were clearly indicated by comparing the masses, fragment ions observed in MS/MS spectra, and shifts in retention time between the nonreduced and reduced datasets. Tryptic peptides D109–R125 and L126–K166 were linked in nonreduced conditions with an average mass of 6620.24 Da and separated upon reduction with monoisotopic masses of 1843.89 and 4774.35 Da, respectively. Note that the native Asn 109 was converted to Asp by PNGase F.

Similarly, tryptic peptides E171–R174 and K179–R182 were linked in the nonreduced datasets with a monoisotopic mass of 993.49 Da and separated upon reduction with a monoisotopic mass of 518.31 Da observed for K179–R182. Tryptic peptide E171–R174 was not observed in the reduced datasets, most likely due to its hydrophilicity and elution in

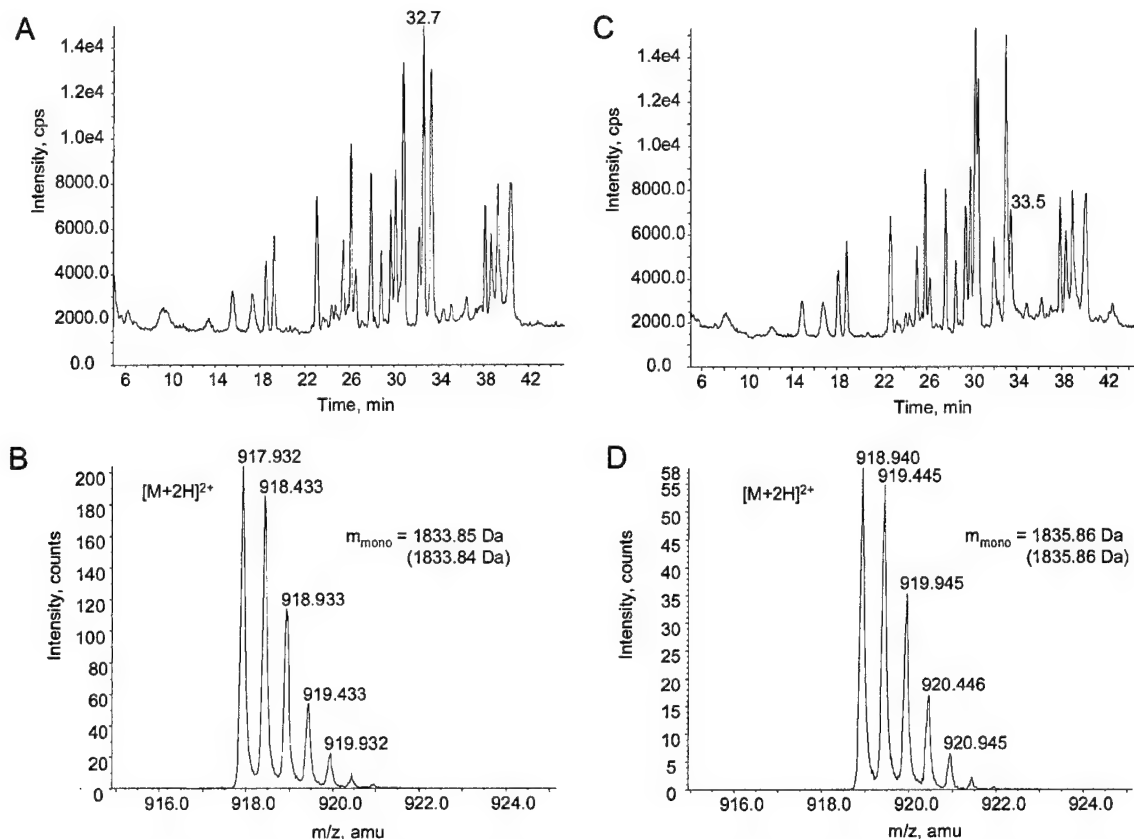


FIGURE 1: Disulfide linkage in the de-N-glycosylated peptide V340–K356. (A) LC–MS TIC chromatogram ( $m/z$  400–2000) for the nonreduced PNGase F treated trypsin digest of NL1-691. The elution position of disulfide-linked tryptic peptide V340–K356 is indicated at 32.7 min. (B) Mass spectrum ( $m/z$  915–925) of the disulfide-linked V340–K356 eluting at 32.7 min. The doubly charged ion gives a monoisotopic mass of 1833.85 Da. The predicted mass for the disulfide-linked peptide is shown in parentheses. (C) LC–MS TIC chromatogram ( $m/z$  400–2000) for the reduced PNGase F treated trypsin digest of NL1-691. The elution position of the reduced tryptic peptide V340–K356 is indicated at 33.5 min. (D) Mass spectrum ( $m/z$  915–925) of the reduced V340–K356 peptide eluting at 32.7 min. The doubly charged ion gives a monoisotopic mass of 1835.86 Da. The predicted mass for this reduced peptide is shown in parentheses. Note that the V340–K356 peptide is 0.98 Da heavier than the native sequence due to the conversion of N343 to D343 by PNGase F.

the HPLC void volume. However, the mass of 993.49 Da was only observed in nonreduced conditions, 518.31 Da was only observed following reduction, and acquired MS/MS spectra confirmed the peptide assignments.

Two intrapeptide disulfides were observed by an increase in mass of 2.01 Da (monoisotopic) between the nonreduced and reduced datasets and shifts in the retention times of affected peptides. Tryptic peptide V340–K356 changed from a monoisotopic mass of 1833.86 Da in nonreduced conditions to 1835.87 Da following reduction and shifted retention time by 0.8 min. Figure 1 presents data used to determine disulfide linkage between Cys 342 and Cys 353. MS/MS analyses for peptide V340–K356, before and after reduction, were consistent with an intrapeptide disulfide linkage (Figure 2). Tryptic peptide T475–K550 changed from an average mass of 8410.09 Da in nonreduced conditions to 8411.87 Da following reduction and shifted retention time by 0.4 min. A weak ionization signal precluded the observation of fragment ions in LC–MS/MS datasets for tryptic peptide T475–K550.

Thus, disulfide bonds present in NL1–691 are Cys 117–Cys 153, Cys 172–Cys 181, Cys 342–Cys 353, and Cys 512–Cys 546. The trypsin + PNGase F data are summarized in Table 1 for all cysteine-containing peptides. Additional support for the assignment of disulfides Cys 117–Cys 153 and Cys 512–Cys 546 was observed in trypsin datasets in

the form of incomplete digestion products. In the case of the former, D109–R125 and L126–R167 behaved similarly to D109–R125 and L126–K166, and in the case of the latter, T475–K568 behaved similarly to T475–K550. Moreover, independent confirmation of disulfides Cys 117–Cys 153, Cys 172–Cys 181, and Cys 512–Cys 546 came from analysis of the GluC + PNGase F nonreduced and reduced digests. The disulfide bonding Cys 512–Cys 546 was also confirmed by the analysis of CNBr + PNGaseF digests before and after reduction.

Tryptic peptide I275–R300 contains the single remaining cysteine residue (Cys 286) in the extracellular domain of NL1. This tryptic peptide is observed as a disulfide-bonded homodimer in the nonreduced LC–MS/MS datasets with a monoisotopic mass of 5274.56 Da and as a monomer with a monoisotopic mass of 2638.28 Da in reducing conditions. It is not surprising that a peptide containing an unpaired cysteine residue, once released from the structural context of the native protein, forms a covalent dimer in the nonreducing environment of the trypsin digest. To investigate further the native state of Cys 286, NL1-691 was subjected to differential alkylation. IAA was used to carboxymethylate free cysteines, and following denaturation and reduction of disulfide bonds, 4-VP was used to pyridylethylate the remaining cysteine residues. Carboxymethylation and pyridylethylation of cysteine residues results in an increase in

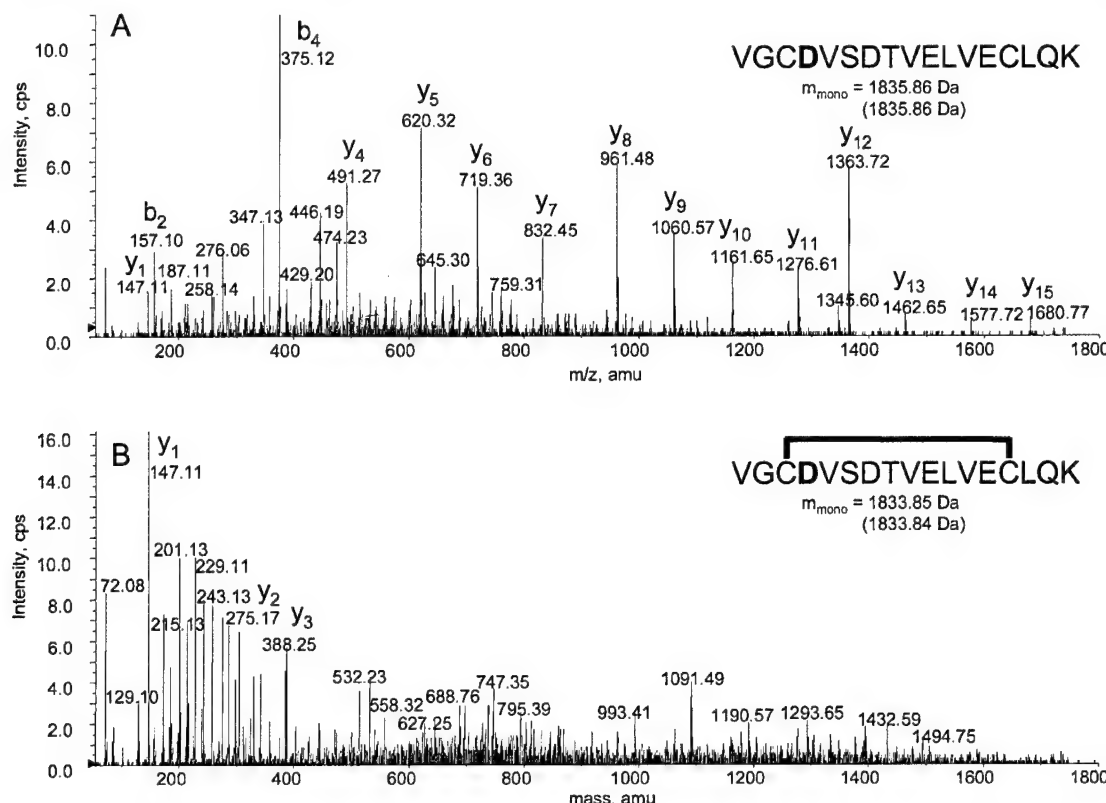


FIGURE 2: 2. MS/MS spectra ( $m/z$  55–1800) of the (A) reduced and (B) oxidized de-N-glycosylated peptide V340–K356. The identities of the b and y fragment ions are indicated above the fragment ion masses. The sequence of the peptide is shown along with the observed and predicted masses; the predicted masses are shown in parentheses. N343 is converted to D343 by PNGase F treatment. D343 is shown in bold text.

Table 1: Masses<sup>a</sup> and Elution Times Observed for Cys-Containing Peptides in Nonreduced and Reduced LC–MS Datasets of PNGase F Treated Tryptic Digests of NL1-691

disulfides	nonreduced elution time (min)	mass (Da)	reduced elution time (min)	mass (Da)	sequence
C117–C153	40.4	6620.24 (6620.39) <sup>b</sup>	30.3 42.6	1843.89 (1843.89) 4774.35 (4774.31)	<i>D</i> <sub>109</sub> ATQFAPVCPQNIIDGR <sub>125</sub> <sup>c</sup> L <sub>126</sub> PEVMLPVWFTNNLNDVSS YVQDQSEDCLYLN <sup>i</sup> YVPTED VK <sub>166</sub> E <sub>171</sub> CAR <sub>174</sub> K <sub>179</sub> ICR <sub>182</sub>
C172–C181	9.8	993.49 (993.48)	7.2	518.31 (518.30)	I <sub>275</sub> TVFGSGAGGSCVNLLTLS HYSEGNR <sub>300</sub>
C286 <sup>d</sup>	33.7	5274.56 (5274.55)	33.0	2638.28 (2638.28)	<i>V</i> <sub>340</sub> GCDVSDTVELVECLQK <sub>356</sub> T <sub>475</sub> LLALFTDHQWVAPAVAT ADLHSNFGSPTYFYAFYHHC QTDQVPAWADAAGDEVPI VLGIPMIGPTELFPCDFSK <sub>550</sub>
C342–C353 C512–C546	32.7 39.8	1833.86 (1833.85) 8410.09 (8410.35)	33.5 39.4	1835.87 (1835.86) 8411.87 (8412.37)	

<sup>a</sup> Monoisotopic masses recorded below 6000 Da, average masses above 6000 Da. <sup>b</sup> Calculated masses based on sequence are shown in parentheses following observed masses. <sup>c</sup> Cys residues are shown in bold type. Asn residues converted to Asp residues by PNGase F are shown in italics. <sup>d</sup> C286 is believed to be unpaired in monomeric NL1-691. However, a dimer of I275–R300 is observed in nonreduced LC–MS data.

monoisotopic mass of 58.01 and 105.06 Da, respectively. Tryptic peptide I275–R300 is resolved in the alkylated trypsin + PNGase F datasets with monoisotopic masses of 2696.29 and 2743.34 Da, corresponding to masses expected for carboxymethylated and pyridylethylated peptides, respectively. The identification of the alkylated I275–R300 peptides was confirmed by MS/MS analysis. The abundances of the alkylated forms, as determined by ion peak areas, indicated Cys 286 was 82.6% carboxymethylated and 17.4% pyridylethylated. The extent of Cys 286 carboxymethylation

indicates that the majority of this residue is free in native NL1-691 and suggests that it does not form stable disulfide-linked homodimers of the NLs. The incomplete carboxymethylation observed for Cys 286 may be due to poor accessibility, whereby IAA encounters steric hindrance that limits its ability to interact with this residue in native NL1-691. The denaturation of NL1-691 prior to the sequential treatment with IAA, DTT, and 4-VP results in exclusive pyridylethylation of Cys 286. In addition, denaturation of NL1-691 in the presence of IAA, followed by reduction and

pyridylethylation, results in 11.5% carboxymethyl-Cys 286 and 88.5% pyridylethyl-Cys 286. Taken together, these data suggest that Cys 286 exhibits great propensity to disulfide bond when released from the structural context of the protein. Note that all other Cys-containing tryptic peptides of NL1-691 were observed only as the pyridylethylated form, providing further confirmation of the disulfide linkages as assigned.

**N-Glycosylation.** NL1-691 contains six potential N-glycosylation sites in the form of N-glycosylation sequons: N(–6)SS, N109AT, N303ST, N343VS, N547FS, and N662ST. Comparison of LC–MS datasets for the reduced trypsin and the reduced trypsin + PNGase F digests indicates the first five potential N-glycosylation sites listed above are all N-glycosylated. Note that the estimates of occupancy are based on the assumption that nonglycosylated and de-N-glycosylated peptides ionize with an equal efficiency. Estimates of N-glycan structure predominance are based on the assumption that all N-glycopeptide forms at a given site ionize with equal efficiency. Since these assumptions may not be strictly true, the numbers should be viewed as best estimates. Oligosaccharide content, as determined by mass-matching paradigms, is used to propose structures that would be consistent with typical complex glycans commonly observed for mammalian expression systems (see the Supporting Information). These types of analyses have been shown to be fairly accurate when compared with more quantitative carbohydrate analyses (15). Each N-glycosylation site will be considered separately below.

**Asn–6.** This N-glycosylation site is not native to NL1, as it was introduced as part of an 18-residue FLAG peptide and linker region at the N-terminus of the recombinant construct. Occupancy of N-glycosylation site Asn –6 was estimated to be 98% on the basis of a comparison of the ( $M + 2H$ )<sup>2+</sup> ion peak areas of nonglycosylated tryptic peptide D(–18)K47 and de-N-glycosylated peptide in the reduced trypsin + PNGase F datasets. These two peptides differed in mass by 0.98 Da, and nonglycosylated peptide eluted 0.6 min before the de-N-glycosylated form. The N-glycopeptide D(–18)K47 elutes as a broad heterogeneous peak centered about 24.5 min, and the de-N-glycosylated peptide elutes as a single sharp peak at 25.9 min. Analysis of the masses associated with tryptic N-glycopeptide D(–18)K47 suggest glycans that are mainly consistent with sialylated core fucosylated complex type N-glycans of biantennary to tetraantennary type, with biantennary predominating at this site. Glycan masses are observed that would be consistent with several further modifications of antennae, including GalNAc for Gal substitution, typically found at the end of nonsialylated antennae, fucosylation, and sulfation.

**Asn 109.** Occupancy of N-glycosylation site Asn 109 was estimated to be 100%, as no nonglycosylated tryptic peptide N109–R125 was observed in the reduced trypsin datasets. N-Glycopeptide N109–R125 elutes as a broad heterogeneous peak centered about 29.3 min, and the de-N-glycosylated peptide elutes as a single sharp peak at 30.3 min. Analysis of glycan masses associated with tryptic N-glycopeptide N109–R125 suggests they are mainly consistent with sialylated core fucosylated complex type N-glycans of biantennary to tetraantennary type, with biantennary predominating at this site. We find masses that indicate a number of modifications of antennae, including GalNAc for Gal

substitution, fucosylation, and sulfation. Further, masses that can be attributed to an additional GlcNAc are observed for some N-glycans, consistent with a  $\beta$ 1,4-GlcNAc attached to terminal mannose of the core.

**Asn 303.** Occupancy of N-glycosylation site Asn 303 was estimated to be 100%, as no nonglycosylated tryptic peptide W301–K306 was observed in the reduced trypsin datasets. N-Glycopeptide W301–K306 elutes as a broad heterogeneous peak centered about 7.9 min, and the de-N-glycosylated peptide was not observed in the reduced trypsin + PNGase F datasets. Analysis of the masses associated with the weakly ionizing tryptic N-glycopeptide W301–K306 suggests glycans that are mainly consistent with sialylated core fucosylated complex type N-glycans of tetraantennary type. We find no mass-based evidence for further modifications of antennae at this site.

**Asn 343.** Occupancy of N-glycosylation site Asn 343 was estimated to be 100% as no nonglycosylated tryptic peptide V340–K356 was observed in the reduced trypsin datasets. N-Glycopeptide V340–K356 elutes as a broad heterogeneous peak centered about 32.2 min, and the de-N-glycosylated peptide elutes as a single sharp peak at 33.5 min. Figure 3 shows the mass spectrum of the heterogeneous N-glycopeptide V340–K356, indicating the doubly and triply charged ions and the reconstructed mass spectrum showing the N-glycopeptide masses derived from the raw mass spectrum. Analysis of glycan masses associated with tryptic N-glycopeptide V340–K356 suggests they are mainly consistent with sialylated core fucosylated complex type N-glycans of biantennary to tetraantennary type, with biantennary predominating at this site. Additional modifications of antennae are suggested, by observed masses that would be consistent with GalNAc for Gal substitution, fucosylation, and sulfation. The mass for an additional GlcNAc was observed for some glycan structures.

**Asn 547.** Occupancy of N-glycosylation site Asn 547 was estimated to be 100%, as no nonglycosylated tryptic peptide T475–K550 was observed in the reduced trypsin datasets. Although the N-glycosylated form of the peptide containing Asn 547 was not observed in the reduced trypsin LC–MS data, the de-N-glycosylated peptide T475-K550 elutes as a single peak at 39.4 min in the reduced trypsin + PNGase F datasets. The de-N-glycosylated peptide has a mass of over 8000 Da and weakly ionizes; it is therefore not surprising that the more massive and heterogeneous N-glycopeptide does not resolve. However, this precludes characterization of the type of N-glycans associated with Asn 547 by mass analysis.

**Asn 662.** The tryptic peptide containing Asn 662 (N662–K674) was not observed in any of the trypsin or GluC datasets. Treatment with both PNGase F and a glycosidase cocktail for de-O-glycosylation failed to produce a mass that could be attributed to deglycosylated peptide N662–K674 or incomplete cleavage products containing this peptide. The absence of the parent mass for this peptide in both the trypsin + PNGase F digested NL1-691 and the trypsin + PNGase F digested de-O-glycosylated NL1-691 suggests that both N- and O-glycosylations are occurring on this peptide. This may render the peptide partially resistant to enzymatic deglycosylation and/or confer sufficient heterogeneity that it elutes over an extended time with a poor ionization signal.

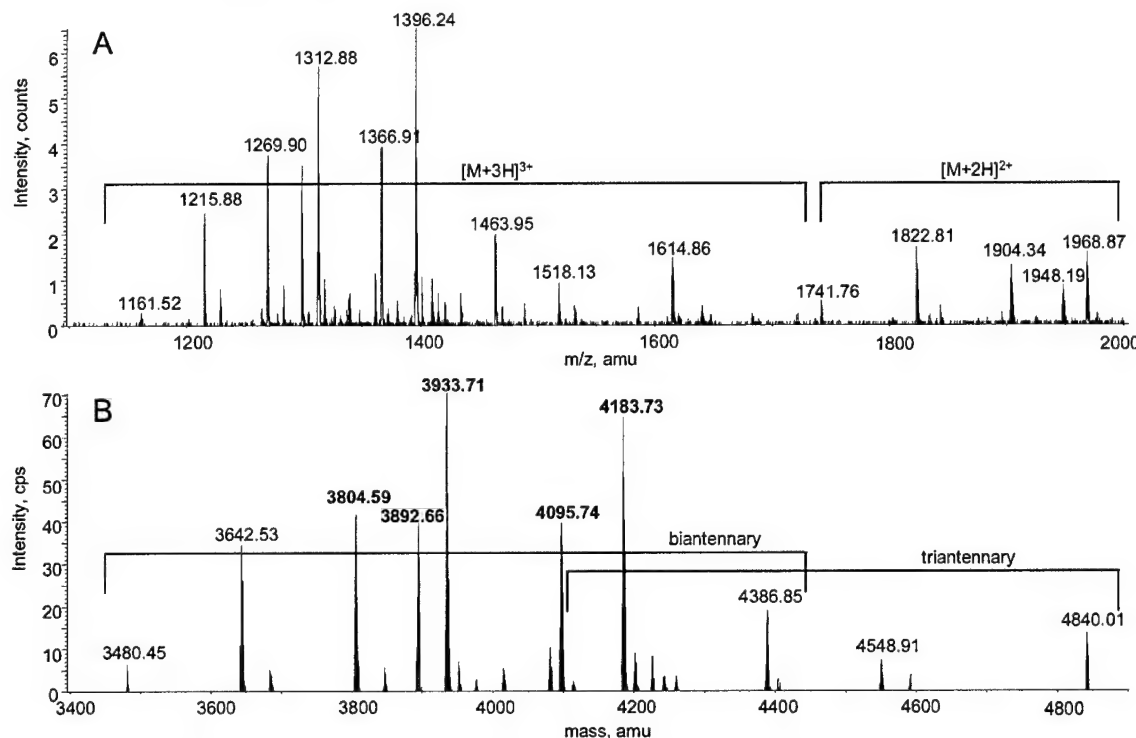


**FIGURE 3:** *N*-Glycopeptide V340–K356. (A) Summed mass spectrum ( $m/z$  1100–2000, 31.4–31.9 min) from the LC–MS dataset of the nonreduced trypsin digest of NL1-691. The ranges of doubly and triply charged ions of the heterogeneous tryptic *N*-glycopeptide V340–K356 are indicated by bars. (B) Reconstructed mass spectrum from 3400 to 4900 AMU of the mass spectrum shown in panel A. Monoisotopic masses are shown above a representative set of peaks, and mass ranges of biantennary and triantennary complex *N*-glycans are indicated by bars. The five most prevalent masses of *N*-glycopeptide V340–K356 are indicated in bold text.

**O-Glycosylation.** We find masses for tryptic peptide Q680–R690 that would be consistent with O-glycosylation by mucin-type O-glycans, likely typical mono- and disialylated Gal $\beta$ 1–3GalNAc $\alpha$ 1-S/T glycosylation. Figure 4 shows the total ion current (TIC) chromatogram for the nonreduced trypsin dataset as well as the extracted ion currents (XICs) for doubly charged ions of Q680–R690 in various O-glycosylation states. On the basis of doubly charged ion intensities, it is estimated that the O-glycan occupancy of this peptide is about 21%. Of the O-glycosylated peptide, approximately 85% resolves as masses that can be attributed to a single mucin-type O-glycan and 15% to two mucin-type O-glycans. There are only two possible O-glycosylation sites present in this peptide, indicating Ser 683 and Ser 686 are O-glycosylated in NL1-691.

Indirect evidence suggests O-glycosylation to occur in tryptic peptides V623–K648 and V649–R660. These two tryptic peptides were observed only in the trypsin digests of enzymatically de-O-glycosylated NL1-691. Upon de-O-glycosylation, two new masses appear in the trypsin datasets, 3035.56 Da at 30.6 min and 1354.75 Da at 15.6 min, corresponding to masses expected for V623–K648 and V649–R660, respectively. The mucin-type O-glycosylation prediction algorithm (12–14) predicts four O-glycosylation sites in these two tryptic peptides, Ser 644, Thr 647, Thr 652, and Thr 659. This does not preclude the possibility that O-glycans other than the mucin type are attached to the two O-glycopeptides. Four mucin-type O-glycosylation sites are also predicted in tryptic peptide N662–K674. The predicted sites are Thr 664, Thr 667, Ser 668, and Thr 672. Note that

no other O-glycosylation sites are predicted N-terminal to residue Val 623.

## DISCUSSION

Greater than 97% of the NL1-691 amino acid sequence has been accounted for and characterized by LC–MS and LC–MS/MS analysis. N-glycosylation has been confirmed at five of the six possible sites, and the *N*-glycan content has been characterized at four of the observed sites. The masses of *N*-glycans are typical of those observed in other recombinant proteins expressed in mammalian cell lines, sialylated core fucosylated complex *N*-glycans with variable antennae numbers and structures. O-glycosylation has been confirmed at two C-terminal serine residues, and other likely O-glycosylation sites have been predicted (12–14). A graphical summary of peptide, disulfide, and glycosylation data is presented in Figure 5.

Given the homology of the extracellular domain of NLs to  $\alpha/\beta$  hydrolase fold proteins, the pattern of cysteine connectivity and sites of oligosaccharide attachment of NL1 provide a foundation to deduce the tertiary structure of NLs. Moreover, the experimental evidence acquired here supports refining of a structural model for NL (Figure 6) constructed by predictions based mainly on homology to AChE.

The truncation of rat NL1 prior to the transmembrane segment produces a soluble protein comprising the entire ectodomain. Recombinant soluble rat NL1-691 can be purified to homogeneity, by use of an epitope tag, facilitating detailed biophysical analysis by peptide mapping and mass spectrometric strategies. It is not known whether the glycosyl

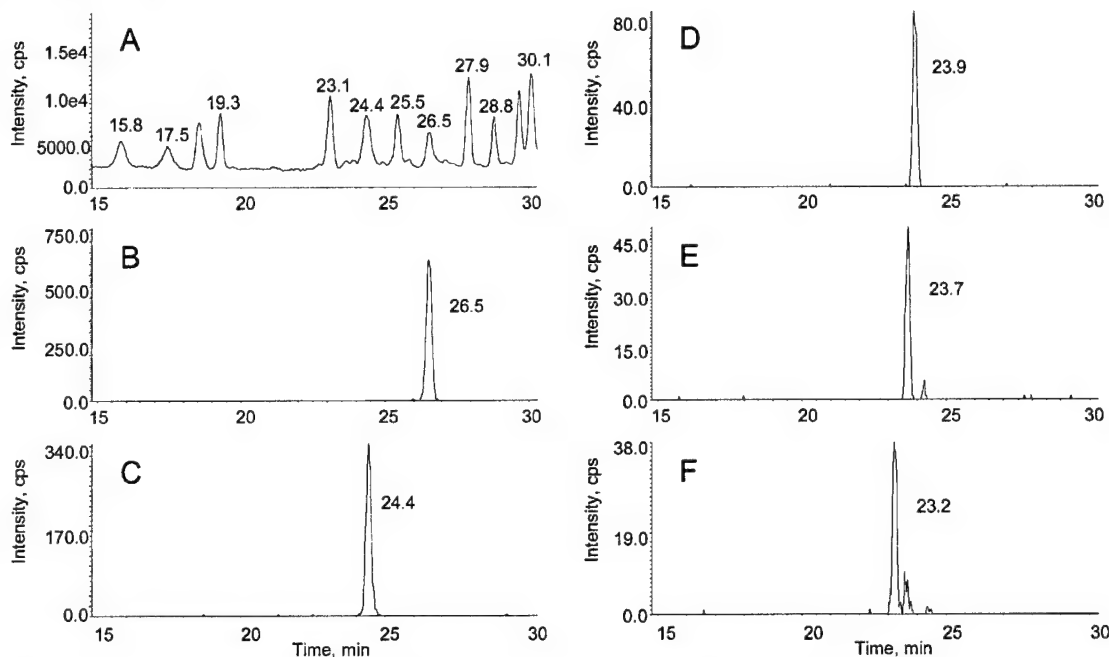


**FIGURE 4:** O-glycopeptide Q680–R690. (A) LC–MS TIC chromatogram ( $m/z$  400–2000) for the nonreduced trypsin digest of NL1-691 from 15 to 30 min. (B) XIC of  $m/z$  636.1–636.5 from the chromatogram in panel A showing the elution position of the doubly charged ion of nonglycosylated peptide Q680–R690. Note that the mass of this tryptic peptide is 17.03 Da lower than that expected from the native sequence due to conversion of the N-terminal residue Q680 to a pyroglutamic acid, as confirmed by MS/MS analysis. (C) XIC of  $m/z$  964.4–964.8 from the chromatogram in panel A showing the elution position of the doubly charged ion of Q680–R690 + monosialylated HexNAcHex. (D) XIC of  $m/z$  1110.0–1110.4 from the chromatogram in panel A showing the elution position of the doubly charged ion of Q680–R690 + disialylated HexNAcHex. (E) XIC of  $m/z$  1147.1–1147.5 from the chromatogram in panel A showing the elution position of the doubly charged ion of Q680–R690 + monosialylated (HexNAcHex)<sub>2</sub>. (F) XIC of  $m/z$  1292.7–1293.1 from the chromatogram in panel A showing the elution position of the doubly charged ion of Q680–R690 + disialylated (HexNAcHex)<sub>2</sub>. Note that the scale of the y-axis (intensity, cps) is variable.

content resulting from production of recombinant NL1-691 in HEK293 cells is similar to those of NLs of neurons in the central nervous system. However, NLs produced by heterologous expression in HEK293 cells have been shown to interact with  $\beta$ -NXs (16) and to induce synapse formation in cocultured neurons (6, 7, 17). Such functionality indicates that the recombinant protein is properly folded and post-translationally processed in a manner similar to that of native NL.

Proteolytic digests of NL1 generated by treatment with trypsin, Glu-C, and CNBr were resolved to obtain an overlapping, comprehensive coverage of NL1 peptides. The amino acid sequence of recombinant NL1 was confirmed to be the expected primary translation product encoded by the cDNA sequence; cleavage of the signal peptide was confirmed, and no modifications of amino acids were evident. Peptides of NL1 generated by specific proteolysis were resolved in native and reduced conditions. Analysis of peptides by mass-matching paradigms and fragment ion data from MS/MS spectra elucidated the disulfide bridging pattern of the nine cysteines in the NL1 ectodomain. Eight cysteines are disulfide bonded, and one, Cys 286, is likely present as a free cysteine. Cys 286 does not appear to participate in intermolecular disulfide bonding between NL dimers, since a majority of this residue is converted to carboxymethylcysteine on treatment with alkylating reagent. Two disulfide bonds, Cys 117 to Cys 153 and Cys 342 to Cys 353, are highly conserved among the family of hydrolase proteins ( $\alpha/\beta$  hydrolase protein database: <http://bioweb.ensam.inra.fr/>

ESTHER/general?what=index). The disulfide linkage of Cys 117 to Cys 153 in NL1 is homologous to an  $\omega$  loop in AChE, shown to undergo distinctive conformational fluctuations that are coupled to enzyme activity (18). While NLs lack hydrolase activity, it is tempting to speculate the homologous loop domain may undergo conformational changes that affect functional properties. Disulfide bonding of Cys 172 to Cys 181, presumably forming an exposed surface loop, is encoded within an alternatively spliced exon. This region has been identified in NL1 and NL2 isoforms of rat brain (2) and may be involved in adhesion or recognition events. The cysteine pair in the C-terminal region of the NL ectodomain, distinct from the majority of hydrolases in the family, is also shown to disulfide bond. It is this region which likely possesses a tertiary structure unique to the NL members. The overall cysteine pattern in the nonspliced region is highly conserved among the NLs, suggesting these three disulfide-bonded loops in the invariant regions are essential for defining the structural motif.

NL1 peptides containing N-glycosylation sequons have been mapped, in native conditions and following de-N-glycosylation, to demonstrate carbohydrate occupancy at Asn 109, Asn 303, Asn 343, and Asn 547. An additional N-glycosyl attachment site occurs in the linker peptide between the epitope tag and NL1 in the recombinant construct (Asn -6) and is occupied. N-glycosylation at Asn 662 could not be confirmed, since the peptide containing the sequon was not observed in proteolytic digests of NL1, native or deglycosylated. It is likely that both N- and

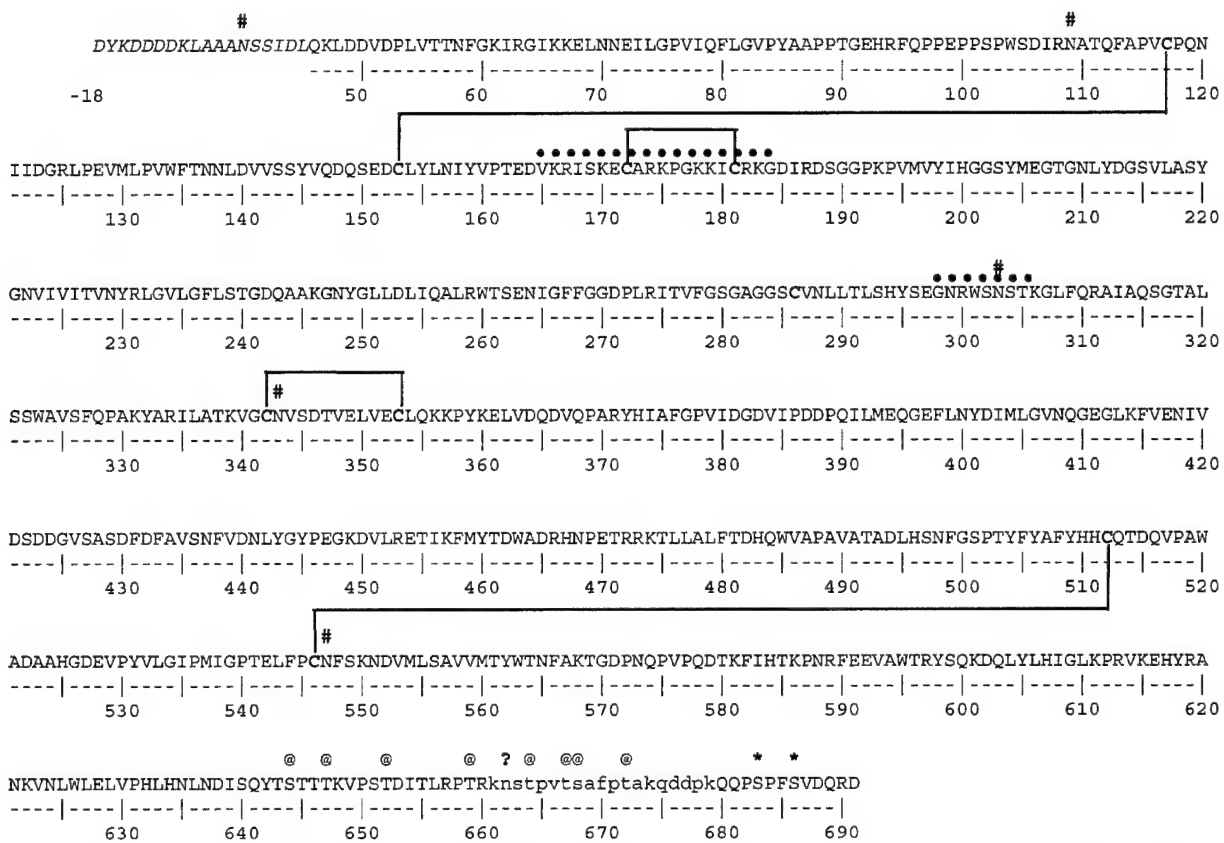


**FIGURE 5:** Peptide, disulfide, and glycosylation map of NL1-691. The sequence of rat NL1-691 expressed from Q46–D691 is shown, including the N-terminal FLAG and linker peptide designated as residues –18 to –1 and contiguous with Q46; the FLAG peptide grafted onto NL1-691 sequence is shown in italics. The alternatively spliced regions of the NLs (V165–G184 and G298–T305) are denoted by a dotted line. The region from K661 to K679, shown in small letters, was not observed. Cysteine residues are shown in bold text, and disulfide bridges are shown by connecting lines. The experimentally characterized glycosylation sites are marked by asterisks (O-glycosylation) and by pound signs (N-glycosylation). The single potential N-glycosylation site in the unresolved region is indicated by a question mark. Possible O-glycosylation sites, as predicted by the mucin-type O-glycosylation algorithm of Hansen and co-workers (12–14), are marked by ampersands.

O-linked glycosylations on the peptides comprising this region lead to inferior resolving capabilities by LC-MS methods (discussed further below).

An analysis of the carbohydrate content at the first four N-glycosylation sites has been performed by mass-matching paradigms. A significant microheterogeneous population of glycosyl residues is identified. The major species suggested by the observed masses are consistent with trimannosyl core complex carbohydrates, core fucosylated, bi-, tri- and tetraantennary structures, that can be sialylated, sulfated, and/or capped by neutral *N*-acetylhexosamine. The most abundant species, as determined by ion intensity in resolved mass spectra, were consistent with highly branched, core fucosylated and sialylated carbohydrates.

The occupancy of N-linked glycosylation sequons leads us to conclude that these domains are surface exposed and facilitates the prediction of tertiary protein structure from the amino acid sequence. Moreover, N-linked glycosylation may play an important functional role. Studies on binding interactions of NLs with  $\beta$ -NXs, by surface plasmon resonance techniques, have shown glycosylation processing of NL to inhibit this interaction (16). Interestingly, N-glycosylation at Asn 303 occurs in a region alternatively spliced among NL isoforms and may represent a mechanism for modulating NL and NX interactions. In previous studies, large N-linked oligosaccharides have been shown to influence

the recognition of protein–protein interactions and to down modulate the activity of enzymes and signaling molecules (19, 20).

O-glycosylation in the segment of the NL1 ectodomain that links the hydrolase homology and transmembrane-spanning regions was confirmed by the direct observation of masses that are consistent with mucin-like sugars on the peptides containing Ser 683 and Ser 686. The prediction of O-linked glycosylation by the NetOGlyc algorithm (12–14) indicates Ser 644, Thr 647, Thr 652, Thr 659, Thr 664, Thr 667, Ser 668, and Thr 672 have a high probability for modification. Interestingly, Ser 683 and Ser 686, directly observed to carry O-linked mucin-type sugars, were predicted to have low probability of occupancy. O-linked carbohydrates in the region spanning Ile 639 to Arg 660 were inferred by the ability to observe the peptides only after deglycosylation by a cocktail of glycohydrolases specific for O-linked oligosaccharides. It was not possible to resolve O-glycosylated peptides within this region. Additionally, the peptide from Asn 662 to Lys 674, also containing an *N*-glycosyl sequon, was not detectable. A high content of oligosaccharides would contribute to inadequate separation by reversed-phase chromatography and/or peptides with poor ionization potential for detection by mass spectrometry. Further, we presume that a high carbohydrate content may interfere, by steric hindrance, with the exposure of appropriate bonds to

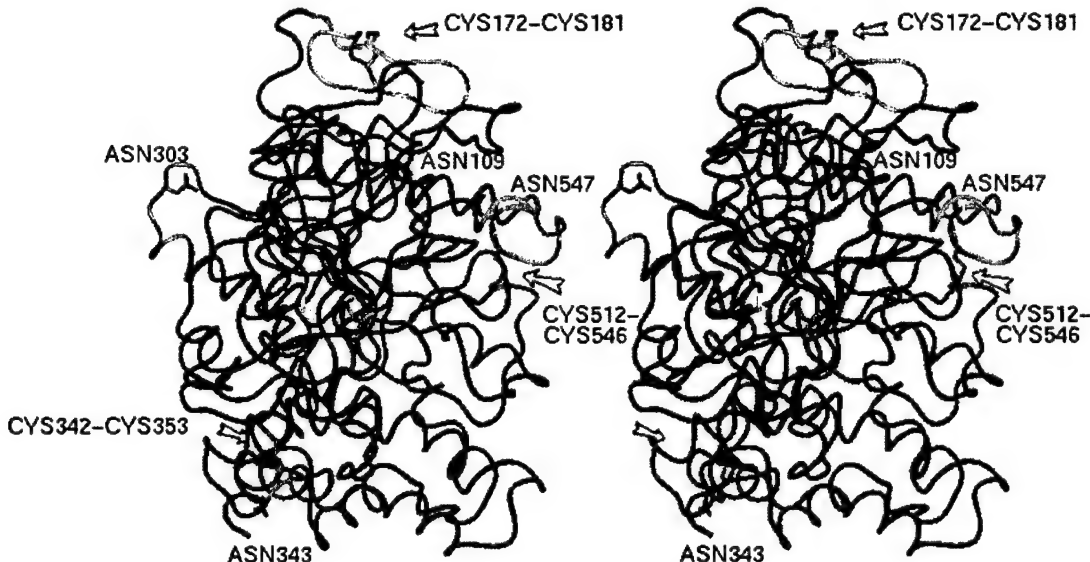


FIGURE 6: Topology model of NL1 from amino acids Q46–S640, generated with the programs Homology, InsightII, and Discover (Accelrys, Inc., 2002) shown as a stereo image. Disulfide linkages are indicated in green. In the center of the molecule, the unlabeled yellow residue on the left is Cys 286 and the disulfide bridge between Cys 117 and Cys 153 is to its right. N-linked glycosylation sites are indicated in red. Alternatively spliced regions of NL1 are colored orange. The region where the novel structure is proposed to account for disulfide linkage of Cys 512 to Cys 546 is indicated in cyan.

the glycosidase active site, thereby preventing deglycosylation.

O-glycosylation in protein domains with high Ser/Thr/Pro content and limited N-linked carbohydrates, such as that found in the NL1 linker region, causes significant perturbations in secondary protein structure and has a striking influence on tertiary conformations (21). The high number of oligosaccharides on Ser and Thr, combined with an abundance of Pro residues, creates a bottlebrush-like structure. Multiple interactions of GalNAc at Ser/Thr residues and the peptide backbone lead to an elongation of the peptide chain, as demonstrated in the P-selectin molecule (22). For the neurotrophin receptor, an O-glycosylation cassette that is heavily sialylated in a stalk-like region, similar to NLs, helps to orient the ligand binding domain away from the cell surface and is possibly involved in intercellular signaling (23). Further, O-glycosylation cassettes can function in conferring protein stability and protease resistance. Of particular interest is that O-glycans have been shown to influence the aggregation of proteins and their quaternary structure, as for lactase phlorizin hydrolase (24). A recent study demonstrated that oligomerization of NL is required for functional activity (7). Perhaps O-linked sugars serve to modulate NL and NX associations.

A topology model predicting the tertiary structure of the NL1 ectodomain (Figure 6) has been refined to incorporate the disulfide bonding pattern and position of extrafacial domains, inferred from carbohydrate attachment sites. The unequivocal disulfide connectivity between Cys 512 and Cys 546 indicates NL1 topology must deviate from predictions based solely on AChE homology. This is not surprising, since significant sequence divergence from AChE occurs in the C-terminal portion of the esterase-like domain of NLs. Therefore, a substantial difference in tertiary structure in this region of the NL1 ectodomain is proposed to place the cysteine pair in close proximity to support disulfide bonding.

Mutations of X-linked genes encoding NLs have been found to be associated with autistic disorders and Asperger syndrome (25). The ability of NL1 to induce synapse formation requires the specific interaction of NL1 with  $\beta$ -NXs and a homooligomerization of NL1, involving extracellular protein domains that are discrete from the NL and NX binding interface (7). Defining the molecular topology of the extracellular region of NL1 and posttranslational modifications, such as N- and O-glycosylation, is an important advance toward efforts to elucidate structure–activity relationships essential for NL-induced synaptic organization in the central nervous system.

#### ACKNOWLEDGMENT

We thank Dr. Elizabeth Komives for expert advice on mass spectrometric analyses.

#### SUPPORTING INFORMATION AVAILABLE

Tables S1 and S2 describing LC–MS/MS datasets for trypsin + PNGaseF treated NL1-691, in nonreduced and reduced conditions, Tables S3–S5 describing the heterogeneous N-linked glycosyl species observed at Asn 109, Asn 303, and Asn 343 of NL1-691, as predicted by the average mass (Da) of oligosaccharide chains, and Table S6 describing the O-linked glycosyl structures of the mucin type found at Ser 683 and Ser 686 in NL1-691. This material is available free of charge via the Internet at <http://pubs.acs.org>.

#### REFERENCES

1. Ichtchenko, K., Hata, Y., Nguyen, T., Ullrich, B., Missler, M., Moomaw, C., and Sudhof, T. C. (1995) Neuroligin 1: a splice site-specific ligand for beta-neurexins, *Cell* 81, 435–443.
2. Ichtchenko, K., Nguyen, T., and Sudhof, T. C. (1996) Structures, alternative splicing, and neurexin binding of multiple neuroligins, *J. Biol. Chem.* 271, 2676–2682.
3. Bolliger, M. F., Frei, K., Winterhalter, K. H., and Gloor, S. M. (2001) Identification of a novel neuroligin in humans which binds to PSD-95 and has a widespread expression, *Biochem. J.* 356, 581–588.

4. Nguyen, T., and Sudhof, T. C. (1997) Binding properties of neuroligin 1 and neurexin 1beta reveal function as heterophilic cell adhesion molecules, *J. Biol. Chem.* 272, 26032–26039.
5. Song, J. Y., Ichtchenko, K., Sudhof, T. C., and Brose, N. (1999) Neuroligin 1 is a postsynaptic cell-adhesion molecule of excitatory synapses, *Proc. Natl. Acad. Sci. U.S.A.* 96, 1100–1105.
6. Scheiffele, P., Fan, J., Choih, J., Fetter, R., and Serafini, T. (2000) Neuroligin expressed in nonneuronal cells triggers presynaptic development in contacting axons, *Cell* 101, 657–669.
7. Dean, C., Scholl, F. G., Choih, J., DeMaria, S., Berger, J., Isacoff, E., and Scheiffele, P. (2003) Neurexin mediates the assembly of presynaptic terminals, *Nat. Neurosci.* 6, 708–716.
8. Holmquist, M. (2000) Alpha/Beta-hydrolase fold enzymes: structures, functions and mechanisms, *Curr. Protein Pept. Sci.* 1, 209–235.
9. Sussman, J. L., Harel, M., Frolov, F., Oefner, C., Goldman, A., Toker, L., and Silman, I. (1991) Atomic structure of acetylcholinesterase from *Torpedo californica*: a prototypic acetylcholine-binding protein, *Science* 253, 872–879.
10. Marchot, P., Ravelli, R. B., Raves, M. L., Bourne, Y., Vellom, D. C., Kanter, J., Camp, S., Sussman, J. L., and Taylor, P. (1996) Soluble monomeric acetylcholinesterase from mouse: expression, purification, and crystallization in complex with fasciculin, *Protein Sci.* 5, 672–679.
11. Bradford, M. M. (1976) A rapid and sensitive method for the quantitation of microgram quantities of protein utilizing the principle of protein-dye binding, *Anal. Biochem.* 72, 248–254.
12. Hansen, J. E., Lund, O., Engelbrecht, J., Bohr, H., and Nielsen, J. O. (1995) Prediction of O-glycosylation of mammalian proteins: specificity patterns of UDP-GalNAc:polypeptide N-acetylgalactosaminyltransferase, *Biochem. J.* 308(Part 3), 801–813.
13. Hansen, J. E., Lund, O., Tolstrup, N., Gooley, A. A., Williams, K. L., and Brunak, S. (1998) NetOglyc: prediction of mucin type O-glycosylation sites based on sequence context and surface accessibility, *Glycoconjugate J.* 15, 115–130.
14. Hansen, J. E., Lund, O., Nilsson, J., Rapacki, K., and Brunak, S. (1998) O-GLYCBASE Version 3.0: a revised database of O-glycosylated proteins, *Nucleic Acids Res.* 26, 387–389.
15. Hoffman, R. C., Andersen, H., Walker, K., Krakover, J. D., Patel, S., Stamm, M. R., and Osborn, S. G. (1996) Peptide, disulfide, and glycosylation mapping of recombinant human thrombopoietin from Ser1 to Arg246, *Biochemistry* 35, 14849–14861.
16. Comoletti, D., Flynn, R., Jennings, L. L., Chubykin, A., Matsumura, T., Hasegawa, H., Sudhof, T. C., and Taylor, P. (2003) Characterization of the interaction of a recombinant soluble neuroligin-1 with neurexin-1-beta, *J. Biol. Chem.* 90, 3950–3957.
17. Fu, Z., Washbourne, P., Ortinski, P. I., and Vicini, S. (2003) Functional excitatory synapses in HEK293 cells expressing neuroligin and glutamate receptors, *J. Neurophysiol.* (in press).
18. Shi, J., Tai, K., McCammon, J. A., Taylor, P., and Johnson, D. A. (2003) Nanosecond dynamics of the mouse acetylcholinesterase Cys69–Cys96 omega loop, *J. Biol. Chem.* 278, 30905–30911.
19. Opdenakker, G., Rudd, P. M., Ponting, C. P., and Dwek, R. A. (1993) Concepts and principles of glycoproteins, *FASEB J.* 7, 1330–1337.
20. Shen, L., and Kane, K. P. (1995) Differential ability of isolated H-2 Kb subsets to serve as TCR ligands for allo-specific CTL clones: potential role for N-linked glycosylation, *J. Exp. Med.* 181, 1773–1783.
21. Van den Steen, P., Rudd, P. M., Dwek, R. A., and Opdenakker, G. (1998) Concepts and principles of O-linked glycosylation, *Crit. Rev. Biochem. Mol. Biol.* 33, 151–208.
22. Li, F., Erickson, H. P., James, J. A., Moore, K. L., Cummings, R. D., and McEver, R. P. (1996) Visualization of P-selectin glycoprotein ligand-1 as a highly extended molecule and mapping of protein epitopes for monoclonal antibodies, *J. Biol. Chem.* 271, 6342–6348.
23. Chapman, B. S., Eckart, M. R., Kaufman, S. E., and Lapointe, G. R. (1996) O-linked oligosaccharide on the 75-kDa neurotrophin receptor, *J. Neurochem.* 66, 1707–1716.
24. Naim, H. Y., and Lentze, M. J. (1992) Impact of O-glycosylation on the function of human intestinal lactase-phlorizin hydrolase. Characterization of glycoforms varying in enzyme activity and localization of O-glycoside addition, *J. Biol. Chem.* 267, 25494–25504.
25. Jamain, S., Quach, H., Betancur, C., Rastam, M., Colineaux, C., Gillberg, I. C., Soderstrom, H., Giros, B., Leboyer, M., Gillberg, C., Bourgeron, T., Nyden, A., Philippe, A., Cohen, D., Chabane, N., Mouren-Simeoni, M. C., Brice, A., Sponheim, E., Spurkland, I., Skjeldahl, O. H., Coleman, M., Pearl, P. L., Cohen, I. L., Tsioris, J., Zappella, M., Menchetti, G., Pompella, A., Aschauer, H., and Van Maldergem, L. (2003) Mutations of the X-linked genes encoding neuroligins NLGN3 and NLGN4 are associated with autism, *Nat. Genet.* 34, 27–29.

BI035278T

## Knockout Mice with Deletions of Alternatively Spliced Exons of Acetylcholinesterase

Shelley Camp, Limin Zhang, Michael Marquez, Brian de la Torre and Palmer Taylor

*Department of Pharmacology 0636, University of California at San Diego, La Jolla, California 92093*

Alternative splicing at the 3' end of the acetylcholinesterase (*Ache*) gene produces three different C-terminal sequences that are associated with a constant catalytic domain (1). Splicing to exon 5 produces glycophospholipid linked AChE<sub>H</sub>. Splicing to exon 6 results in the AChE<sub>T</sub> form capable of forming monomers, dimers and tetramers of these AChE subunits as well as associating with anchoring proteins ColQ and PRiMA (2-4). Reading through the 3' end of exon 4 produces AChE<sub>R</sub>, soluble AChE monomers. Although a vast body of information about the three alternative 3' end sequences exists, assessing the role of each form in tissue as well as during development has proved to be a complex task. In this light we have approached the problem using knockout mice. As Lockridge and colleagues have shown with the total AChE knockout, life in mammals without AChE is possible, yet the knockout mice do not thrive (5). We have produced two knockouts, one deleting exon 5, and the other deleting both exons 5 and 6, and a third colony deleting only exon 6 is being bred. In both knockouts the sequence that would produce the AChE<sub>R</sub> form of AChE has been left intact. Deletions were constructed using the Cre-loxP system. The neomycin gene, necessary for the selection of the knockout in embryonic stem cells, was flanked by lox-P sites so that it could be deleted through the action of Cre recombinase. Here we describe the constructs used to make the knockout mice, generating a knockout mouse, transfection experiments of the abbreviated genes in differentiating C2C12 cells that should reflect AChE expression in muscle, and initial data from the knockout mice comparing serum AChE levels.

### ***Knockout constructs***

Table 1 summarizes essential features in the *Ache* gene and in the deletion constructs. All bp numbers in brackets and in the table refer to Genbank accession # AF312033 (6), covering 296820 bases of sequence around the *Ache* gene. Knockout constructs for the alternatively spliced exons of the acetylcholinesterase gene were made in pBluescript SK2+. The "right arm" of all of the constructs spanned the region from the Sal 1 site at [8728] to [12710] for the Delete Exon 5 and Delete Exons 5+6 constructs, and Sal 1 to [13307] for Delete Exon 6. All constructs contained an engineered Cla 1 site for insertion of the neomycin gene. The neomycin gene, flanked by loxP sites (a kind gift of Goran Bucht) replaced the deleted region in all cases. The "left arm" of the constructs started at [12863] for Delete Exon 5 and extended to the BamH 1 site at [17891], while for Delete Exons 5+6 and Delete Exon 6, [13562] was the 5' end of the left arm. All mouse DNA used for the knockout constructs came from clone address 341/C04, BAC Mouse ES Rel II, a 129 SvJ/BAC mouse genomic library from Incyte Genomics or PCR of 129/SvJ embryonic stem (ES) cell DNA, as it is important for knockout DNA constructs to be identical in sequence to that of the ES cells that will be transfected. LoxP sites were tested for integrity by transfecting the constructs into bacteria stably transfected with the Cre recombinase gene (a gift from A. Wynshaw-Boris laboratory at UCSD). Functional loxP sites allowed deletion of the 2kb neomycin gene; this deletion was easy to assess using restriction analysis. LoxP sites were inserted because a large insertion in the gene might disrupt either RNA processing or stability by introducing cryptic splice acceptors in the neomycin gene or by producing a long and unstable 3' untranslated region. Also expression of neighboring genes can be changed by promoter elements from the selection cassette (7).

Feature	5'	3'
Exon 1	~7511	7607
Exon 2	9256	10345
Exon 3	10723	11207
Exon 4	12434	12603
Read-through stop	12693 (TAA)	
Exon 5	12720	12846 (TAA)
Exon 6	13384	13503 (TGA)
Poly A signal #1	13711 (AATAAA)	
Poly A signal #2	14909 (AATAAA)	
Delete exon 5 (ACHE del 5): deleted region	12710	12863
Delete exon 6 (ACHE del 6): deleted region	13307	13562
Delete exons 5+6 (ACHE del 5+6): deleted region	12710	13562
Delete regulatory region in 1 <sup>st</sup> intron (ACHE del RR): floxed region	8183	8438
ACHE total knockout (4): deleted region	7608	13065

**Table 1:** Essential features of the Acetylcholinesterase (Ache) gene and Ache knockout mouse constructs. Exons 1 through 6 are defined as well as the stop codons for the 3 alternative splice options for AChE transcripts. Numbers refer to Reference (6); this sequence includes the Ache gene. The sequence is available as Genebank accession # AF312033.

#### *C2C12 transfections with the Ache gene*

C2C12 cells (ATCC CRL-1772), derived from mouse muscle, grown with high concentrations of fetal bovine serum and kept at sub-confluent densities, divide rapidly as myoblasts and do not produce AChE. When growth conditions are altered by the withdrawal of fetal serum the cells fuse to become multinucleated myotubes and AChE is expressed. A 8.3 kb Hind III genomic fragment [bp 7120-15430] contains all of the essential elements necessary for AChE expression in C2C12 cells (Table 1). This genomic fragment contains the muscle specific promoter region, exons 1-6 and both polyadenylation signals. For propagation purposes the Hind III fragment was cloned into pBluescript SK2+, a vector devoid of mammalian expression components. The "mini-gene" was transfected into C2C12 cells using Lipofectamine Plus (Invitrogen). As shown in Fig. 1a, transfected activity parallels endogenous activity, with no AChE expression in myoblasts and activity that increases with increasing time of differentiation in myotubes. C2C12 expression was used to check the knockout constructs before they were used to make mice. The knockout constructs were extended on the 5' end by adding 5'UTR, the promoter region and part of the first intron (Hind III [7120] to Sal I [8728]). AChE activity was measured after 1 day of growth (no activity was seen in any construct) and 4 days of differentiation. Differentiation media (2% donor horse serum in DME) was changed every day, but for the final 24 hours only DME was used so that expressed exported AChE could be measured.

#### *The knockout mice*

The knockout constructs were transfected via electroporation into 129/SvJ ES cells and selected using G418. An Nhe 1 digest of selected clones was probed with an Nhe 1 [7785] to Aat II [8437] probe to distinguish homologous recombination from random integration. The frequency of homologous recombination ran from 1 to 2.5% for our constructs. Selected colonies were injected into early C57/BL6 blastocysts and then implanted in pseudo-pregnant C57/BL6 mothers. Chimeric pups (showing both the

Cholinesterases in the Second Millennium: *Biomolecular and Pathological Aspects*

agouti coat color of the 129/SvJ cells and the black color of the C57 blastocysts) were then bred back to black mice to determine germline transmission of the altered allele. All agouti pups were genotyped at weaning by PCR. Mice found to be heterozygous for the *Ache* deletion were then inbred to give Delete Exon 5/Neo, Delete Exons 5+6/Neo, and (an anticipated) Delete Exon 6/Neo. Heterozygous /Neo mice were then bred to EIIa-cre mice (8). These transgenic mice express Cre recombinase during very early embryogenesis causing deletion of the floxed neomycin gene, leaving only short sequences flanking the loxP sites that were used in cloning. These matings, to date, have given Delete Exon 5/Cre and Delete Exons 5+6/Cre.

#### Results and Discussion

**C2C12 Transfections:** Fig. 1b shows relative AChE expression of the knockout constructs transfected into C2C12 cells normalized to co-transfected  $\beta$ -galactosidase activity. The most obvious result of these transfections is the lack of activity expressed by constructs containing the neomycin gene, hinting that at least in muscle the presence of the 2kb insert negatively influences RNA processing or stability. Since Del Exon 5/Neo is devoid of enzyme expression, it would seem that RNA splicing is also affected because exons 4 and 6 along with all splice consensus sequences are present, C2C12 cells express the 4/6 splice exclusively, and Delete Exon 5 constructs that do not contain the neomycin gene seem to express AChE even better than the wild type gene. Constructs from which exon 6 has been deleted show less cell associated activity than the wild type gene, but somewhat higher expression in the media. Media and cell extracts from the transfected Delete Exons 5+6/Cre construct were analyzed on sucrose density gradients in both Triton X-100 and Brij 96 (data not shown). All gradients showed a single species running at 4.5S. The AChE expressed is therefore monomeric and neither amphiphilic nor hydrophobic as it does not shift in brij gradients. These results are consistent with expression of an AChE form in which the intron following exon 4 is not spliced.

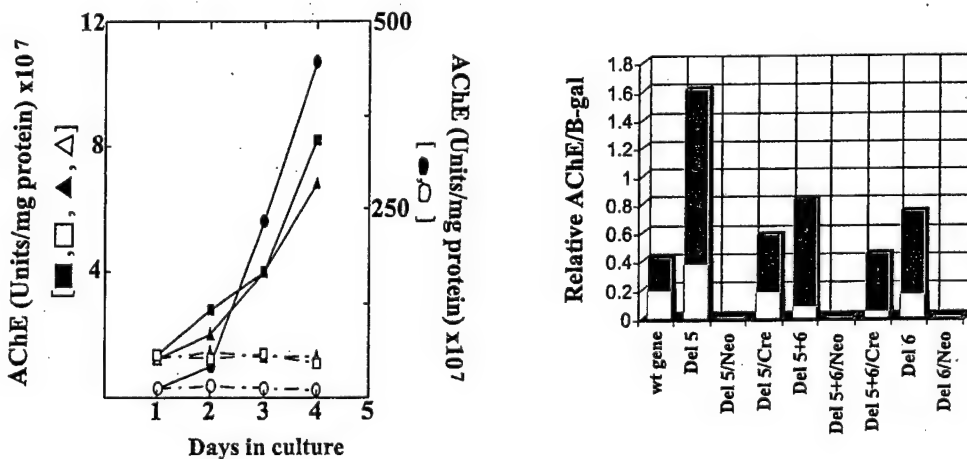


**Figure 1:** (A) AChE expression in C2C12 cells under growth and differentiation conditions. Open symbols, AChE activity during growth conditions, filled symbols, differentiation conditions. Squares represent untransfected cells; triangles, cells transfected with empty vector; and circles, cells transfected with the *Ache* gene (Hind III fragment, [7120 to 15430]). (B) C2C12 cells transfected with *Ache* gene knockout constructs. Cells are transfected and then differentiated for 4 days. Media is changed to DME with no serum 24 hours before cells are harvested. White bars represent cell associated AChE, black bars represent AChE that is exported from the cells to the media. The *Ache* constructs were co-transfected with CMV  $\beta$ -galactosidase and AChE is normalized to  $\beta$ -gal to correct for differing transfection efficiencies between the knockout constructs. Constructs with only the exon deletion, the deletion replaced by the floxed Neomycin gene, and Neomycin removed through exposure to Cre-Recombinase are shown.

**Knockout Mice:** Serum AChE levels of the knockout mice were analyzed at weaning and genotype was analyzed by PCR. These results are compared in figure 2, using the total AChE knockout with no AChE in the serum of the homozygous knockout and 50% of wild type levels in the heterozygote for comparison (4). Constructs retaining the neomycin gene show very low AChE expression levels in serum, homozygous Delete Exon 5/Neo and Delete Exons 5+6/Neo mice are stunted and tremble like the total knockout mouse, but the phenotype is not as severe. Care required to maintain the mice is much less than that required for the total knockout suggesting that very low levels of AChE will suffice to rescue partially the severe knockout phenotype. AChE expression in Delete Exon 5/Cre mice does not yield an evident phenotype at present. Delete Exons 5+6/Cre mice with their strikingly high levels of AChE expression in serum, hint at what happens when AChE cannot properly anchor. It will be interesting to analyze AChE forms in blood as well as RNA expression in AChE rich tissues such as muscle and brain to see if expression levels of AChE RNA are altered by 3' sequences or the lack of available splice options. It remains to be seen what cell types are affected by these deletions and how or if *Ache* gene regulation is affected by the ability of the gene product to anchor in a specific region in various tissues.

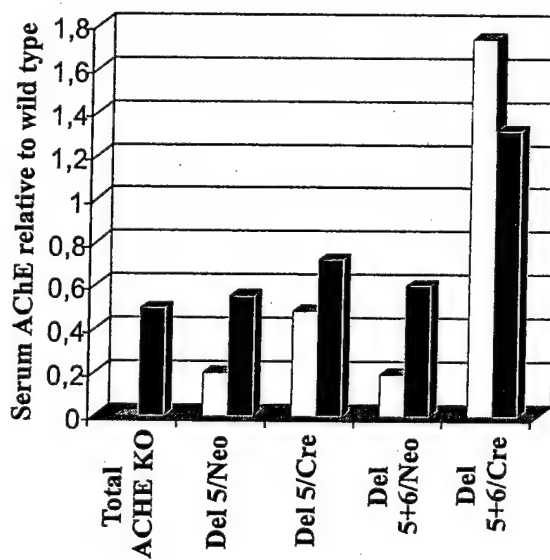


**Figure 2:** AChE expression in mouse serum at weaning. Serum BuChE was inhibited with 50  $\mu$ M Iso-OMPA. White bars represent AChE activity in homozygous mice; both alleles are altered. The black bars represent activity from the heterozygote, one allele is wild type, the other carries the altered *Ache* gene, either containing the neomycin gene (/Neo), or when the neomycin gene has been deleted through breeding to mice carrying the Cre-recombinase gene, (/Cre).

We would like to thank The UCSD Transgenic Core, (<http://cancer.ucsd.edu/tgm>) for ES cell transfections and blastocyst injections, A. Wynshaw-Boris for invaluable advice and expertise. A special thanks to Goran Bucht who made the original Delete Exon 5 construct that was altered to meet the needs of this project. Finally, we are indebted to Oksana Lockridge and the total AChE knockout mice who paved the way for these exon-deleted mice.

Cholinesterases in the Second Millennium: *Biomolecular and Pathological Aspects*

**References**

1. Li Y, Camp S, Rachinsky T, Getman D, Taylor P. *J. Biol. Chem.* 1991; 266:23083-23090.
2. Massoulie J. *Neurosignals* 2002; 11:130-143.
3. Massoulie J, Anselmet A, Bon S, Krejci E, Legay C, Morel N, Simon S. *J Physiol Paris.* 1998; 92:83-90.
4. Perrier AL, Massoulie J, Krejci E. *Neuron.* 2002; 33:275-85.
5. Xie W, Stribley JA, Chatonnet A, Wilder PJ, Rizzino A, McComb RD, Taylor P, Hinrichs SH, Lockridge O. *J Pharmacol Exp Ther.* 2000; 293:896-902.
6. Wilson MD, Riemer C, Martindale DW, Schnupf P, Boright AP, Cheung TL, Hardy DM, Schwartz S, Scherer SW, Tsui LC, Miller W, Koop BF. *Nucleic Acids Res.* 2001; 29:1352-65. Genebank accession # AF312033.
7. Hasty P, Abuin A, Bradley A. In *Gene Targeting: a practical approach* (ed. AL Joyner). 2000; Oxford University Press Inc., New York.
8. Xu X, Li C, Garrett-Beal L, Larson D, Wynshaw-Boris A, Deng CX. *Genesis.* 2001; 30:1-6.

# Freeze-frame inhibitor captures acetylcholinesterase in a unique conformation

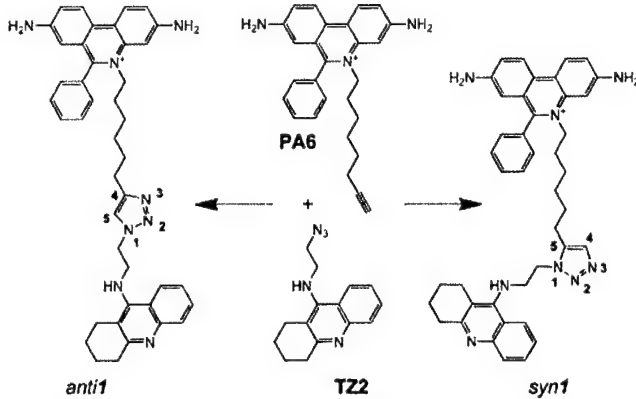
Yves Bourne<sup>\*†</sup>, Hartmuth C. Kolb<sup>‡</sup>, Zoran Radić<sup>§</sup>, K. Barry Sharpless<sup>\*†</sup>, Palmer Taylor<sup>§</sup>, and Pascale Marchot<sup>†||</sup>

<sup>†</sup>Ingénierie des Protéines, Centre National de la Recherche Scientifique Unité Mixte de Recherche-6560, Institut Fédératif de Recherche Jean Roche, Université de la Méditerranée, Faculté de Médecine Secteur Nord, F-13916 Marseille Cedex 20, France; <sup>\*</sup>Architecture et Fonction des Macromolécules Biologiques, Centre National de la Recherche Scientifique Unité Mixte de Recherche-6098, 31 Chemin Joseph Aiguier, F-13402 Marseille Cedex 20, France; <sup>‡</sup>Department of Chemistry, <sup>||</sup>The Skaggs Institute for Chemical Biology, The Scripps Research Institute, La Jolla, CA 92037; and <sup>§</sup>Department of Pharmacology, University of California at San Diego, La Jolla, CA 92093-0636

Contributed by K. Barry Sharpless, December 10, 2003

The 1,3-dipolar cycloaddition reaction between unactivated azides and acetylenes proceeds exceedingly slowly at room temperature. However, considerable rate acceleration is observed when this reaction occurs inside the active center gorge of acetylcholinesterase (AChE) between certain azide and acetylene reactants, attached via methylene chains to specific inhibitor moieties selective for the active center and peripheral site of the enzyme. AChE catalyzes the formation of its own inhibitor in a highly selective fashion: only a single *syn1*-triazole regioisomer with defined substitution positions and linker distances is generated from a series of reagent combinations. Inhibition measurements revealed this *syn1*-triazole isomer to be the highest affinity reversible organic inhibitor of AChE with association rate constants near the diffusion limit. The corresponding *anti1* isomer, not formed by the enzyme, proved to be a respectable but weaker inhibitor. The crystal structures of the *syn1*- and *anti1*-mouse AChE complexes at 2.45- to 2.65-Å resolution reveal not only substantial binding contributions from the triazole moieties, but also that binding of the *syn1* isomer induces large and unprecedented enzyme conformational changes not observed in the *anti1* complex nor predicted from structures of the apoenzyme and complexes with the precursor reactants. Hence, the freeze-frame reaction offers both a strategically original approach for drug discovery and a means for kinetically controlled capture, as a high-affinity complex between the enzyme and its self-created inhibitor, of a highly reactive minor abundance conformer of a fluctuating protein template.

Acetylcholinesterase (AChE) rapidly terminates cholinergic neurotransmission by catalyzing the hydrolysis of the neurotransmitter, acetylcholine, and inhibitors of AChE have been used for over a century in various therapeutic regimens (1, 2). The structure of the target enzyme reveals a narrow gorge ≈20 Å in depth with the catalytic triad of the active center at its base (3). Distinctive inhibitors bind to the active center or to a peripheral anionic site (PAS) located at the rim of the gorge near the enzyme surface (4–6). Previously, we generated a library of active site and PAS inhibitors with respective tacrine and phenanthridinium nuclei, each equipped with an azide or acetylene group at the end of a flexible methylene chain, to enable the reporting 1,3-dipolar cycloaddition to occur (Scheme 1) (7). AChE itself served as the reaction vessel, synthesizing its own inhibitor from these building blocks, in effect, by equilibrium-controlled sampling of various possible pairs of reactants in its active center gorge until irreversible cycloaddition between azide and acetylene ensued at an intersecting point within the gorge, between the two anchoring positions. From 49 building block combinations, the enzyme selected the TZ2/PA6 pair to form, with an enhanced reaction rate, a highly regioselective *syn1* triazole as the sole product (Scheme 1). In contrast, chemical synthesis by thermal reaction in the absence of enzyme proceeds very slowly and provides an ≈1:1 mixture of *syn1* and *anti1* regioisomers, which differ in the nitrogen substitution positions on the 1,2,3-triazole. Although both are high-affinity inhibitors, the *syn1* isomer, with a 100-fold greater affinity and a subpic-



Scheme 1. Structures of the *anti1* and *syn1* TZ2PA6 regioisomers formed by 1,3-dipolar cycloaddition (7). The phenylphenanthridinium, triazole, and tacrine moieties are shown from top to bottom.

molar dissociation constant for certain AChEs (7), has a potency greater than all known noncovalent organic AChE inhibitors and high selectivity for individual cholinesterases.

The discovery that enzymes can serve as atomic-scale reaction templates for creating their own inhibitors offers an original approach to drug discovery. In this light, we have solved the crystal structures of complexes of mouse AChE (mAChE) (8, 9) with the TZ2PA6 *anti1* and *syn1* regioisomers at 2.45- and 2.65-Å resolution (Table 1 and Fig. 1) and have analyzed further their respective binding kinetics and affinities (Table 2). We show that the distinctive binding properties of the two isomers in solution are related to discrete rearrangements in both the ligand and enzyme conformations. Indeed, the active center gorge and PAS conformations for the two crystalline complexes differ greatly, where binding of the higher affinity *syn1* isomer unveils a unique enzyme conformation not predicted from the structures of either the apo form or the complexes with the precursor reactants (10, 11). Hence these structures reveal that the *syn1* compound specifically formed on the enzyme effectively freezes in frame a highly reactive AChE conformer, and that the two TZ2PA6 regioisomers select distinct conformations from an unliganded enzyme that is presumably fluctuating between multiple conformational states. Because the unique structural features seen for the *syn1*-mAChE complex likely reflect the unique proximity

Abbreviations: AChE, acetylcholinesterase; mAChE, mouse AChE; PAS, peripheral anionic site.

Data deposition: The atomic coordinates and structure factors of the *anti1*- and *syn1*-mAChE complex structures have been deposited in the Protein Data Bank, www.rcsb.org (PDB ID codes 1Q84 and 1Q83, respectively).

<sup>†</sup>To whom correspondence may be addressed. E-mail: marchot.p@jean-roche.univ-mrs.fr or yves@afmb.cnrs-mrs.fr.

© 2004 by The National Academy of Sciences of the USA

**Table 1.** Data collection and refinement statistics

	TZ2PA6 isomer complexed to mAChE	
	anti1	syn1
<b>Data collection*</b>		
Beamline (European Synchrotron Radiation Facility)	ID14-EH1	ID14-EH2
Wavelength, Å	0.933	0.933
Resolution range, Å	25–2.45	25–2.65
Total observations	549,476	513,851
Unique reflections	74,834	59,650
Multiplicity	3.9	3.6
Completeness, %	99.8 (99.7)	99.8 (99.9)
$I/\sigma(I)$	9.3 (1.8)	8.2 (1.8)
$R_{\text{sym}}^{\dagger}$	5.7 (43.5)	6.5 (42.0)
<b>Refinement†</b>		
R factor/ $R_{\text{free}}$ , %	18.4/21.4	18.1/22.0
rms deviation§		
Bonds, Å/angles, °	0.015/1.5	0.015/1.5
Chiral volume, Å³	0.085	0.084
Mean B factors, Å		
Main/side chains	53.4/55.2	49.7/51.6
Solvent/carbohydrate	50.8/91.5	46.7/95.2
Ligand/polyethylene glycol	63.5/72.2	57.2/66.3
rms deviation on B factors, Å²		
Main/side chains	0.9/1.6	0.9/1.6

\*Values in parentheses are those for the last shell.

† $R_{\text{sym}} = |I - \langle I \rangle| / \sum I$ , where  $I$  is an individual reflection measurement and  $\langle I \rangle$  is the mean intensity for symmetry-related reflections.

‡R factor =  $\sum ||F_o| - |F_c|| / \sum |F_o|$ , where  $F_o$  and  $F_c$  are observed and calculated structure factors, respectively.  $R_{\text{free}}$  is calculated for 2% of randomly selected reflections excluded from refinement.

§rms deviation from ideal values.

of reactants causing the higher affinity syn1 isomer to be the sole reaction product *in situ*, these structures also provide insights on the cycloaddition reaction occurring on a flexible protein template and at a locus remote from the anchoring binding sites of the precursors. Thus, the unique structure of the complex captured by click chemistry leads to an unusual strategy for drug design where the most selective agents induce distinctive conformational states of the target.

## Experimental Procedures

**Preparation and Analysis of the Complexes.** The TZ2PA6 anti1 and syn1 isomers were synthesized as described (7). Monomeric mAChE expressed from human embryonic kidney-293 cells (9) was purified by affinity chromatography by using propidium elution (10). The anti1- and syn1-mAChE complexes were prepared by using a 2-fold molar excess of the inhibitors and concentrations well above their  $K_{\text{d}}$ s ( $\approx 135 \mu\text{M}$  i.e.,  $15 \times 10^6 \times K_{\text{i(anti)}} + 330 \times 10^6 \times K_{\text{i(syn)}}$ ; Table 2) (7, 10). Titration of the isomer stock solutions ( $\epsilon_{490\text{nm}} = 6,000 \text{ M}^{-1}\cdot\text{cm}^{-1}$ ) and analysis of the complex solutions were carried out spectrophotometrically (10).

**Crystallization and Data Collection.** Crystallization was achieved at 4°C by vapor diffusion by using hanging drops (1–2  $\mu\text{l}$ ) and a protein-to-well solution ratio of 1:1 with polyethylene glycol-600 25–32% (vol/vol) in 20–100 mM Hepes, pH 6.0–7.5, as the well solution. The crystals were directly flash-cooled in the nitrogen gas stream (100 K); optimal occupancies of the crystalline PASs were controlled by spectrophotometry before data collection (10). The crystals belonged to the orthorhombic space group P2<sub>1</sub>2<sub>1</sub>2<sub>1</sub> with unit cell dimensions  $a = 79.7 \text{ \AA}$ ,  $b = 111.9 \text{ \AA}$ , and  $c = 226.5 \text{ \AA}$ .

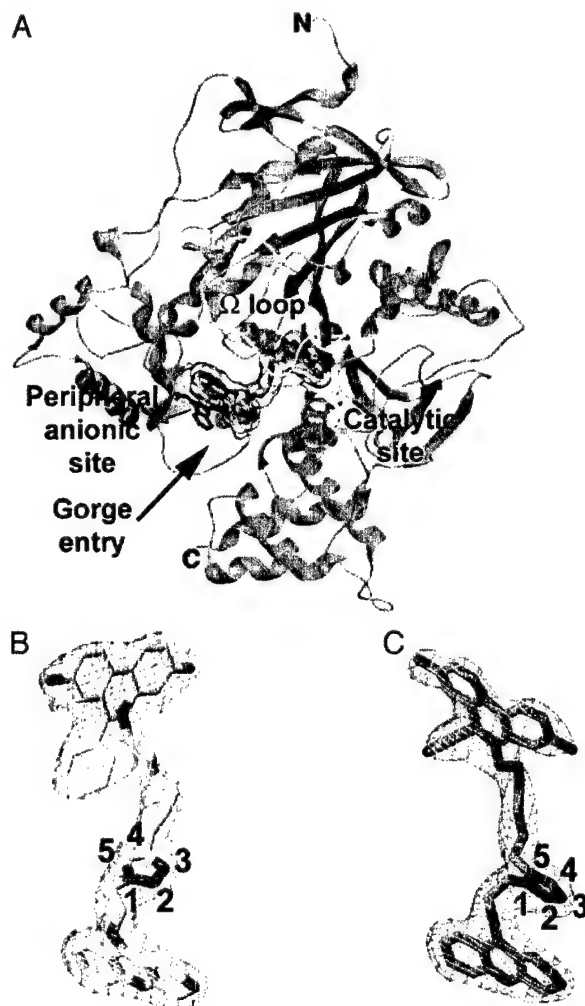


**Fig. 1.** Overall fold and structural quality of the TZ2PA6–mAChE complexes. (A) Overall view of the mAChE molecule (cyan ribbon) showing the syn1 isomer (orange bonds; transparent molecular surface) bound within the enzyme active-site gorge; the long  $\Omega$  loop Cys-69-Cys-96 is displayed in yellow. (B and C) Determined structures of the bound anti1 and syn1 isomers (yellow and orange bonds, respectively; blue nitrogens; numbered triazole atoms; same orientation as in Scheme 1), with the respective 2.45- and 2.65-Å resolution final  $2F_o - F_c$  electron density maps contoured at 1  $\sigma$  (cyan).

Oscillation images were integrated with DENZO (12), and data were scaled and merged with SCALA (13).

**Structure Determination and Refinement.** Coordinates of the anti1 and syn1 molecules were obtained from docked simulations of TZ2PA6–TcAChE complexes (7). The apo-mAChE structure (Protein Data Bank ID code 1J06) (10) without solvent was used as a starting model to refine the anti1- and syn1-mAChE complex structures with CNS (14) and REFMAC (15) (Table 1). Rigid-body refinements on each of the two subunits in the crystalline mAChE dimer (10) gave  $R$  factor values of 25.2% and 24.8% ( $R_{\text{free}}$  values of 25.8% and 25.3%) for the anti1 and syn1 complexes, respectively, by using all data in the 25- to 2.45/2.65-Å resolution range. The resulting  $2F_o - F_c$  and  $F_o - F_c$  electron density maps were used to position the inhibitors and correct the protein model with the graphics program TURBO-FRODO (16).

The final two TZ2PA6–mAChE structures comprise residues Glu-1-Ala-541 and Glu-4-Thr-540 for the two mAChE mole-

**Table 2.** Kinetic parameters for inhibition of various cholinesterases by the TZ2PA6 isomers

Enzyme	syn1			anti1		
	$k_{on}$ , $10^{10} \text{ M}^{-1} \cdot \text{min}^{-1}$	$k_{off}$ , $10^{-3} \text{ min}^{-1}$	$K_i$ , fM	$k_{on}$ , $10^{10} \text{ M}^{-1} \cdot \text{min}^{-1}$	$k_{off}$ , $10^{-3} \text{ min}^{-1}$	$K_i$ , fM
mAChE*	1.7	7.1	410	2.5	220	8,900
mAChE mutant Trp286Ala	0.94	19	2,000	0.87	1,800	210,000
AChE, <i>Electrophorus electricus</i> *	1.5	1.5	99	1.8	250	14,000
AChE, <i>Torpedo californica</i> *	1.4	1.1	77	3.2	23	720
AChE, <i>Drosophila melanogaster</i>	2.0	72	3,600	3.4	58	1,700
Butyrylcholinesterase, mouse	0.36	2.6	720	0.69	3.2	460

Parameters are means of  $n \geq 3$  individual values with SD  $\leq 20\%$ .

\*Modified from ref. 7.

cules in the asymmetric unit (10). High-temperature factors and weak electron densities are associated with residues Cys-257, Pro-258, and Asp-265 in the short  $\Omega$  loop Cys-257-Cys-272 and with the surface loop region Asp-491-Pro-498. The average rms deviation (rmsd) between the *anti1* and *syn1* complex structures is 0.24 Å for 535  $\text{C}\alpha$  atoms. Between the *anti1* and *syn1* complexes and the apo form, the rmsds are 0.19 and 0.23 Å for 534 and 533  $\text{C}\alpha$  atoms, respectively. The stereochemistries of the bound isomers were checked by using the MM2 force field as implemented in MACROMODEL (17). Those of the structures were analyzed with PROCHECK (18); with the exception of the catalytic Ser-203, no residues were found in the disallowed regions of the Ramachandran plot. Figs. 1–3 were generated with SPOCK (19) and RASTER3D (20).

**Inhibition Studies.** Inhibition constants were measured from the ratio of dissociation and association rates ascertained by conventional mixing and stopped-flow instrumentation (7). The mAChE Trp286Ala mutant was expressed, sequence verified, and concentrated from the expression medium as described (21). Purified AChE from *D. melanogaster* was a gift from D. Fournier (Institut de Pharmacologie et de Biologie Structurale, Toulouse, France).

## Results and Discussion

**Overall View of the TZ2PA6–mAChE Complexes.** The structures of mAChE in complexes with the *anti1* and *syn1* regioisomers (Fig. 1) show the canonical catalytic subunit, made up of a 12-stranded central  $\beta$ -sheet surrounded by 14  $\alpha$ -helices (10, 22, 23), and well-ordered bound inhibitor molecules. The isomer-binding site may be deconstructed into three discrete loci: (*i*) the active center at the base of the gorge that binds the tacrine moiety; (*ii*) an intervening site in the constricted region within the gorge that associates with the triazole moiety and adjacent methylene groups; and (*iii*) the PAS at the rim of the gorge that binds the phenylphenanthridinium moiety.

**The anti1–mAChE Complex.** In the *anti1* complex, the tacrine moiety is positioned at the base of the mAChE gorge similar to the *T. californica* AChE–tacrine complex (11) (Fig. 2*A*). However, the density maps clearly reveal a slight bend in the moiety that may enhance  $\pi$ – $\pi$  stacking of the tetrahydroaminoacridine ring inserted between the Trp-86 and Tyr-337 aromatic side chains. At the region of constriction formed by the side chains of Tyr-124, Phe-297, Tyr-337, and Phe-338,  $\approx$ 5–8 Å into the gorge, the triazole establishes van der Waals contacts with the Phe-297 and Tyr-341 side chains. The hydroxyl groups of Tyr-337 and Tyr-124, on opposite sides of the gorge, are hydrogen-bonded to the triazole N2 and N3 atoms and may interact with the heteroaromatic  $\pi$ -system. The dimethylene linker connecting the tacrine and triazole is well ordered within the gorge and in van der Waals contact with the side chains of the conserved residues Asp-74, Tyr-124, and Tyr-341.

At the PAS, the phenylphenanthridinium moiety is positioned by the hexamethylene chain that links it to the triazole. Major interactions include a near-parallel stacking of the planar phenanthridinium with the Trp-286 indole, an edge-to-face arrangement with the Tyr-72 ring, and stabilizing interactions with the Ser-293 hydroxyl and Gln-291 carbonyl (Figs. 2*A* and 3*A*). The *anti1* exocyclic phenyl moiety, nearly buried at the gorge entrance and in a T shaped arrangement with the Tyr-72 and Trp-286 side chains, orients to establish van der Waals contacts with the Asp-74, Tyr-124, and Tyr-341 side chains and hydrogen bonds with the Tyr-72 hydroxyl and Ser-293 N, O, and O $\gamma$  atoms. Partial delocalization of electrons between the Trp-286 indole and the phenanthridinium observed in the density maps suggests formation of a charge–transfer complex, similar to that observed in the decidium–mAChE complex (10) (Fig. 2*D*).

The architecture of the PAS region in the *anti1*–mAChE complex (Figs. 2*A* and 3*A*) is virtually identical to that seen in the decidium– and propidium–mAChE complexes (10), and the major interactions involved in the phenanthridinium–Trp-286 stacking are retained (Fig. 2*D*). Yet the phenylphenanthridinium adopts distinctive orientations in the PAS in the three complexes. In the *anti1* complex, the phenanthridinium is rotated by  $\approx$ 180° around its centroid axis, whereas this centroid is translated by 1.5 Å from its position in the other two complexes. This positioning leads to stabilizing interactions of the *anti1* phenanthridinium with the Gln-291 and Ser-293 side chains, instead of the His-287 imidazole located across the gorge opening, and to a distinct environment for the exocyclic phenyl group. This versatility in the rotational and translational orientations of the bound phenylphenanthridinium relative to the Trp-286 side chain adds a new dimension to the design of molecules that associate with the PAS region.

**The syn1–mAChE Complex.** The structure of the *syn1*–mAChE complex differs considerably from that of the *anti1*–mAChE complex, due to the respective 1,5- and 1,4-disubstitution of the *syn1* and *anti1* 1,2,3-triazole rings (Scheme 1, Fig. 1). The *anti1* isomer adopts an elongated flat shape, whereas the *syn1* isomer presents a corkscrew-like topology that provides greater surface complementarity with the gorge walls, resulting in fewer solvent-filled voids around the bound *syn1* (Figs. 2*B* and *C* and 3*B*). Whereas the tacrine moiety in both complexes is positioned similarly within the active site, the triazole in the *syn1* complex is shifted 2 Å deeper into the gorge, where it is held in place by the tacrine ring and the Phe-297 and Phe-338 side chains. Consequently, a single  $\pi$ -aromatic interaction may exist between the *syn1* triazole and Tyr-124 hydroxyl, and a water-bridged hydrogen bond is created between the triazole N3 and the catalytic Ser-203 O $\gamma$  and Gly-121 amide backbone. Additional van der Waals contacts occur between the triazole and the Gly-121-Gly-122 dipeptide backbone and Tyr-124 side chain. The shifted *syn1* triazole occludes the Tyr-337 ring, which sweeps

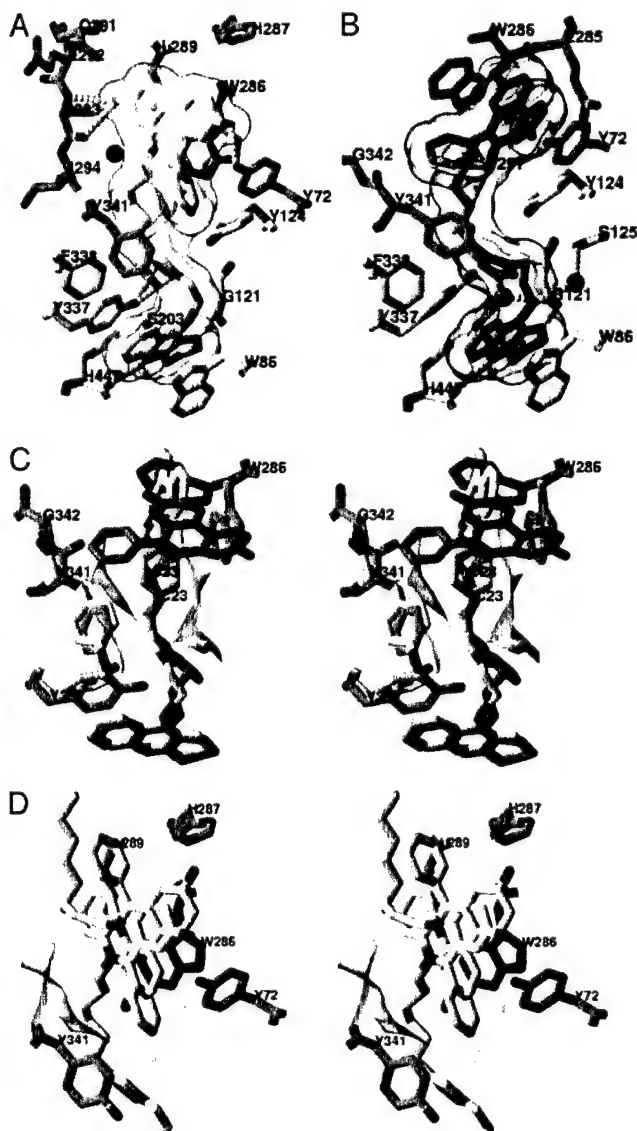


**Fig. 2.** Close-up views of the TZ2PA6–mAChE complexes. (*A* and *B*) Bound *anti1* and *syn1* isomers (colored as in Fig. 1) with interacting mAChE side chains colored white, yellow, and green/magenta (blue, nitrogens; red, oxygens) for those that respectively interact with the tacrine, triazole, and phenanthridinium moieties of the isomers. The isomer molecular surfaces are displayed in transparency. The side chains of the catalytic residues Ser-203, Glu-334, and His-447 are shown as white bonds, and hydrogen bonds between mAChE residues and the isomers are shown as white dotted lines. (*C*) Stereo superimposition of the *anti1* and *syn1* complexes (colored as in *A* and *B*) according to all C $\alpha$  atoms of mAChE. The side chains of residues Trp-286 and Tyr-337 and of dipeptide Tyr-341-Gly-342, which adopt distinctive positions in the complexes, are shown in magenta and green, respectively. The  $\chi$  values for the Trp-286 side chain are (*anti*)  $\chi_1 = -73^\circ$ ,  $\chi_2 = 100^\circ$ ; (*syn*)  $\chi_1 = -158^\circ$ ,  $\chi_2 = 50^\circ$ . (*D*) Stereo superimposition of the *anti1* complex with the decidium–mAChE complex (Protein Data Bank ID code 1J07; ref. 10) according to all C $\alpha$  atoms of mAChE in the two complexes. The *anti1* and decidium phenylphenanthridinium moieties (yellow and white bonds, respectively; blue, nitrogens) adopt distinct positions and orientations relative to Trp-286 in the PAS, whereas their alkyl chains diverge. The side chains of the PAS residues are highlighted in green (blue, nitrogens; red, oxygens). The mAChE molecular surface buried at the *anti1* complex interface is displayed in transparency.

out in a 60° arc, resulting in a hydroxyl group displacement of 4.5 Å and in new interactions with the Tyr-341 ring near the gorge entry.

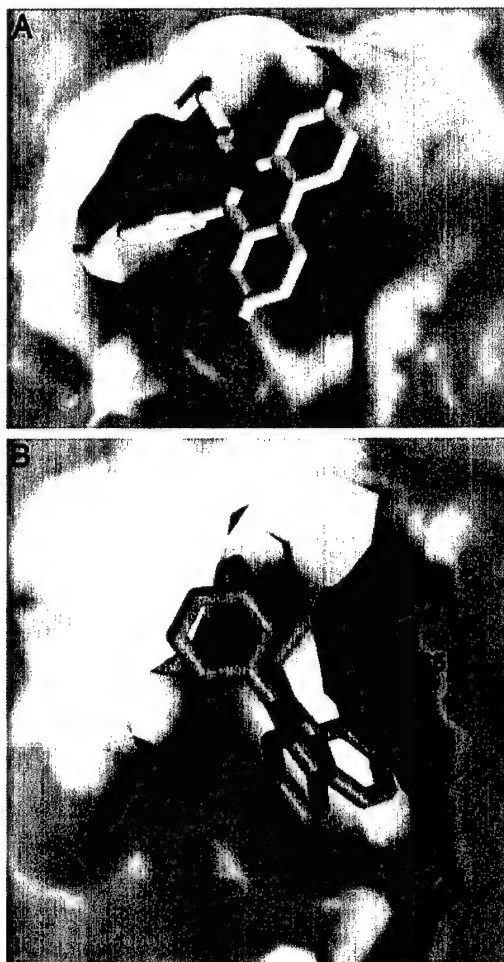


**Fig. 3.** Distinctive topographies of the PAS regions in the *anti1* and *syn1* complexes. Views of the PAS region of mAChE bound to the phenanthridinium moiety present in the *anti1* (*A*) and *syn1* (*B*) isomers (colored as in Figs. 1 and 2). The mAChE molecular surfaces buried at the complex interfaces are shown in yellow, with the Tyr-72 and Trp-286 side chains highlighted in green and magenta, respectively. The mAChE surface areas (Connolly's surfaces) buried to a 1.6-Å radius probe at the *anti1* and *syn1* complex interfaces by the phenylphenanthridinium and linker first carbon are 256 and 313 Å<sup>2</sup> (the double-face burying of the *syn1* phenanthridinium being counterbalanced by the deeper burying of the *anti1* phenyl). The gorge mouth openings (Richards' surface) for the *anti1* and *syn1* complexes are 14 and 29 Å<sup>2</sup>, respectively.

The position and orientation of the *syn1* triazole at the gorge constriction influence the phenylphenanthridinium position at the PAS (Figs. 2*B* and *C* and 3*B*). Compared to the *anti1* complex, the overall span of the linker is shortened by 1.5 Å in the more compact *syn1* triazole, a value close to the length of a C–C bond (Fig. 1*B* and *C*). As a result of the reduced linking distance, the *syn1* phenanthridinium moiety is constrained to a narrow region deep within the gorge where it would sterically clash with the Trp-286 indole. This causes the Trp-286 side chain to be dislodged from the PAS surface and to swing into the solvent, with differences of 85° and 50° in the  $\chi_1$  and  $\chi_2$  values, respectively. This distinct side chain conformation enlarges the opening at the gorge rim 2-fold, creating a 10 × 9 Å groove delimited by the Tyr-72 and uniquely positioned Trp-286 side chains on each side and by Glu-285 at its base, wherein the phenanthridinium tightly intercalates (Figs. 2*B* and *C* and 3*B*). Hence, the aromatic plate of the *syn1* phenanthridinium, oriented 90° from its position in the *anti1* complex, is wedged

neatly between the two aromatic side chains where it is stabilized by  $\pi$ - $\pi$  interactions with centroids separated by 3.6–3.8 Å. This causes the phenyl group to become solvent exposed and establish discrete van der Waals contacts with residues Leu-76, Tyr-341, and Gly-342 at the gorge rim.

**Kinetic Analysis of *syn1* and *anti1* Isomer Binding.** Comparison of the relative rates of association and dissociation shows that the enhanced affinity of the *syn1* isomer for mAChE largely results from a slower dissociation rate (Table 2). The small differences seen in the association rates would be anticipated in view of the rates being at or near the diffusion rate limit. Hence the enhanced affinity of the *syn1* isomer is reflected in a greater activation barrier for dissociation of the complex. Several conformational changes and positional rearrangements of side chains observed within the PAS and active-site gorge correlate with the *syn1* isomer being more tightly sequestered in the active site gorge.

The *syn1* isomer displays up to 5-fold greater affinity for *E. electricus* and *T. californica* AChEs than for mAChE, and the selectivity of *E. electricus* AChE for the *syn1* isomer is as much as 300-fold higher than that of any other AChE species assayed (Table 2). Only low-resolution structures of *E. electricus* AChE are available (24), but the limited sequence differences found at the PAS and within the gorge do not reveal particular determinants responsible for the higher selectivity. In contrast, *D. melanogaster* AChE, with its Glu, Tyr, and Met substitutions for mAChE residues Tyr-72, Asp-74, and Tyr-124, and mouse butyrylcholinesterase, with its Arg and Asn substitutions for Trp-286 and Tyr-72 (see <http://bioweb.ensam.inra.fr/ESTHER/general?what=index>), show an inverted but small selectivity for the *anti1* isomer, consistent with a more open gorge and fewer aromatic side chains at the PAS in these enzymes. Moreover, removal of the indole ring at the rim of the mAChE gorge by a Trp286Ala mutation results in higher dissociation rates and up to 20-fold reduction in affinity for the *syn1* and *anti1* complexes. These results further emphasize the importance of the peripheral aromatic side chains in trapping the *syn1* phenanthridinium and of Trp-286 in stabilizing both complexes despite the distinctive orientations of the indole side chain.

**Functional Role of the Central Triazole Moiety.** The triazole moieties of the *syn1*- and *anti1*-mAChE complexes are both tightly bound within the gorge, due to rearrangements in both ligand position and mAChE conformation (Fig. 2). Hence, the triazoles actively contribute to the binding interactions in the respective complexes instead of acting as passive linkers. The high affinities of the complexes (Table 2) arise not only from proximity reducing entropic contributions for a “divalent” ligand with separate binding groups but also from interactions along the gorge wall. The observation that the alternate synthesis product TZ6PA2 with inverted dimethylene and hexamethylene linkers is a weak AChE inhibitor (7) provides additional evidence for specific position-sensitive triazole contributions to the overall binding energy. The formative adaptability of this five-membered heterocycle is reflected in *syn1* cycloaddition occurring with the azide and acetylene extended in a parallel orientation, effectively shortening the intervening linker through the triazole by one bond length, whereas they would lie antiparallel in formation of the *anti1* triazole product (7). The triazole’s large dipole (>5 Debye), which bisects the ring plane near atoms N3 and C5 (Scheme 1, Fig. 1B and C), and the capacity of the N2 and N3 electron lone pairs to serve as hydrogen bond acceptors not only enhance binding affinity but also contribute to the efficiency of the 1,3-dipolar-coupling reaction. The conformation of the *syn1* complex is congruent with *syn1*’s shorter linker, compared to the *anti1* complex. This is evident from the positioning of the phenanthridinium at the PAS, where it resides closer to

the tetrahydroaminoacridine in the *syn1* than in the *anti1* complex (Fig. 1B and C, Fig. 2C). To achieve this disposition of proximal reactants, a substantial conformational change occurs at the rim of the gorge with a secondary change evident in the vicinity of the triazole formed by the cycloaddition (Figs. 2C and 3). Hence, the reactivity of the azide and acetylene precursors in the gorge and the resulting affinity of the triazole formed could not have been predicted from structures of apo-AChE (10) or of complexes with close congeners to the precursors (10, 11). To date, inhibitors containing substituted 1,2,3-triazoles have been observed only in plant glycolate oxidase inhibitors (25) and  $\beta$ -lactam antimicrobials (26).

**Functional Role of the Trp-286 Indole.** Most AChE crystal structures show the Trp-286 side chain centered in the PAS with one face of the indole buried at the rim of the gorge and the other occluded by either a symmetry-related AChE molecule or a bound PAS ligand (ref. 3, and subsequent structures derived from the same TcAChE crystal form; refs. 10, 11, 22, 23, 27, and 28). Only the apo-mAChE structure (10), solved from the crystal form used here, shows the Trp-286 external face fully accessible to solvent, providing it with potential mobility. Indeed, binding of the *syn1* isomer displaces the Trp-286 side chain from the AChE hydrophobic core toward the solvent, with one face of the indole now stacked with the phenanthridinium and the other face still exposed to the solvent and in van der Waals contact with Leu-289 (Figs. 2C and 3). One of the phenanthridinium rings is buried in a near-parallel stacking interaction with the Tyr-124 ring at the bottom of the groove, whereas the other two rings insert into the Trp-286-Tyr-72 parallel sandwich. The buried phenanthridinium amino group is hydrogen bonded to Glu-285. Whereas the phenanthridinium ring system in the bound *anti1* isomer is virtually planar, the *syn1* system adopts a slightly curved shape conforming to the induced groove where it intercalates.

Indirect evidence suggests that the PAS region, with its surface-exposed aromatic groups, may be responsible for the adhesion properties of AChE (29). Recognition and adhesion play important roles in synapse maintenance, as seen with the structurally related neuroglinins (30). They may also play a role for the AChE-promoted nucleation of amyloid peptides in the Alzheimer’s disease pathogenesis (31). The flip in the Trp-286 indole and the newfound  $\pi$ - $\pi$  and cation- $\pi$  interactions seen in the *syn* complex raise the possibility that an open conformation of AChE with distinctive exposure of aromatic groups is involved in these adhesion functions.  $\pi$ -orbital stacking mediated by aromatic side chains is instrumental in other molecular recognition and cell adhesion processes (32). Other intercalations of polycyclic aromatic compounds between protein aromatic side chains or nucleotide bases involve the isoalloxazine moiety of the flavin cofactor and flavodoxin (33); ethidium derivatives and the multidrug-resistant-binding protein QacR (34) and adjacent base pairs (see Nucleic Acid Database, code 1JTY); the benzothiazole moiety of thioflavin and DNA (35) and  $\beta$ -sheet amyloid structures (36); and perhaps thioflavin and the PAS of AChE (37).

**Role of the AChE Gorge Flexibility in Catalysis and Inhibitor Binding.** Controversy surrounds how AChE, with its catalytic triad at the base of a narrow gorge, sustains high catalytic efficiency. Alternate portals for substrate and product access have been proposed (38); however, catalytic and inhibitor-binding parameters are influenced only by mutations in the gorge (21) and not in the vicinity of the putative additional portals (39). Rapid fluctuations giving rise to transient enlargements of the gorge appear critical (40). Ligand binding evidently induces a closed gorge state, whereas the unliganded enzyme seems to fluctuate rapidly between multiple states with varying degrees of gorge openness (41, 42).

Previous structural analysis of PAS ligands associated with

mAChE showed that the tips of the long  $\Omega$  loop Cys-69-Cys-96 and loop Val-340-Gly-342 bordering on the gorge (Fig. 1A) possessed sufficient mobility to enlarge the gorge entry, thereby facilitating access to and from the active center (10). In fact, only the *syn1*-mAChE complex exhibits an increase of up to 12 Å in the mean temperature factors for residues at the loop tips where movement of 1.2 Å of Leu-76 and an inversion of the Gly-342 carbonyl carbon occur; the weak electron densities for the Leu-76 and Tyr-341 side chains are also consistent with substantial localized fluctuations. Hence, the flexibility of the AChE long  $\Omega$  loop differs from the hinge-like motion of a homologous loop that, in the structurally related lipases, forms a rigid flap and opens only in the presence of the lipid substrate (43, 44). Moreover, ligand binding to AChE may cause the gorge to collapse around the ligand, minimizing internal dimensions (41, 42). This notion is supported by the observed repositioning of the Tyr-337 side chain and associated perturbation of Tyr-341, which not only alter the gorge shape but also enlarge its width at the position of constriction to accommodate the *syn1* triazole (Fig. 2C). Such large conformational changes involving these residues were not observed for the PAS or active center complexes from which the precursor reactants were designed (10, 11). These computational and experimental results point to concerted fluctuations all along the gorge, which may facilitate access of incoming substrate to the active site at the gorge base and presumably occur in short time frames relative to diffusional translation of substrate (40).

In summary, the use of the enzyme active-site gorge as an atomic-scale template for inhibitor synthesis (7) and of structural

analyses of the *anti1*- and *syn1*-mAChE complexes has revealed (i) an *in situ* phenomenon (7) that bears an uncanny resemblance to pioneering studies begun in 1983 by W. L. Mock (45); (ii) inherent flexibility and conformational fluctuations in the AChE molecule; and (iii) a most stable and selective complex that could not have been predicted from the apo-enzyme structure (10). The highly exergonic nature of the 1,3-dipolar-[2 + 3]-cycloaddition ( $\Delta H > 50$  kcal/mol) has allowed us to immobilize and then identify by structural means an otherwise minor abundance conformation of the enzyme. Because only the higher-affinity *syn1*-triazole regioisomer is associated with major changes in enzyme conformation, the crystalline *syn1*-mAChE complex becomes the lead template in the design of selective pharmacologic agents directed toward the catalytic or noncatalytic functions of AChE. If, in fact, AChE through its PAS plays a role in synaptic adhesion processes and in nucleating plaque formation associated with dementia (29), then AChE inhibitors that also influence surface conformation may offer a means of enhancing therapeutic efficacy.

We are grateful to D. Fournier for providing the *D. melanogaster* enzyme, L. Green for synthesis of the regioisomers; F. Grynspan, M. G. Finn, and W. G. Lewis for discussion; M. Juin for assistance in crystallography; and G. Sulzenbacher, M. Czjzek, and the ID14 staff of the European Synchrotron Radiation Facility for expert assistance in data collection. This work was supported by grants from the Association Française contre les Myopathies (to P.M.); U.S. Public Health Service (R37-GM18360) and Department of Army Medical Defense (17-1-8014) (to P.T.); and National Institutes of Health (GM 28384), National Science Foundation (CHE-9985553), National Institute of General Medical Sciences, and the W. M. Keck Foundation (to K.B.S.).

1. Argyl-Robertson, D. (1863) *Edinb. Med. J.* **8**, 815–820.
2. Dale, H. H. (1914) *J. Pharmacol. Exp. Ther.* **6**, 147–190.
3. Sussman, J. L., Harel, M., Frolov, F., Oefner, C., Goldman, A., Toker, L. & Silman, I. (1991) *Science* **253**, 872–879.
4. Changeux, J.-P. (1966) *Mol. Pharmacol.* **2**, 369–392.
5. Taylor, P. & Lappi, S. (1975) *Biochemistry* **14**, 1889–1997.
6. Taylor, P. (2001) in *Goodman and Gilman's Pharmacological Basis of Therapeutics* (eds. Hardman, J. G. & Limbird, L. E.), 10th Ed., pp. 175–192.
7. Lewis, W. G., Green, L. G., Grynspan, F., Radić, Z., Carlier, P. R., Taylor, P., Finn, M. G. & Sharpless, K. B. (2002) *Angew. Chem. Int. Ed.* **41**, 1053–1057.
8. Rachinsky, T. L., Camp, S., Li, Y., Ekström, J., Newton, M. & Taylor, P. (1990) *Neuron* **5**, 317–327.
9. Marchot, P., Ravelli, R. B. G., Raves, M. L., Bourne, Y., Vellom, D. C., Kanter, J., Camp, S., Sussman, J. L. & Taylor, P. (1996) *Protein Sci.* **5**, 672–679.
10. Bourne, Y., Taylor, P., Radić, Z. & Marchot, P. (2003) *EMBO J.* **22**, 1–12.
11. Harel, M., Schalk, I., Ehret-Sabatier, L., Bouet, F., Goeldner, M., Hirth, C., Axelsen, P. H., Silman, I. & Sussman, J. L. (1993) *Proc. Natl. Acad. Sci. USA* **90**, 9031–9035.
12. Otwinowski, Z. & Minor, W. (1997) *Methods Enzymol.* **276**, 307–326.
13. Collaborative Computational Project Number 4 (1994) *Acta Crystallogr. D* **50**, 760–763.
14. Brünger, A. T., Adams, P. D., Marius Clore, G., DeLano, W. L., Gros, P., Gross-Kunstleve, R. W., Jiang, J.-S., Kuszewski, J., Nilges, M., Pannu, N. S., et al. (1998) *Acta Crystallogr. D* **54**, 905–909.
15. Murshudov, G., Vagin, A. & Dodson, E. J. (1997) *Acta Crystallogr. D* **53**, 240–255.
16. Roussel, A. & Cambillau, C. (1989) in *Silicon Graphics Geometry Partners Directory*, eds. Silicon Graphics Committee (Silicon Graphics, Mountain View, CA), pp. 77–78.
17. Mohamadi, F., Richards, N. G. J., Guida, W. C., Liskamp, R., Lipton, M., Caufield, C., Chang, G., Hendrickson, T. & Still, W. C. (1990) *J. Comput. Chem.* **11**, 440–467.
18. Laskowski, R. A., MacArthur, M. W., Moss, D. S. & Thornton, J. M. (1993) *J. Appl. Crystallogr.* **26**, 283–291.
19. Christopher, J. A. (1998) SPOCK (Center for Macromolecular Design, Texas A&M University, College Station, TX).
20. Merritt, E. A. & Bacon, D. J. (1997) *Methods Enzymol.* **277**, 505–524.
21. Radić, Z., Pickering, N. A., Vellom, D. C., Camp, S. & Taylor, P. (1993) *Biochemistry* **32**, 12074–12084.
22. Bourne, Y., Taylor, P. & Marchot, P. (1995) *Cell* **83**, 503–512.
23. Bourne, Y., Taylor, P., Bougis, P. E. & Marchot, P. (1999) *J. Biol. Chem.* **274**, 2963–2970.
24. Bourne, Y., Grassi, J., Bougis, P. E. & Marchot, P. (1999) *J. Biol. Chem.* **274**, 30370–30376.
25. Stenberg, K. & Lindqvist, Y. (1997) *Protein Sci.* **6**, 1009–1015.
26. Kuzin, A. P., Nukaga, M., Nukaga, Y., Hujer, A. M., Bonomo, R. A. & Knox, J. R. (2001) *Biochemistry* **40**, 1861–1866.
27. Harel, M., Kleywegt, G. J., Ravelli, R. B., Silman, I. & Sussman, J. L. (1995) *Structure (London)* **3**, 1355–1366.
28. Kryger, G., Silman, I. & Sussman, J. L. (1999) *Acta Crystallogr. D* **56**, 1385–1394.
29. Soreq, H. & Seidman, S. (2001) *Nat. Rev. Neurosci.* **2**, 294–302.
30. Ichchenko, K., Nguyen, T. & Sudhof, T. C. (1996) *J. Biol. Chem.* **271**, 2676–2682.
31. Inestrosa, N. C., Alvarez, A., Perez, C. A., Moreno, R. D., Vicente, M., Linker, C., Casanueva, O. I., Soto, C. & Garrido, J. (1996) *Neuron* **16**, 881–891.
32. Zacharias, N. & Dougherty, D. A. (2002) *Trends Pharmacol. Sci.* **23**, 281–287.
33. Genzor, C. G., Perales-Alcon, A., Sancho, J. & Romero, A. (1996) *Nat. Struct. Biol.* **3**, 329–332.
34. Schumacher, M. A., Miller, M. C., Grkovic, S., Brown, M. H., Skurray, R. A. & Brennan, R. G. (2001) *Science* **294**, 2158–2163.
35. Canete, M., Villanueva, A., Juarranz, A. & Stockert, J. C. (1987) *Cell. Mol. Biol.* **33**, 191–199.
36. LeVine, H., III (1999) *Methods Enzymol.* **309**, 274–284.
37. De Ferrari, G. V., Mallender, W. D., Inestrosa, N. C. & Rosenberry, T. L. (2001) *J. Biol. Chem.* **276**, 23282–23287.
38. Gilson, M. K., Straatsma, T. P., McCammon, J. A., Ripoll, D. R., Faerman, C. H., Axelsen, P. H., Silman, I. & Sussman, J. L. (1994) *Science* **263**, 1276–1278.
39. Kronman, C., Ordentlich, A., Barak, D., Velan, B. & Shafferman, A. (1994) *J. Biol. Chem.* **269**, 27819–27822.
40. Shen, T., Tai, K., Henchman, R. H. & McCammon, J. A. (2002) *Acc. Chem. Res.* **35**, 332–340.
41. Shi, J., Radić, Z. & Taylor, P. (2002) *J. Biol. Chem.* **277**, 43301–43308.
42. Shi, J., Tai, K., McCammon, J. A., Taylor, P. & Johnson, D. A. (2003) *J. Biol. Chem.* **278**, 30905–30911.
43. Cygler, M., Schrag, J., Sussman, J. L., Harel, M., Silman, I., Gentry, M. K. & Doctor, B. P. (1993) *Protein Sci.* **2**, 366–382.
44. Grochulski, P., Li, Y., Schrag, J. D. & Cygler, M. (1994) *Protein Sci.* **3**, 82–91.
45. Mock, W. L. (1995) *Top. Curr. Chem.* **175**, 1–24.

Submitted to J. Amer. Chem. Soc.  
June, 2004

# *In Situ* Click Chemistry: Enzyme Inhibitors Made to Their Own Specifications

*Antoni Krasinski,<sup>†</sup> Roman Manetsch,<sup>†</sup> Zoran Radic,<sup>‡</sup> Jessica Rauschel,<sup>†</sup> Palmer Taylor,<sup>‡</sup> K. Barry Sharpless,<sup>†</sup> and Hartmuth C. Kolb<sup>\*†</sup>*

Contribution from the Department of Chemistry and the Skaggs Institute for Chemical Biology, The Scripps Research Institute, La Jolla, CA 92037, USA, and the Department of Pharmacology, University of California, San Diego, La Jolla, CA 92093-0636, USA

Author E-Mail Address: hckolb@scripps.edu

**Received Date:**

Corresponding author footnote: <sup>†</sup> The Scripps Research Institute, <sup>‡</sup> University of California, San Diego.

**Abstract.** The *in situ* click chemistry approach to lead discovery uses the biological target itself for synthesizing inhibitors by equilibrium-controlled sampling of reagents carrying complementary functional groups until an irreversible reaction essentially ‘freezes’ the pair that best fits the protein’s binding pockets. The *in situ* reaction products are usually highly potent, since they simultaneously engage in multiple binding interactions with the protein. The approach employs bio-orthogonal reagents and coupling reactions, and inhibitor discovery is as simple as determining which reagent combinations form products in the presence of the target. The present publication discusses the optimization of this target-guided strategy with respect to its scope, sensitivity, reliability and throughput, using

acetylcholinesterase (AChE) as a test system. The application of liquid chromatography with mass spectroscopic detection in the single ion mode (LC/MS-SIM) for product identification greatly enhanced the sensitivity and reliability of this method. The LC/MS-SIM technique enabled the testing of multicomponent mixtures, dramatically increasing the efficiency of the method and setting the stage for medium- or even high-throughput screening. In addition to the previously reported *in situ* product *syn-TZ2PA6*, we discovered three new inhibitors, *syn-TZ2PA5*, *syn-TA2PZ6* and *syn-TA2PZ5*, derived from tacrine and phenylphenanthridinium azides/acetylenes, in the reactions with *Electrophorus electricus* and mouse AChE. We have shown all *in situ* hit compounds to be extremely potent AChE inhibitors, with femtomolar dissociation constants, due to the presence of multiple sites of interaction, which include the newly-formed triazole nexus as a significant pharmacophore.

## Introduction

The past decade has seen a paradigm shift in drug discovery from testing small numbers of ‘handcrafted’ compounds and natural products to high-throughput screening of large combinatorial libraries.<sup>1</sup> These developments have gone hand in hand with dramatic improvements in methods for producing, handling and screening large numbers of compounds.<sup>2-5</sup> Despite these achievements, challenges related to the synthesis, purification, and diversity of compound libraries and the pharmacological properties of their members still exist,<sup>6,7</sup> and combinatorial chemistry has yet to deliver on its promises.<sup>8,9</sup> Since typically more than 99% of all compounds in a library are inactive in a given screen, methods for producing just the active compounds are highly desirable. Target-guided synthesis (TGS) addresses this challenge by using the target enzyme for assembling its own inhibitors from a collection of building block reagents. Only building blocks that adhere to the protein’s binding sites react with each other to form highly potent inhibitors that simultaneously access multiple binding pockets within the protein. These target-guided approaches avoid the classical screening of large compound libraries altogether, and hit identification can be as simple as determining whether a given

combination of building blocks has resulted in a product. Follow up tests for determining the inhibitory potency, bioavailability, toxicity and the development of structure activity relationships (SAR) can then be limited to a small number of target-generated compounds, which may dramatically improve the efficiency of the discovery process.

The concept of target-guided synthesis was pioneered almost 20 years ago by D. Rideout *et al.* who observed a marked synergism between the cytotoxic effects of decanal and N-amino-guanidines, which was proposed to be due to the self-assembly of cytotoxic hydrazones *in situ*.<sup>10,11</sup> Since then, several approaches to target-guided synthesis have been explored: (1) Dynamic combinatorial chemistry,<sup>12-21</sup> (2) stepwise target-guided synthesis,<sup>22,23</sup> and (3) kinetically controlled target-guided synthesis.<sup>24-31</sup> The dynamic combinatorial chemistry approach introduced by Lehn *et al.*,<sup>12</sup> relies on building blocks bearing complementary functional groups that react reversibly with each other to form a thermodynamically controlled mixture of products. In the presence of the enzyme, the equilibrium is skewed toward the compounds that show the highest affinity toward the enzyme. Their identification requires the equilibrium to be ‘frozen’ (e.g. by hydride reduction or by lowering the pH), before analysis by HPLC or MS can be performed. The multistep variant of TGS makes only indirect use of the enzyme for inhibitor synthesis.<sup>22,23</sup> In the first step, a library of building blocks is screened to identify candidates that bind to the enzyme. In the second step, the building blocks with the highest affinity are linked together using conventional combinatorial chemistry approaches. The library of ‘divalent’ molecules is then screened for high affinity inhibitors using traditional assays. The kinetically controlled approach uses the enzyme target itself for the synthesis of inhibitors by equilibrium-controlled sampling of various possible pairs of reactants until an irreversible reaction induced by the enzyme essentially connects the pair that best fits its binding pockets.<sup>24-31</sup>

Recently, several successful applications of the kinetically-controlled approach to TGS have been reported. For example, Benkovic and Boger have developed multisubstrate adduct inhibitors (MAI) of the enzyme glycinamide ribonucleotide transformylase (GAR Tfase) by enzyme-templated alkylation of one of its substrates with a folate-derived electrophile.<sup>26-28</sup> More recently, Huc described a similar

approach, in which inhibitors of carbonic anhydrase were generated by alkylation of a thiol with  $\alpha$ -chloroketones in the presence of the Zn(II) enzyme.<sup>29</sup> Competition experiments revealed that the enzyme-templated reaction had produced mainly the alkylation product with the highest affinity for the target. Nicolaou and co-workers have utilized a target-accelerated combinatorial synthesis approach to develop dimeric derivatives of vancomycin.<sup>30,31</sup> Appropriately functionalized monomeric vancomycin derivatives were subjected to olefin metathesis or disulfide formation in the presence of vancomycin's target, Ac-D-Ala-D-Ala or Ac<sub>2</sub>-L-Lys-D-Ala-D-Ala, resulting in the formation of highly potent dimers.

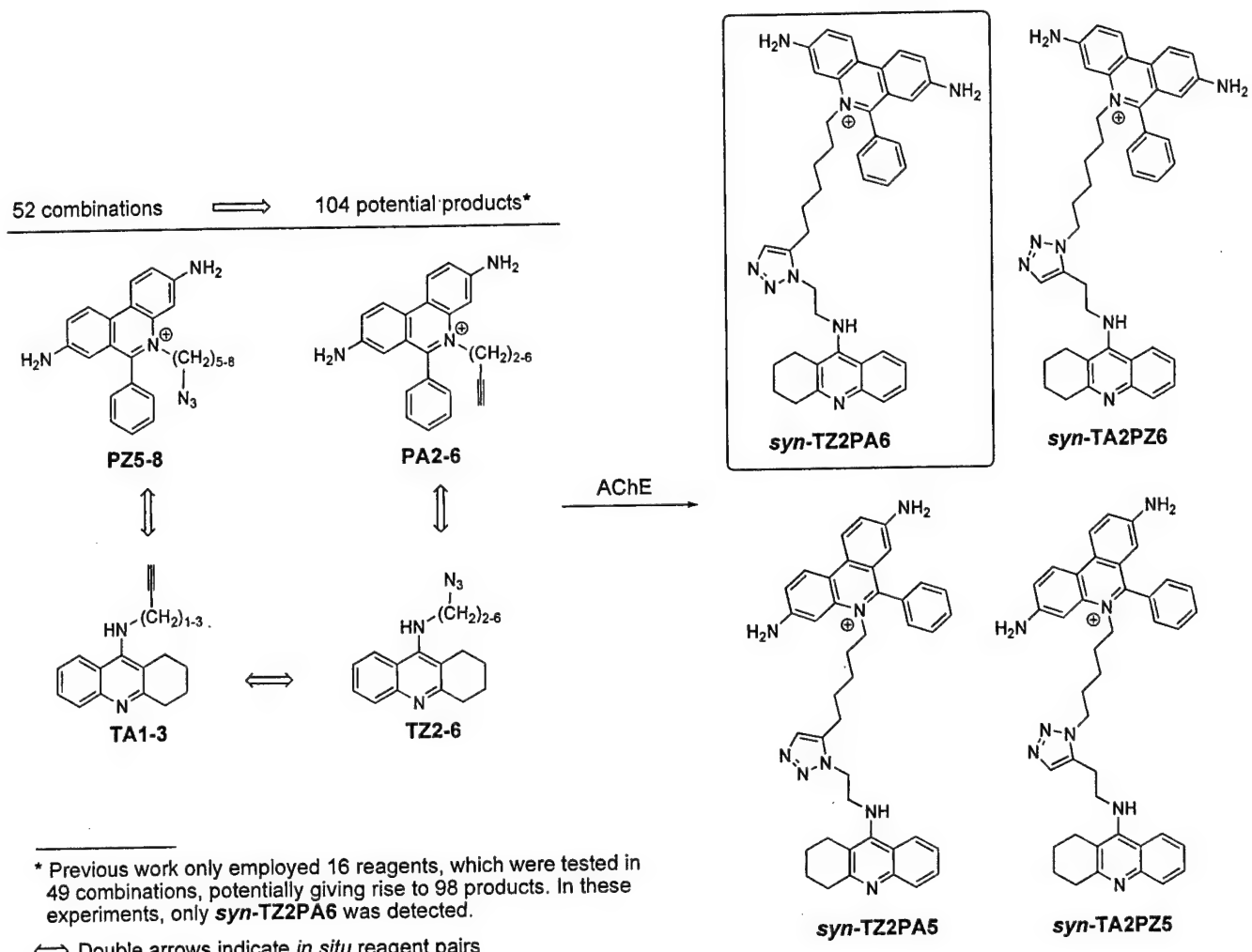
The scope of most TGS methods is limited because of their use of highly reactive reagents (strong electrophiles or nucleophiles, metathesis catalysts etc.), which can react in many ‘unproductive’ pathways, including ones which destroy the enzymic target. In contrast, the recently developed *in situ* click chemistry approach to kinetically controlled TGS<sup>24</sup> uses bio-orthogonal reactions and reagents – the [1,3]-dipolar cycloaddition reaction<sup>32</sup> between azides and acetylenes. This system is especially well-suited for TGS, since (a) the reaction is extremely slow at room temperature, despite the very high driving force which makes it irreversible, (b) it does not involve components that might disturb the binding sites (external reagents, catalysts, by-products), and (c) the reactants are inert to biological molecules. Mock *et al.* had previously provided proof-of-concept by demonstrating that the azide/acetylene [1,3]-dipolar cycloaddition is accelerated by four to five orders of magnitude by the synthetic receptor cucurbituril to give exclusively the *anti*-triazole regioisomer.<sup>33-35</sup>

The biological target for the initial *in situ* click chemistry study, acetylcholinesterase (AChE), catalyzes the hydrolysis of the neurotransmitter acetylcholine and thus plays a key role in the central and peripheral nervous system.<sup>36</sup> Its inhibitors have been employed for over a century in various therapeutic regimens and to investigate the role of acetylcholine in neurotransmission.<sup>37,38</sup> The catalytic site of the enzyme is located at the bottom of a 20 Å deep narrow gorge. A second, peripheral binding site is positioned at the other end of this gorge, near the protein surface.<sup>39,40</sup> A building block library of azides and acetylenes based on the known site specific inhibitors tacrine (active site ligand) and phenyl

phenanthridinium (peripheral site ligand) was developed to probe whether the enzyme would combine selected pairs of complementary reagents to synthesize its ‘divalent’ inhibitors (cf. Scheme 1).<sup>24</sup>

A series of 49 binary mixtures of these reagents was incubated with *Electrophorus electricus* AChE (electric eel AChE) at room temperature for six days, potentially giving rise to 98 products. Analysis of the crude reaction mixtures by Desorption/Ionization on Silicon mass spectrometry<sup>41</sup> (DIOS-MS) revealed only one product, **TZ2PA6**, which was shown by HPLC to be only the 1,5-disubstituted triazole (“*syn*-triazole”) (Scheme 1). This compound, formed by the enzyme, turned out to be the most potent noncovalent AChE inhibitor known to date, with  $K_d$  values between 77 fM (*Torpedo californica*) and 410 fM (murine AChE). In contrast, the *anti*-TZ2PA6 isomer, not formed by the enzyme, is less active by two orders of magnitude.

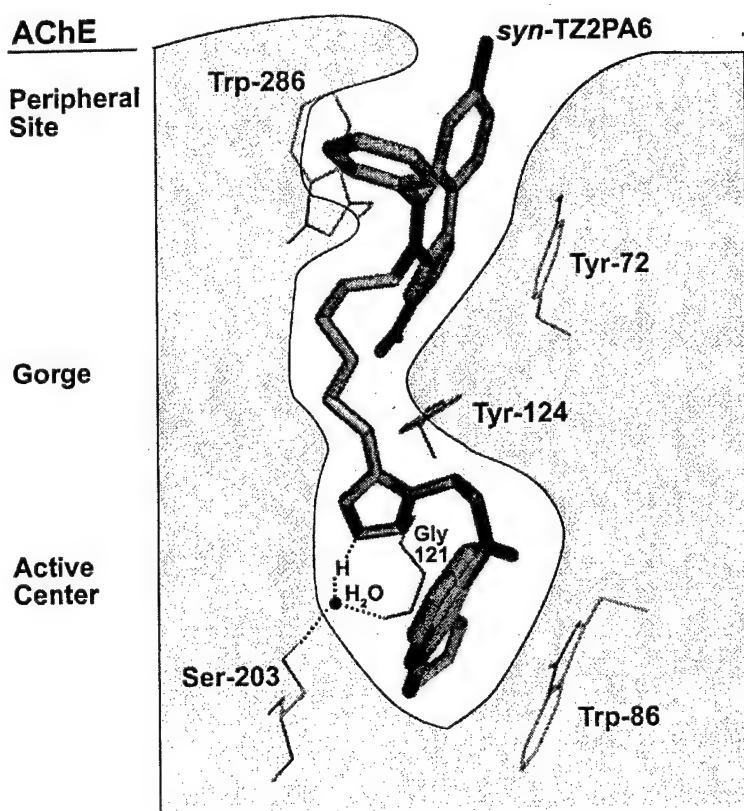
**Scheme 1.** *In situ* click chemistry screening. 52 binary mixtures of azide and alkyne building blocks were incubated with eel AChE as indicated by the double arrows, potentially giving rise to 104 products. Previous work was done without **PZ5**, potentially giving rise to 98 products from 49 reagent combinations, and providing *syn*-**TZ2PA6** as the sole product of the *in situ* reaction with the enzyme.<sup>24</sup>



Recent X-ray structures of both the *syn*- and *anti*-**TZ2PA6** mouse AChE complexes confirmed the multivalent nature of the protein ligand interactions, with the tacrine moiety accessing the active center of the enzyme and the phenylphenanthridinium group the peripheral site (Figure 1).<sup>25</sup> Interestingly, these studies revealed that the triazole unit, created by the azide/alkyne cycloaddition, engages in hydrogen bonding and stacking interactions with amino acid residues in the wall of the gorge. Several important conclusions can be drawn from this observation. First, triazoles are not just passive linkers, but rather

active pharmacophores that may contribute significantly to protein binding, as in the case of the *in situ*-generated product, *syn*-TZ2PA6. Second, the tremendous rate acceleration by AChE<sup>42</sup> is not only due to entropic effects, but also to an enthalpic stabilization of the triazole-like transition state, leading to the observed product. In a more general sense, it appears likely that a compound whose formation is accelerated by the enzyme (i.e., an ‘*in situ* hit’) is very likely a good binder, because the same entropic and enthalpic factors that cause the observed rate acceleration may also stabilize the protein/product complex, and thus strengthen the binding interactions.

**Figure 1.** Schematic representation of the binding interactions between *syn*-TZ2PA6 and mouse AChE.<sup>25</sup>



The higher potency of *syn*-TZ2PA6 compared to the *anti*-isomer manifests itself in a strikingly different binding mode at the peripheral site. The phenylphenanthridinium moiety of the tightly bound *syn*-product inserts itself between tryptophan-286 and tyrosine-72 residues near the gorge rim (Figure 1),

causing the enzyme to adopt a minor abundance conformation in which the tryptophan residue swings out into the solvent to make room for the ligand. This conformation has never been seen before in AChE X-ray structures of the free enzyme or its inhibitor complexes. Thus, the *in situ* click chemistry approach allows one to identify conformations that associate with high affinity inhibitors and that would not be detected by conventional structural methods. These findings have interesting implications for drug discovery, as it is possible to trap a flexible enzyme in a minor abundance conformation by an inhibitor, which is formed inside its binding pockets through irreversible reaction of complementary building blocks.

The goal of the current study was to optimize the *in situ* approach to drug discovery and to investigate its scope. We started by optimizing the mass spectroscopy-based analysis method, since a highly sensitive and reliable method was deemed crucial for success. We then revisited the AChE system to search for additional *in situ* hits from binary azide/acetylene mixtures and from multi-reagent mixtures (combinatorial screening), to study the species dependence of product formation, and to determine *syn/anti* ratios and binding affinities for all products.

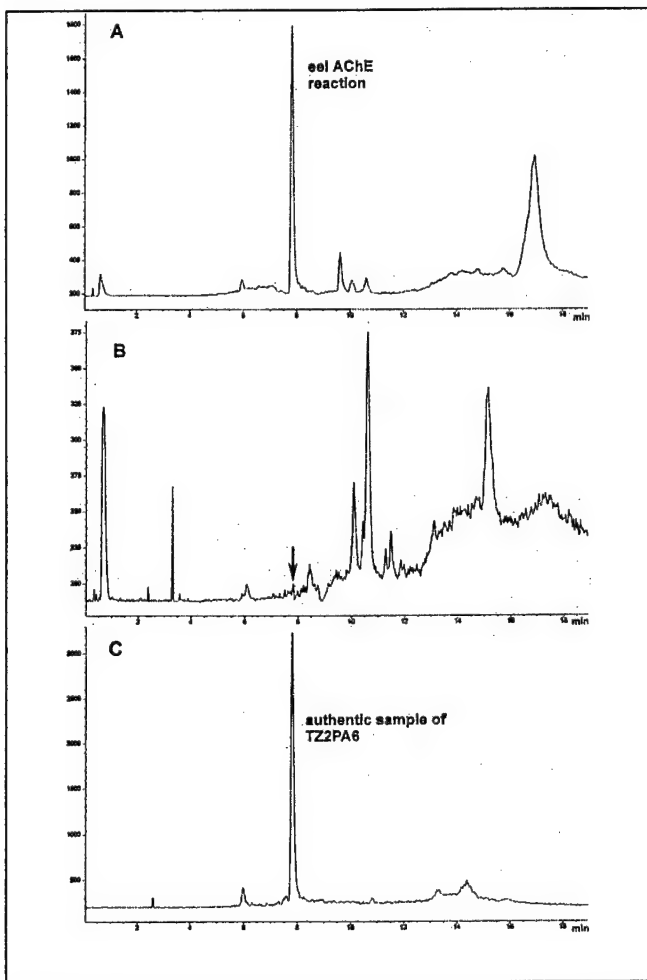
## Results and Discussion

*Optimization of the analysis method.* Previous experiments using the DIOS-MS method for analyzing *in situ* reaction mixtures suffered from poor signal-to-noise ratios, setting the stage for false negative results. Additionally, the analysis of crude reaction mixtures without chromatographic separation of their components complicates unambiguous product identification. To address these issues, we investigated various mass spectroscopy methods and found HPLC with mass spectroscopic detection through electrospray ionization and single ion monitoring (LC/MS-SIM) to give the best results in terms of sensitivity and reliability. *The analysis is extremely easy to perform, allowing crude reaction mixtures to be screened and products to be unambiguously identified by their molecular weights and retention times.*

The new analytical method was validated on the known *in situ* hit **TZ2PA6**. After incubating the building blocks **TZ2** and **PA6** with eel AChE for 6 hours, analysis by LC/MS-SIM gave a distinct

product signal, which was identified by its molecular weight and retention time (Figure 2). Thus, the high sensitivity of this analysis method allowed us to reduce the incubation time from six days to as little as six hours, thereby significantly enhancing the efficiency of lead discovery by *in situ* click chemistry.<sup>43</sup> Control experiments, in which mixtures of the same building blocks were incubated in the presence of bovine serum albumin (BSA) instead of AChE, or in the absence of any protein, failed to give detectable amounts of triazole.

**Figure 2.** *In situ* hit identification by LC/MS-SIM, exemplified by the **TZ2/PA6** pair. **A)** **TZ2** (4.6  $\mu$ M) and **PA6** (24  $\mu$ M) after incubation with eel AChE (1.04  $\mu$ M) at pH 7.5 for 6 hours. **B)** **TZ2** and **PA6** incubated in the presence of BSA (3 mg/mL) instead of AChE. The same trace is obtained in the absence of any protein. **C)** Authentic sample of **TZ2PA6**.



*In situ* lead discovery. Encouraged by these results, we decided to revisit the AChE system using a library of tacrine and phenylphenanthridinium building blocks (“**T-P** library”), which contained one additional member, **PZ5**, compared to previous work, and to screen for additional *in situ* hits with the more sensitive LC/MS-SIM method. Incubation of 52 binary tacrine- and phenanthridinium-based azide/acetylene mixtures as illustrated in Scheme 1 (i.e. **PZ5-8/TA1-3**, **PA2-6/TZ2-6**, and **TA1-3/TZ2-6**) with eel AChE for one day led to the identification of three new hit compounds, **TZ2PA5**, **TA2PZ6** and **TA2PZ5**, in addition to the known hit, **TZ2PA6**. Thus, only **TZ/PA** and **TA/PZ** combinations, not

**TZ/TA** combinations, provided *in situ* hits. All hits were validated by comparing their retention times with those of authentic samples. Additionally, MALDI mass spectroscopy showed distinct molecular ions for the respective products in all four *in situ* reaction mixtures.

Interestingly, all four hit compounds have the newly formed triazole moieties separated by two methylene units from the tacrine core. Other compounds with the same overall spacing between tacrine and phenanthridinium moieties, but a different location of the triazole (e.g. **TZ6PA2**), are not formed, suggesting that the triazole-genesis event is critically linked to a specific location in the protein's gorge. This notion is supported by the X-ray crystal structures of **TZ2PA6**/mouse AChE complexes,<sup>25</sup> which reveal the triazole units are tightly bound inside the gorge through hydrogen bonding and stacking interactions (Figure 1). It is reasonable to assume that these product-stabilizing interactions in that location also favor the transition state leading to that product. Such active participation by the protein would explain the dramatic rate acceleration observed in this system, over that for the uncatalyzed cycloaddition reaction.<sup>42</sup>

*Species dependence.* We decided to investigate the species dependence of product formation, since the X-ray studies were performed with mouse AChE, while eel enzyme was used for the *in situ* screen (58% sequence identity and 70% residue homology by NCBI Blast2).<sup>44,45</sup> Incubation of binary azide/acetylene mixtures from the **T-P** building block library with mouse AChE and analysis by LC/MS-SIM provided the same four hit compounds **TZ2PA6**, **TZ2PA5**, **TA2PZ6** and **TA2PZ5** as before. Thus, not only is mouse AChE able to make its inhibitors, it does so with the same building block preferences as the eel enzyme.

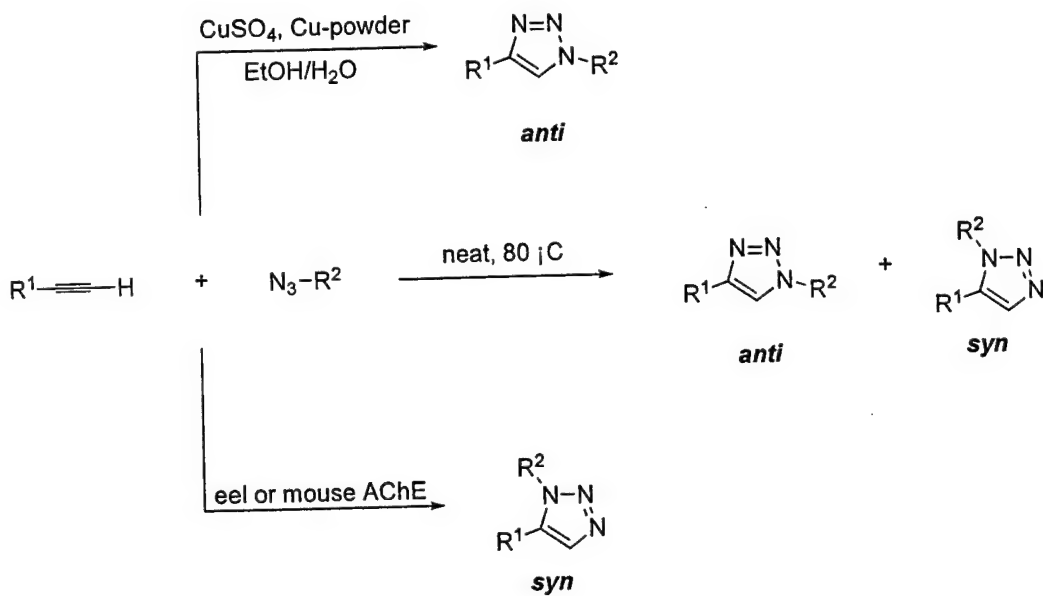
*Combinatorial in situ screening.* *In situ* click chemistry promises a big boost for lead discovery above all because it eliminates the need for high-throughput screening of large compound libraries, since the biological target itself has been forced to generate its inhibitors, which can readily be identified. Moreover, while previous experiments had used only binary azide/acetylene mixtures,<sup>24</sup> we have now found that the enzyme is able to select and assemble the best inhibitors from more complex mixtures of azide and acetylene precursors. This not only reduces the amount of enzyme per reagent combination,

but also increases the screening throughput. Multi-component *in situ* click chemistry screening was made possible by the new LC/MS-SIM method, due to its higher sensitivity and greater reliability of product identification through chromatographic separation of the reaction components. In a proof-of-concept experiment, the azide **TZ2** and a mixture of four phenylphenanthridinium building blocks, **PA2-PA5**, were incubated with eel AChE under standard conditions at 37 °C overnight. LC/MS-SIM analysis of the reaction mixture showed the expected compound **TZ2PA5** to be the sole product (cf. Supporting Information). Encouraged by this success, we expanded this multicomponent approach to the entire tacrine azide/phenylphenanthridinium acetylene library. In order to avoid combinations with degenerate molecular weights (e.g. **TZ3PA5** has the same molecular weight as **TZ2PA6**), which would complicate product identification, especially in view of the similar chromatographic behavior of the TZ-PA compounds, we decided to conduct the experiment in five batches: Mixtures of all five phenanthridinium acetylenes, **PA2-PA6**, were incubated with one tacrine azide at a time in presence of mouse AChE. Analysis by LC/MS-SIM revealed the expected hits, **TZ2PA5** and **TZ2PA6**. These experiments demonstrate that multicomponent screening is feasible, albeit at the cost of a slightly reduced sensitivity. This development is bound to further accelerate lead discovery endeavors based on *in situ* click chemistry.

*Determination of the syn/anti selectivity.* The X-ray co-crystal structures revealed that bound *anti*-**TZ2PA6** has little effect on the enzyme conformation, whereas the bound *syn*-**TZ2PA6** isomer, with its shorter spacer length between the tacrine and phenanthridinium moieties (the distance between the aromatic ring atoms of the tacrine and phenanthridinium moieties that are connected to the linker is 1.52 Å shorter in the *syn*-isomer, which is equivalent to about one C–C bond), forces the enzyme into a very different, and unprecedented conformation. This prompted the question whether AChE would compensate for the deletion of one methylene unit in **TZ2PA5** by forming the ‘longer’ *anti*-triazole instead of the ‘shorter’ *syn*-isomer. Hence, we set out to study the *syn/anti*-selectivity for the formation of **TZ2PA5** and the other new *in situ* hits by LC/MS-SIM. These efforts greatly benefited from the recently discovered Cu(I)-catalyzed process, which provides pure *anti*-triazoles from azides and terminal

alkynes.<sup>46,47</sup> Thus, **TZ2PA5**, **TA2PZ6** and **TA2PZ5** were synthesized each as a mixture of *syn*- and alkynes.<sup>46,47</sup> Thus, **TZ2PA5**, **TA2PZ6** and **TA2PZ5** were synthesized each as a mixture of *syn*- and *anti*-triazoles by the thermal cycloaddition reaction and as isomerically pure *anti*-triazoles by Cu(I)-catalysis (Scheme 2).

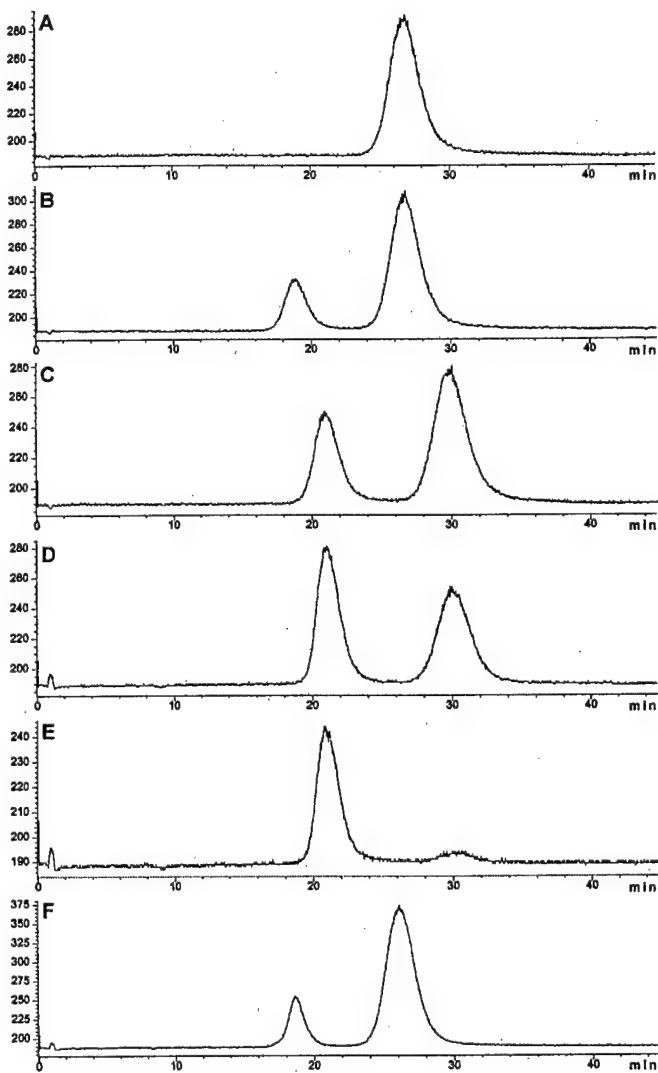
**Scheme 2.** Synthesis of triazoles as reference compounds for the determination of the *syn/anti* ratio of *in situ* hits by HPLC. Equimolar *syn*- and *anti*-triazole mixtures were prepared by heating neat mixtures of the corresponding azides and alkynes at 80 °C for six days. The pure *anti*-regioisomers were readily prepared by the copper(I)-catalyzed reaction between the azide and alkyne reagents.<sup>46,47</sup> Comparison of these compounds with the *in situ* hits by LC/MS revealed the enzyme reaction to generate almost exclusively *syn*-triazoles.



Regioisomer assignment for the triazoles generated by AChE was accomplished by comparing the HPLC traces from the *in situ* reactions with authentic samples from the thermal and Cu(I)-catalyzed reactions.<sup>46,47</sup> While the previous HPLC-UV method required multiple injections and mathematical summation of the traces, the new LC/MS-SIM system allowed us to obtain reliable results with single injections using only one third of the amount of enzyme. We were able to confirm the original assignment of a *syn*-geometry for enzyme-generated **TZ2PA6**,<sup>24</sup> and found all the other products,

**TZ2PA5**, **TA2PZ6** and **TA2PZ5**, from both the eel and mouse AChE reactions to also contain almost exclusively *syn*-triazoles. Figure 3 exemplifies the results for the **TA2/PZ6** pair. While this is not surprising in case of **TA2PZ6** in view of its similarity to **TZ2PA6**, we had expected the shorter linker in **TZ2PA5** and **TA2PZ5** to cause a switch into the ‘*anti*-mode’, which would have extended the linker by approximately 1.5 Å. These results suggest the stereoelectronic requirements for effective catalysis of the cycloaddition inside the enzyme gorge are very strict. We are in the process of investigating this further by X-ray crystallography.

**Figure 3.** Regioisomer determination for mouse AChE-derived *in situ* hits. The *in situ* product, TA2PZ6, was compared by LC/MS-SIM to authentic samples from the thermal and the Cu(I)-catalyzed reactions.<sup>48</sup> **A)** *anti*-TA2PZ6 prepared by the Cu(I)-catalyzed reaction; **B)** co-injection of *anti*-TA2PZ6 prepared by the Cu(I)-catalysis and a mixture of *syn*- and *anti*-TA2PZ6 prepared by the thermal reaction; **C)** mixture of *syn*- and *anti*-TA2PZ6 prepared by the thermal reaction; **D)** co-injection of TA2PZ6 prepared by the *in situ* click reaction and a mixture of *syn*- and *anti*-TA2PZ6 prepared by the thermal reaction; **E)** *in situ* click chemistry reaction; **F)** co-injection of the *in situ* click chemistry reaction and *anti*-TA2PZ6, prepared by the Cu(I)-catalyzed reaction.



*Binding measurements.* The equilibrium dissociation constants for the *syn*- and *anti*-TA2PZ6, TA2PZ5, TZ2PA5 and TZ2PA6<sup>24</sup> isomers, calculated as the ratios of their first order dissociation and second order association rate constants, are listed in Table 1, along with the corresponding free energy of binding values. All eight compounds were respectable inhibitors of both mouse and eel AChE, with dissociation constants in the femtomolar and picomolar range. Even though the femtomolar potency of the original *in situ*-generated inhibitor, *syn*-TZ2PA6, remains unsurpassed for both enzymes, the new *in situ* hits, *syn*-TZ2PA5 and *syn*-TA2PZ6, are close second.  $K_d$  values span three orders of magnitude, which is mainly due to a dramatic 1800-fold variability of dissociation rate constants  $k_{off}$  in the case of the eel enzyme, and 90-fold variability in the case of mouse AChE. In contrast, the on-rates  $k_{on}$  vary only by a factor of two.

**Table 1:** Interaction constants and free energies of binding ( $-RT/\ln K_d$  at  $T = 295K$ ) of triazole inhibitors with acetylcholinesterases.

Inhibitor		$k_{on}$ ( $10^{10} M^{-1} min^{-1}$ )	$k_{off}$ ( $min^{-1}$ )	$K_d$ (fM)	$-RT/\ln K_d$ (kcal mole $^{-1}$ )	AChE source
TA2PZ5	<i>syn</i> -	1.5	0.0081	540	16.6	<i>Electrophorus</i> mouse
	<i>syn</i> -	1.5	0.045	3,000	15.6	
	<i>anti</i> -	0.98	1.4	140,000	13.3	<i>Electrophorus</i> mouse
	<i>anti</i> -	1.1	0.50	44,000	14.0	
TZ2PA5	<i>syn</i> -	0.76	0.00077	100	17.5	<i>Electrophorus</i> mouse
	<i>syn</i> -	1.2	0.028	2,300	15.7	
	<i>anti</i> -	0.90	0.38	42,000	14.0	<i>Electrophorus</i> mouse
	<i>anti</i> -	1.3	0.43	33,000	14.1	
TA2PZ6	<i>syn</i> -	1.2	0.010	830	16.3	<i>Electrophorus</i> mouse
	<i>syn</i> -	1.4	0.0086	610	16.5	
	<i>anti</i> -	1.4	1.4	100,000	13.5	<i>Electrophorus</i> mouse
	<i>anti</i> -	1.7	0.71	42,000	14.0	
TZ2PA6	<i>syn</i> -	1.5	0.0015	99	17.6	<i>Electrophorus</i> mouse
	<i>syn</i> -	1.3	0.0079	410	16.7	

<i>anti-</i>	1.8	0.25	14,000	14.7	<i>Electrophorus</i>
	2.4	0.30	8,900	14.9	<i>mouse</i>

The range in dissociation constants is largest for the eel enzyme, where the free binding energy changes by 4.3 kcal/mole (295K) from the tightest binder, *syn-TZ2PA6* (99 fM), to the weakest compound, *anti-TA2PZ5* (140,000 fM). In the case of the mouse enzyme, the free energy difference between the best binder, *syn-TZ2PA6* (410 fM), and the weakest inhibitor, *anti-TA2PZ5* (44,000 fM), is only 2.7 kcal/mole. We were able to derive a linear free energy relationship from the binding data, which allows us to calculate binding energy changes upon modifying the ligand structure, e.g. from *syn-TZ2PA6* to *anti-TA2PZ5*. The mean values for the energy increments for each structural modification are summarized in Table 2. Further details are provided in the supplementary materials.

**Table 2:** Energy increments for structural changes.

Structural Change	mean $\Delta (-RT/nK_d)$ (kcal mole <sup>-1</sup> )	AChE source
<i>syn</i> → <i>anti</i>	<b>3.1 ± 0.3</b>	<i>Electrophorus</i> mouse
	<b>1.9 ± 0.4</b>	
<i>P6</i> → <i>P5</i>	<b>0.15 ± 0.38</b>	<i>Electrophorus</i> mouse
	<b>0.69 ± 0.45</b>	
<i>TZ</i> → <i>TA</i>	<b>1.0 ± 0.2</b>	<i>Electrophorus</i> mouse
	<b>0.37 ± 0.36</b>	
$\Sigma$ ( <i>syn</i> → <i>anti</i> + <i>P6</i> → <i>P5</i> + <i>TZ</i> → <i>TA</i> )	$\Sigma \Delta(-RT/nK_d)^*$	<i>Electrophorus</i> mouse
	<b>4.3 (4.3)</b>	
	<b>3.0 (2.7)</b>	

# Energy difference values calculated from increments are shown in bold typeface; experimental values are in parentheses.

The energy differences derived from the linear free energy relationship closely match the experimental values. For example, *syn*-TZ2PA6 was calculated to be 4.3 kcal/mole more tightly bound than *anti*-TA2PZ5 in the eel AChE case (3.1 kcal/mole for *syn*-to-*anti* isomerization, plus 0.15 kcal/mole for linker shortening, plus 1.0 kcal/mole for inversion of triazole orientation), whereas the difference is only 3.0 kcal/mole in the mouse enzyme case (1.9 kcal/mole for *syn*-to-*anti* isomerization, plus 0.7 kcal/mole for linker shortening, plus 0.4 kcal/mole for inversion of triazole orientation). The fact that a linear free energy relationship can be successfully applied suggests that the inhibitors are stabilized by largely independent multipoint interactions with the protein, and the data indicate that not only the tacrine and phenanthridinium moieties, but also the triazole ring are involved in binding. Consequently, the triazole apparently functions as an independent pharmacophore.

Many of the structure-activity trends revealed in Table 1 are species dependent. In general, eel AChE rate constants are more dependent on the triazole substitution pattern, while mouse AChE is more sensitive to changes in linker length. For example, the *syn*-/*anti*- preference is much greater for eel AChE (average preference: 3.1 kcal/mole  $\pm$  0.3 kcal/mole, 200-fold) than for mouse AChE (average preference: 1.9 kcal/mole  $\pm$  0.4 kcal/mole, 26-fold). Also, the inversion of triazole ring orientation (TZ2PA6  $\rightarrow$  TA2PZ6, TZ2PA5  $\rightarrow$  TA2PZ5) leads to a marked increase of the dissociation rate in the case of the eel enzyme ( $1.0 \pm 0.2$  kcal/mole, 5.5-fold), while the effects for the mouse enzyme were less pronounced ( $0.4 \pm 0.4$  kcal/mole, 2-fold). For the *syn*-triazole inhibitors, which are the products of the *in situ* click reactions, the shortening of the linker between the triazole and phenanthridinium moieties from six (*syn*-TZ2PA6, *syn*-TA2PZ6) to five methylene groups (*syn*-TZ2PA5, *syn*-TA2PZ5) has only a very small effect on the dissociation constants  $K_d$  for the eel enzyme ( $-0.2 \pm 0.01$  kcal/mole, 0.7-fold), while it leads to a 5-fold increase in the case of mouse AChE ( $0.97 \pm 0.05$  kcal/mol). In contrast, for the *anti*-triazoles, the shortening of the linker reduces the binding affinity for both the mouse and eel enzymes.

The observed species-specific differences of rate and binding trends indicate that the two enzymes interact differently with the products of the *in situ* reactions and their *anti*-congeners. While this may not be seen as surprising in view of the relatively low sequence identity (58%) between the two enzymes, detailed analysis of the primary structures reveals a fully conserved interior of the active center gorge starting from Trp286 of the peripheral site and ending with Trp86 at the bottom of the gorge. Thus, more global properties of the gorge, such as its overall shape or flexibility, not directly and exclusively determined by conserved interior residues, may be responsible for the observed trends.

### Conclusions

We have optimized the *in situ* click chemistry approach to lead discovery and increased its scope using acetylcholinesterase as the target. The application of LC/MS-SIM for product identification greatly enhanced the sensitivity and reliability of the method, and allowed the incubation times to be decreased from six days to as little as six hours. Three new AChE inhibitors, in addition to the known compound, **TZ2PA6**, were identified from a library of tacrine and phenanthridinium azide and acetylene reagents, which contained the building blocks from previous work and the new **PZ5**.<sup>24</sup> All inhibitors, **TZ2PA6**, **TZ2PA5**, **TA2PZ6** and **TA2PZ5**, were produced with almost complete selectivity for the *syn*-triazole isomer by both eel and mouse enzymes. This is a surprising discovery for **TZ2PA5** and **TA2PZ5**, in view of their reduced linker lengths. The *syn*-triazoles, formed by the enzyme, are over 100 times more potent than the corresponding *anti*-isomers. Detailed binding studies revealed all *in situ* hit compounds to be extremely potent AChE inhibitors, with dissociation constants in the femtomolar range, due to the multivalent nature of the binding interactions, which also involve the newly-formed *syn*-triazole heterocycle as an active pharmacophore.<sup>25</sup> The LC/MS-SIM technique enables the testing of multicomponent mixtures, thereby dramatically increasing the efficiency of the method and setting the stage for medium- or even high-throughput screening. We are currently completing a search for novel and drug-like AChE inhibitors based on this method and are investigating other enzyme and receptor targets, such as HIV protease, carbonic anhydrase, and nicotinic acetylcholine receptors.

## Experimental Section

**General.** Reactions requiring anhydrous conditions were run under nitrogen in vacuum flame dried glassware. Reagents were purchased from Acros or Aldrich and were used as received. Reaction progress was monitored by TLC using Merck silica gel 60 F-254 with detection by UV or by immersion in an acidic staining solution (ceric ammonium molybdinate or phosphomolybdic acid). Silica gel 60 (Merck 40–63 µm) was used for column chromatography. The preparation of the library of tacrine and phenylphenanthridinium building blocks was published in the previous paper.<sup>24</sup>

**Instrumentation.**  $^1\text{H}$  NMR and  $^{13}\text{C}$  NMR spectra were recorded with Bruker DRX-600, Bruker DRX-500 or Varian Inova-400 spectrometers. Proton magnetic resonance ( $^1\text{H}$  NMR) spectra were recorded at 600, 500, or 400 MHz. Data are presented as follows: chemical shift (ppm), multiplicity ( $s$  = singlet,  $d$  = doublet,  $t$  = triplet,  $q$  = quartet,  $quin$  = quintet,  $m$  = multiplet), coupling constant (Hz) and integration. Carbon magnetic resonance ( $^{13}\text{C}$  NMR) spectra were recorded at 150, 125, or 100 MHz. Data for  $^{13}\text{C}$  NMR are reported in terms of chemical shifts (ppm). Infrared spectra were recorded on an Avatar 370 Fourier transform spectrometer (IR) and are reported as follows: wavenumbers ( $\text{cm}^{-1}$ ), description (w = weak, m = medium, s = strong, b = broad). High-resolution mass spectra (HRMS) were recorded at the mass spectrometry facility at The Scripps Research Institute, La Jolla. HPLC was performed on an Agilent 1100 LC/MSD with an Agilent 1100 SL mass spectrometer, using four different elution solvents: elution solvent A (0.05 % TFA in  $\text{H}_2\text{O}$ ), elution solvent B (0.05 % TFA in  $\text{CH}_3\text{CN}$ ), elution solvent C (1 %  $\text{Me}_3\text{N}$ /formic acid in  $\text{H}_2\text{O}$ , pH = 7.5) and elution solvent D (MeOH).

### General Procedures for *In Situ* Click Chemistry Experiments.

*Determination of acetylcholinesterase concentrations.* The concentrations of the eel and mouse enzymes are calculated in terms of molarity of active sites based on quantitative measurements of enzyme activity. Commercially available preparations of *Electrophorus* AChE were found to contain approximately 10% active enzyme. The concentration was determined by quantitative measurement of AChE activity using the Ellman assay as previously described.<sup>24</sup> Concentrations of highly purified preparations of mouse AChE, prepared from expression in HEK cells using a recombinant cDNA,<sup>49,50</sup>

containing practically homogeneous enzyme, were determined by quantitative measurement of AChE activity using the Ellman assay and comparing that activity to previously determined values<sup>49</sup> of  $k_{cat}$  in quantitative agreement with band intensities in gels of polyacrylamide gel electrophoresis.

*In situ click chemistry screening procedure for binary reagent mixtures.* The tacrine component (i.e., **TZ2** through **TZ6** or **TA1** through **TA3** dissolved in MeOH) was added to ~1  $\mu$ M solutions of *Electrophorus* AChE (Type V-S, Sigma) or mouse AChE<sup>49,50</sup> in buffer (2 mM ammonium citrate, 100 mM NaCl, pH=7.3-7.5) followed immediately by one of the phenylphenanthridinium components (i.e., **PA2** through **PA6** and **PZ5** through **PZ8**, respectively) and mixed. The final concentrations were as follows: eel or mouse AChE: 1  $\mu$ M; tacrine component: 4.6  $\mu$ M, phenylphenanthridinium component: 24  $\mu$ M; MeOH: 1.5 %. Each reaction mixture was incubated at 37°C for at least six hours. Samples of the reactions were injected directly (15  $\mu$ L) into the LC/MSD instrument to perform LC/MS-SIM analysis (Zorbax SB-C8 reverse phase column, preceded by a Phenomenex C18 guard column, electrospray ionization and mass spectroscopic detection in the positive single-ion mode, tuned to the expected molecular mass of the product). The cycloaddition products were identified by their retention times and molecular weights. Control experiments in the absence of enzyme or in the presence of BSA instead of enzyme failed to produce product signals. For the BSA experiments, AChE was substituted for bovine serum albumin (3 mg/mL). Methanol (1:1 dilution) was added to the reaction mixture prior to LC/MS-SIM analysis, to prevent precipitation of the expected **TZ-PA** triazole product.

*In situ click chemistry screening procedure for multi-component incubations.* A methanolic solution (11.0  $\mu$ L) of phenylphenanthridinium building blocks **PA2** to **PA6** (stock solution contains 400  $\mu$ M of each building block) was added to a solution of mouse AChE (1.1 mL of 1  $\mu$ M AChE, 2 mM ammonium citrate, 100 mM NaCl, pH=7.3-7.5). This mixture was then distributed into six different Eppendorf vials (198  $\mu$ L per vial) and each sample was mixed with one of the tacrine building blocks (**TZ2** to **TZ6**; 2.0  $\mu$ L of a 1.92 mM methanolic stock solution). The final concentrations were as follows: mouse AChE: 1  $\mu$ M; tacrine component: 19.2  $\mu$ M, phenylphenanthridinium component: 4.0

$\mu$ M; MeOH: 2 %. Each reaction mixture was incubated at 37°C for at least 24 hours. Samples of the reactions were injected directly (15  $\mu$ L) into the LC/MSD instrument to perform LC/MS-SIM analysis. The cycloaddition products were identified by their retention times and molecular weights.

*LC-MS analysis.* Although the analysis by DIOS-MS (desorption-ionization on porous silicon mass spectroscopy), as described previously,<sup>24</sup> required only submicroliter amounts for a single measurement, the results suffered from poor signal/noise ratios. In contrast, the LC/MS method with single ion monitoring is considerably more sensitive, with detection limits in the nanomolar range. For example for **TZ2PA6**, we estimated that the compound can readily be detected by the LC/MS-SIM method at concentrations as low as 4 nM, which corresponds to 0.4 % of the used enzyme active site concentration (see supporting information). The analyses were performed on an Agilent 1100 LC/MSD instrument by reverse-phase HPLC using a 30 x 2.1 mm Zorbax SB-C8 column, preceded by a Phenomenex C18 ODS guard column. The injection volume was 15-30  $\mu$ L, and the components were eluted using a gradient (flow rate at 0.3 mL·min<sup>-1</sup>; at 0 min elution solvent mixture A/B=100/0; at 10 min elution solvent mixture A/B=0/100; at 18 min elution solvent mixture A/B=0/100). The mass spectrometer was set to the positive ion mode with single-ion monitoring of only the expected m/z. Under these conditions, *in situ* click chemistry products derived from binary building block mixtures are readily detectable after six hours of incubation in the presence of enzyme.

*Regioisomer determination.* The sensitive LC/MS-SIM method was employed for determining the regioisomer distribution of the *in situ* click chemistry products **TZ2PA6**, **TZ2PA5**, **TA2PZ5** and **TA2PZ6**. The assignment was accomplished by comparing the retention times of the *in situ* products with authentic samples, prepared by thermal cycloaddition (yielding an approximately 1:1 mixture of regioisomers) and copper-catalyzed azide/acetylene reaction (yielding pure *anti*-regioisomers). The *in situ* reaction mixtures were injected directly (15-80  $\mu$ L) into the LCMS as well as co-injected with the reference compounds. Comparison of all traces revealed that the *syn*-isomers were formed preferentially *in situ*. The chromatography was performed on a 100 x 4.6 mm Cyclobond I 2000 DMP column,

preceded by a Phenomenex C18 ODS guard column. The MS detector settings used were the same as for the screening of reactions.

**Synthesis of building blocks and reference compounds.**

**CAUTION! All of the compounds described here (and especially the most potent polyvalent inhibitors) are potentially neurotoxic. They must be handled with extreme care by trained personnel.**

**Tacrine building block TA2.** A mixture of 9-chloro-1,2,3,4-tetrahydroacridine (1.0 g, 4.61 mmol), but-3-ynylammonium chloride (0.54 g, 5.05 mmol) and triethylamine (0.93 g, 9.2 mmol) in pentanol (3 mL) was heated at reflux for 16 h. The reaction mixture was diluted with CH<sub>2</sub>Cl<sub>2</sub>, washed with saturated NaHCO<sub>3</sub> solution, dried over MgSO<sub>4</sub> and concentrated. The residue was purified by chromatography (EtOAc/MeOH = 9/1) to give pure alkyne **TA2** (1.06 g, 4.23 mmole, 92 %). <sup>1</sup>H NMR (400 MHz, CD<sub>3</sub>OD): δ = 8.44 (d, *J* = 8.6 Hz, 1H), 8.04 (d, *J* = 8.1 Hz, 1H), 7.95 (*t*, *J* = 6.4 Hz, 1H), 7.84 (*t*, *J* = 7.5 Hz, 1H), 7.56 (*t*, *J* = 7.5 Hz, 1H), 3.92 (*m*, 2H), 3.04 (*m*, 2H), 2.76-2.60 (*m*, 4H), 2.51 (*t*, *J* = 2.1 Hz, 1H), 1.81 (*m*, 4H) ppm; <sup>13</sup>C NMR (400 MHz, CD<sub>3</sub>OD): δ = 156.8, 152.0, 138.6, 133.4, 126.1, 125.8, 120.0, 116.7, 112.5, 82.1, 74.1, 46.8, 28.8, 25.06, 22.3, 21.1, 20.6 ppm; UV-vis (H<sub>2</sub>O/CH<sub>3</sub>CN/TFA = 40/60/0.05): λ<sub>max</sub> (relative intensities) = 248 (100%), 346 (43%) nm; IR: ν = 3340 (br), 3220 (s), 2940 (m), 2860 (m), 1620 (s), 1580 (w), 1560 (w), 1500 (m), 1470 (m), 1400 (w), 1350 (w), 1260 (m), 1120 (w), 1080 (w), 1030 (m), 950 (w), 830 (m) cm<sup>-1</sup>; HRMS (ESI-TOF) calculated for C<sub>17</sub>H<sub>19</sub>N<sub>2</sub> (MH<sup>+</sup>) 251.1543, found 251.1547.

**Phenylphenanthridinium building blocks.** Building blocks **PA5**, **PZ6** and **PZ5** were prepared according to the previously reported methods.<sup>24</sup>

**PA5:** <sup>1</sup>H NMR (500 MHz, CD<sub>3</sub>OD): δ = 8.64 (d, *J* = 9.1 Hz, 1H), 8.54 (d, *J* = 9.2 Hz, 1H), 7.88-7.76 (*m*, 3H), 7.64-7.52 (*m*, 3H), 7.40-7.34 (*m*, 2H), 6.46 (d, *J* = 2.2 Hz, 1H), 4.52 (*t*, *J* = 7.9 Hz, 2H), 2.22 (*t*, *J* = 2.5 Hz, 1H), 2.16-2.12 (*m*, 4H), 1.44-1.32 (*m*, 4H) ppm; <sup>13</sup>C NMR (500 MHz, CD<sub>3</sub>OD): δ = 160.2, 153.1, 149.7, 136.5, 133.7, 132.3, 130.8, 130.1, 129.9, 129.6, 126.8, 126.0, 123.9, 121.5, 119.7, 110.4,

99.8, 84.5, 70.1, 54.9, 29.4, 28.7, 26.5, 18.2 ppm; UV-vis ( $\text{H}_2\text{O}/\text{CH}_3\text{CN}/\text{TFA} = 40/60/0.05$ ):  $\lambda_{\max}$  (relative intensities) = 293 (100%), 324 (30%) nm; IR:  $\nu = 3360$  (m), 3240 (m), 2960 (s), 2930 (s), 2870 (m), 1730 (s), 1620 (s), 1580 (w), 1490 (m), 1470 (m), 1260 (s), 1160 (m), 1080 (m), 1030 (s), 830 (w) (m),  $\text{cm}^{-1}$ ; HRMS (ESI-TOF) calculated for  $\text{C}_{26}\text{H}_{26}\text{N}_3(\text{M}^+)$  380.2127, found 321.2126.

**PZ5:**  $^1\text{H}$  NMR (500 MHz,  $\text{CD}_3\text{OD}$ ):  $\delta = 8.62$  (*d*,  $J = 9.1$  Hz, 1H), 8.59 (*d*,  $J = 9.2$  Hz, 1H), 7.83-7.72 (*m*, 3H), 7.68-7.54 (*m*, 3H), 7.38-7.32 (*m*, 2H), 6.46 (*d*,  $J = 2.4$  Hz, 1H), 4.52 (*t*,  $J = 8.1$  Hz, 2H), 2.06-1.88 (*m*, 2H), 1.78-1.26 (*m*, 6H) ppm;  $^{13}\text{C}$  NMR (500 MHz,  $\text{CD}_3\text{OD}$ ):  $\delta = 159.9, 152.7, 149.5, 136.4, 133.8, 132.3, 130.8, 130.1, 129.8, 129.4, 126.7, 126.1, 123.8, 121.2, 119.8, 110.4, 99.8, 52.1, 31.0, 29.4, 29.1, 24.8$  ppm; UV-vis ( $\text{H}_2\text{O}/\text{CH}_3\text{CN}/\text{TFA} = 40/60/0.05$ ):  $\lambda_{\max}$  (relative intensities) = 292 (100%), 324 (30%) nm; IR:  $\nu = 3440$  (w), 3360 (m), 3240 (m), 2930 (s), 2860 (s), 2090 (s), 1640 (s), 1630 (s), 1500 (m), 1470 (w), 1260 (s), 1160 (s), 1030 (s), 830 (w)  $\text{cm}^{-1}$ ; HRMS (ESI-TOF) calculated for  $\text{C}_{24}\text{H}_{25}\text{N}_6(\text{M}^+)$  397.2141, found 397.2130.

**PZ6:**  $^1\text{H}$  NMR (600 MHz,  $\text{CD}_3\text{OD}$ ):  $\delta = 8.63$  (*d*,  $J = 9.1$  Hz, 1H), 8.56 (*d*,  $J = 9.2$ , 1H), 7.82-7.76 (*m*, 3H), 7.64-7.54 (*m*, 3H), 7.39-7.33 (*m*, 2H), 6.48 (*d*,  $J = 2.4$ , 1H), 3.46-3.29 (*m*, 2H), 2.06-1.88 (*m*, 2H), 1.80-1.62 (*m*, 4H) 1.22-1.58 (*m*, 4H) ppm;  $^{13}\text{C}$  NMR (600 MHz,  $\text{CD}_3\text{OD}$ ):  $\delta = 160.3, 153.0, 149.7, 136.5, 133.8, 132.3, 130.9, 130.1, 129.9, 129.6, 126.8, 126.0, 123.8, 121.6, 119.7, 110.4, 99.8, 52.4, 30.9, 29.7, 27.5, 27.1, 26.9$  ppm; UV-vis ( $\text{H}_2\text{O}/\text{CH}_3\text{CN}/\text{TFA} = 40/60/0.05$ ):  $\lambda_{\max}$  (relative intensities) = 292 (100%), 324 (28%) nm; IR:  $\nu = 3450$  (w), 3360 (m), 3240 (m), 2930 (s), 2860 (m), 2100 (s), 1640 (m), 1630 (m), 1500 (m), 1460 (w), 1260 (s), 1160 (s), 1030 (s), 830 (w)  $\text{cm}^{-1}$ ; HRMS (ESI-TOF) calculated for  $\text{C}_{25}\text{H}_{27}\text{N}_6(\text{M}^+)$  411.2297, found 411.2292.

**General procedure for the preparation of regioisomerically pure *syn*-triazoles.** Azide (50  $\mu\text{mol}$ ) and alkyne (50  $\mu\text{mol}$ ) were dissolved in methanol (1 mL) and the solvent was subsequently removed under reduced pressure. The residue was heated in an oven at 80-120 °C for four to seven days affording the corresponding triazole as a *syn-/anti*-mixture of approximately 1:1. The regioisomers were separated

by semi-preparative HPLC (Cyclobond I 2000 DMP, 250x10 mm) to yield regioisomerically pure triazoles.

***syn*-TZ2PA5:**  $^1\text{H}$  NMR (600 MHz, CD<sub>3</sub>OD):  $\delta$  = 8.62 (*d*, *J* = 9.1 Hz, 1H), 8.56 (*d*, *J* = 9.2 Hz, 1H), 8.24 (*d*, *J* = 8.2 Hz, 2H), 7.74-7.16 (*m*, 11 H), 6.45 (*d*, *J* = 2.0 Hz, 1H), 4.66 (*t*, *J* = 7.3 Hz, 2H), 4.37 (*m*, 2H), 4.18 (*t*, *J* = 7.2 Hz, 2H), 2.97 (*s*, 2H), 2.57 (*t*, *J* = 6.9 Hz, 2H), 1.93-1.76 (*m*, 6H), 1.41-1.12 (*m*, 6H) ppm; UV-vis (H<sub>2</sub>O/CH<sub>3</sub>CN/TFA = 40/60/0.05):  $\lambda_{\max}$  (relative intensities) = 248 (98%), 292 (100%), 333 (52%) nm; IR:  $\nu$  = 3340 (br), 2950 (m), 2840 (m), 1640 (w), 1620 (w), 1580 (m), 1520 (w), 1500 (w), 1450 (w), 1410 (w), 1320 (w), 1260 (w), 1230 (w), 1110 (w), 1020 (s) cm<sup>-1</sup>; HRMS (ESI-TOF) calculated for C<sub>41</sub>H<sub>43</sub>N<sub>8</sub>(M<sup>+</sup>) 647.3611, found 647.3595.

***syn*-TA2PZ6:**  $^1\text{H}$  NMR (500 MHz, CD<sub>3</sub>OD):  $\delta$  = 8.62 (*d*, *J* = 9.1 Hz, 1H), 8.57 (*d*, *J* = 9.2 Hz, 1H), 8.24 (*d*, *J* = 8.2 Hz, 2H), 7.72-7.12 (*m*, 11 H), 6.41 (*d*, *J* = 2.2 Hz, 1H), 4.70-4.37 (*m*, 4H), 4.30-4.13 (*m*, 2H), 2.83 (*s*, 2H), 2.78-2.60 (*m*, 4H), 1.93-1.76 (*m*, 6H), 1.41-1.12 (*m*, 6H) ppm; UV-vis (H<sub>2</sub>O/CH<sub>3</sub>CN/TFA = 40/60/0.05):  $\lambda_{\max}$  (relative intensities) = 248 (97%), 293 (100%), 334 (55%) nm; IR:  $\nu$  = 3310 (br), 2930 (m), 2860 (m), 1690 (w), 1620 (m), 1590 (m), 1520 (w), 1490 (w), 1450 (m), 1410 (w), 1340 (m), 1260 (m), 1180 (w), 1150 (w), 1050 (s), 950 (w), 830 (w) cm<sup>-1</sup>; HRMS (ESI-TOF) calculated for C<sub>42</sub>H<sub>45</sub>N<sub>8</sub>(M<sup>+</sup>) 661.3767, found 661.3753.

***syn*-TA2PZ5:**  $^1\text{H}$  NMR (400 MHz, CD<sub>3</sub>OD):  $\delta$  = 8.68-8.23 (*m*, 4H), 7.77-7.10 (*m*, 11 H), 6.45 (*d*, *J* = 2.3 Hz, 1H), 4.56-4.17 (*m*, 6H), 3.01 (*s*, 2H), 2.62 (*t*, *J* = 7.48 Hz, 2H), 1.93-1.79 (*m*, 6H), 1.38-1.15 (*m*, 6H) ppm; UV-vis (H<sub>2</sub>O/CH<sub>3</sub>CN/TFA = 40/60/0.05):  $\lambda_{\max}$  (relative intensities) = 247 (97%), 293 (100%), 334 (53%) nm; IR:  $\nu$  = 3350 (br), 2940 (m), 2850 (w), 1620 (w), 1590 (m), 1520 (w), 1480 (w), 1460 (m), 1410 (m), 1350 (m), 1250 (m), 1180 (w), 1160 (w), 1080 (w), 1020 (s), 950 (w), 830 (w) cm<sup>-1</sup>; HRMS (ESI-TOF) calculated for C<sub>41</sub>H<sub>43</sub>N<sub>8</sub>(M<sup>+</sup>) 647.3611, found 647.3596.

**General procedure for the synthesis of isomerically pure *anti*-triazoles.** An aqueous CuSO<sub>4</sub> solution (100 mM, 25  $\mu$ L) and Copper powder (2 mg) were added to a solution of azide (50  $\mu$ mol) and

alkyne (50  $\mu$ mol) in methanol (200  $\mu$ L). The reaction was stirred at room temperature for two to four days. The *anti*-triazole was purified by semi-preparative HPLC.

**anti-TZ2PA5:**  $^1\text{H}$  NMR (600 MHz, CD<sub>3</sub>OD):  $\delta$  = 8.62 (*d*, *J* = 9.1 Hz, 1H), 8.56 (*d*, *J* = 9.2 Hz, 1H), 7.96 (*d*, *J* = 8.6 Hz, 2H), 7.72-7.24 (*m*, 11 H), 6.38 (*d*, *J* = 2.3 Hz, 1H), 4.70 (*t*, *J* = 7.8 Hz, 2H), 4.37 (*m*, 2H), 4.21 (*t*, *J* = 6.1 Hz, 2H), 2.91 (*s*, 2H), 2.53 (*t*, *J* = 7.4 Hz, 2H), 1.88-1.72 (*m*, 6H), 1.41-1.16 (*m*, 6H) ppm; UV-vis (H<sub>2</sub>O/CH<sub>3</sub>CN/TFA = 40/60/0.05):  $\lambda_{\max}$  (relative intensities) = 248 (96%), 292 (100%), 334 (51%) nm; IR:  $\nu$  = 3340 (br), 2930 (m), 2870 (w), 2100 (s), 1730 (w), 1700 (w), 1590 (s), 1520 (w), 1490 (w), 1450 (m), 1370 (m), 1350 (m), 1230 (m), 1180 (m), 1160 (m), 1040 (w), 950 (m), 840 (m) cm<sup>-1</sup>; HRMS (ESI-TOF) calculated for C<sub>41</sub>H<sub>43</sub>N<sub>8</sub>(M<sup>+</sup>) 647.3611, found 647.3597.

**anti-TA2PZ6:**  $^1\text{H}$  NMR (500 MHz, CD<sub>3</sub>OD):  $\delta$  = 8.64 (*d*, *J* = 9.2 Hz, 1H), 8.60 (*d*, *J* = 9.2 Hz, 1H), 8.03 (*d*, *J* = 8.4 Hz, 2H), 7.82-7.34 (*m*, 11 H), 6.48 (*d*, *J* = 2.2 Hz, 1H), 4.70-4.37 (*m*, 4H), 4.30-4.13 (*m*, 2H), 2.88 (*s*, 2H), 2.78-2.67 (*m*, 4H), 1.88-1.72 (*m*, 6H), 1.41-1.16 (*m*, 6H) ppm; UV-vis (H<sub>2</sub>O/CH<sub>3</sub>CN/TFA = 40/60/0.05):  $\lambda_{\max}$  (relative intensities) = 248 (86%), 292 (100%), 334 (48%) nm; IR:  $\nu$  = 3330 (br), 3360 (m), 2940 (m), 2870 (w), 2100 (s), 1730 (w), 1700 (w), 1590 (s), 1520 (w), 1490 (w), 1450 (m), 1370 (m), 1230 (m), 1160 (m), 1120 (w), 1060 (s), 950 (m), 830 (m) cm<sup>-1</sup>; HRMS (ESI-TOF) calculated for C<sub>42</sub>H<sub>45</sub>N<sub>8</sub>(M<sup>+</sup>) 661.3767, found 661.3756.

**anti-TA2PZ5:**  $^1\text{H}$  NMR (400 MHz, CD<sub>3</sub>OD):  $\delta$  = 8.71-8.23 (*m*, 4H), 7.67-7.12 (*m*, 11 H), 6.45 (*d*, *J* 2.2, 1H), 4.40-4.2 (*m*, 6H), 3.01 (*s*, 2H), 2.62 (*t*, *J* = 7.42 Hz, 2H), 1.95-1.72 (*m*, 6H), 1.38-1.20 (*m*, 6H) ppm; UV-vis (H<sub>2</sub>O/CH<sub>3</sub>CN/TFA = 40/60/0.05):  $\lambda_{\max}$  (relative intensities) = 248 (95%), 292 (100%), 334 (51%) nm; IR:  $\nu$  = 3340 (br), 2940 (m), 2840 (w), 2100 (s), 1690 (w), 1590 (s), 1520 (w), 1480 (w), 1450 (m), 1350 (m), 1250 (m), 1180 (m), 1160 (m), 1040 (s), 950 (m), 830 (m) cm<sup>-1</sup>; HRMS (ESI-TOF) calculated for C<sub>41</sub>H<sub>43</sub>N<sub>8</sub>(M<sup>+</sup>) 647.3611, found 647.3596.

**Table 3.** Analytical HPLC conditions for selected compounds.

Compound	Elution solvent mixture					Retention time (min)
		A (%)	B (%)	C (%)	D (%)	
<b>TZ2PA6<sup>a</sup></b>	<i>syn</i>	-	-	56	44	28.4
	<i>anti</i>	-	-	56	44	34.6
<b>TZ2PA5<sup>a</sup></b>	<i>syn</i>	-	-	56	44	19.2
	<i>anti</i>	-	-	56	44	25.2
<b>TA2PZ6<sup>a</sup></b>	<i>syn</i>	-	-	54	46	20.8
	<i>anti</i>	-	-	54	46	29.9
<b>TA2PZ5<sup>a</sup></b>	<i>syn</i>	-	-	46	44	20.6
	<i>anti</i>	-	-	46	44	24.7
<b>TZ2PA6<sup>b,c)</sup></b>	gradient	gradient	-	-	-	7.8
<b>TZ2PA5<sup>b,c)</sup></b>	gradient	gradient	-	-	-	7.6
<b>TA2PZ6<sup>b,c)</sup></b>	gradient	gradient	-	-	-	7.7
<b>TA2PZ5<sup>b,c)</sup></b>	gradient	gradient	-	-	-	7.6
<b>TA2<sup>c)</sup></b>	gradient	gradient	-	-	-	7.2
<b>TZ2<sup>c)</sup></b>	gradient	gradient	-	-	-	7.3
<b>PA5<sup>c)</sup></b>	gradient	gradient	-	-	-	8.6
<b>PA6<sup>c)</sup></b>	gradient	gradient	-	-	-	8.4
<b>PZ5<sup>c)</sup></b>	gradient	gradient	-	-	-	8.5
<b>PZ6<sup>c)</sup></b>	gradient	gradient	-	-	-	8.7

<sup>a)</sup> Analytical HPLC column Cyclobond I 2000 DMP (10x4.6 mm) preceded by a Phenomenex C18 ODS guard column. Isocratic elution at 0.5 mL·min<sup>-1</sup>. <sup>b)</sup> Mixture of *syn*- and *anti*-triazoles. <sup>c)</sup> Analytical column Zorbax SB-C8 (2.1x50 mm) preceded by a Phenomenex C18 ODS guard column. Flow rate 0.3 mL·min<sup>-1</sup>. At 0 min, elution solvent mixture A/B=100/0, at 10 min, elution solvent mixture A/B=0/100, at 18 min, elution solvent mixture A/B=0/100.

#### Determination of AChE - inhibitor association and dissociation rate constants.

The association rate constants ( $k_{on}$ ) were determined by following the rate of quenching of the intrinsic AChE tryptophan fluorescence upon inhibitor binding using the stopped-flow technique.<sup>51</sup> For femtomolar and low picomolar inhibitors, we determined the first order dissociation rate constants ( $k_{off}$ ) by measuring the return of AChE activity upon 5000-fold dilution of 50 – 100 nM concentrations of AChE•inhibitor complex into 250 µg/ml solution of calf thymus DNA (USB Corp., Cleveland, OH)

using the Ellman assay.<sup>52</sup> The DNA sequesters the free phenantridinium ion upon its release from the AChE complex through intercalation, thus preventing its re-association with AChE when inhibitor concentrations in the reactivation medium are above their Kd. High picomolar inhibitors dissociated faster and the reactivation medium contained no DNA, but substrate acetylthiocholine and thiol reagent DTNB were added to the reactivation medium for continuous monitoring of enzyme activity immediately upon dilution of AChE•inhibitor complex. The dissociation constants were determined by nonlinear fitting of the first order increase in enzyme activity up to 100 % of the AChE control activity in mixture containing no inhibitor. Alternatively,  $k_{off}$  of fast dissociating inhibitors were determined using stopped-flow techniques, by following the partial return of intrinsic tryptophan fluorescence caused by dissociation of the AChE•inhibitor complex upon mixing with high concentration (100  $\mu$ M) of competing ligand (ambenonium or other tight binding ligand) to prevent inhibitor re-association.

All experiments were performed in at least triplicate with the standard error of determination smaller than 20% of the mean value. The measurements were performed in 0.1 M phosphate buffer pH 7.0 at 22 °C on a SX.18 MV stopped-flow instrument (Applied Photophysics) or Cary 1E UV/VIS spectrophotometer (Varian).

The equilibrium dissociation constants for the *syn*- and *anti*-TA2PZ6, TA2PZ5 and TZ2PA5 isomers, calculated as the ratios of their first order dissociation and second order association rate constants, are listed in Table 1, along with the dissociation constants for the TZ2PA6 isomers obtained previously.<sup>24</sup>

**Acknowledgements.** We thank Professors M.G. Finn and V. Fokin, and Mr. W.G. Lewis for advice and helpful discussions. We are grateful to Professor G. Siuzdak and Dr. J. Apon for MALDI mass spectroscopy support. This work was supported by the Swiss National Science Foundation and the Novartis Research Foundation (RM), by the Skaggs Foundation (HCK, AK), and the NIH (KBS and PT, grants # R-37GM18360 and DAMDC17C-02-2-0025 to PT).

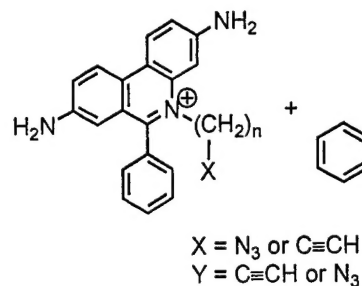
**Supporting Information Available.** LC/MS-SIM traces for *in situ* click chemistry and control experiments, experimental details and LC/MS-SIM traces for regioisomer determination, tables with free energy increments for structural modifications.

## References

- (1) Nicolaou, K. C.; Hanko, R.; Hartwig, W. In *Handbook of Combinatorial Chemistry*; Nicolaou, K. C., Hanko, R., Hartwig, W., Eds.; Wiley-VCH: Weinheim, Germany, 2002; Vol. 1, p 3-9.
- (2) Kolb, H. C.; Sharpless, K. B. *Drug Discov. Today* **2003**, *8*, 1128-1137.
- (3) Terrett, N. *Combinatorial Chemistry*; Oxford University Press: Oxford, UK, 1998.
- (4) Nicolaou, K. C.; Hanko, R.; Hartwig, W. *Handbook of Combinatorial Chemistry*; Wiley-VCH: Weinheim, Germany, 2002; Vol. 1.
- (5) Nicolaou, K. C.; Hanko, R.; Hartwig, W. *Handbook of Combinatorial Chemistry*; Wiley-VCH: Weinheim, Germany, 2002; Vol. 2.
- (6) Kassel, D. B.; Myers, P. L. *Pharm. News* **2002**, *9*, 171-177.
- (7) Geysen, H. M.; Schoenen, F.; Wagner, D.; Wagner, R. *Nat. Rev. Drug Discov.* **2003**, *2*, 222-230.
- (8) "Fixing the drugs pipeline," *The Economist*, March 11th, 2004
- (9) Kubinyi, H. *Nat. Rev. Drug Discov.* **2003**, *2*, 665-668.
- (10) Rideout, D. *Science* **1986**, *233*, 561-563.
- (11) Rideout, D.; Calogeropoulou, T.; Jaworski, J.; Michael McCarthy *Biopolymers* **1990**, *29*, 247-262.
- (12) Huc, I.; Lehn, J.-M. *Proc. Natl. Acad. Sci. USA* **1997**, *94*, 2106-2110.
- (13) Ramstrom, O.; Lehn, J.-M. *ChemBioChem* **2000**, *1*, 41-48.
- (14) Lehn, J.-M.; Eliseev, A. V. *Science* **2001**, *291*, 2331-2332.
- (15) Bunyapaiboonsri, T.; Ramstrom, O.; Lohmann, S.; Lehn, J.-M.; Peng, L.; Goeldner, M. *ChemBioChem* **2001**, *2*, 438-444.
- (16) Eliseev, A. V. *Pharm. News* **2002**, *9*, 207-215.
- (17) Ramstrom, O.; Lehn, J.-M. *Nat. Rev. Drug Discov.* **2002**, *1*, 26-36.
- (18) Otto, S. *Curr. Opin. Drug Discov. Dev.* **2003**, *6*, 509-520.
- (19) Erlanson, D. A.; Braisted, A. C.; Raphael, D. R.; Randal, M.; Stroud, R. M.; Gordon, E. M.; Wells, J. A. *Proc. Natl. Acad. Sci. USA* **2000**, *97*, 9367-9372.
- (20) Erlanson, D. A.; Lam, J. W.; Wiesmann, C.; Luong, T. N.; Simmons, R. L.; DeLano, W. L.; Choong, I. C.; Burdett, M. T.; Flanagan, W. M.; Lee, D.; Gordon, E. M.; O'Brien, T. *Nat. Biotechnol.* **2003**, *21*, 308-314.
- (21) Ramström, O.; Lohmann, S.; Bunyapaiboonsri, T.; Lehn, J.-M. *Chem. - Eur. J.* **2004**, *10*, 1711-1715.
- (22) Maly, D. J.; Choong, I. C.; Ellman, J. A. *Proc. Natl. Acad. Sci. USA* **2000**, *97*, 2419-2424.
- (23) Kehoe, J. W.; Maly, D. J.; Verdugo, D. E.; Armstrong, J. I.; Cook, B. N.; Ouyang, Y.-B.; Moore, K. L.; Ellman, J. A.; Bertozzi, C. R. *Bioorg. Med. Chem. Lett.* **2002**, *12*, 329-332.
- (24) Lewis, W. G.; Green, L. G.; Grynszpan, F.; Radic, Z.; Carlier, P. R.; Taylor, P.; Finn, M. G.; Sharpless, K. B. *Angew. Chem. Int. Ed.* **2002**, *41*, 1053-1057.
- (25) Bourne, Y.; Kolb, H. C.; Radić, Z.; Sharpless, K. B.; Taylor, P.; Marchot, P. *Proc. Natl. Acad. Sci. USA* **2004**, *101*, 1449-1454.
- (26) Inglese, J.; Benkovic, S. J. *Tetrahedron* **1991**, *47*, 2351-2364.
- (27) Boger, D. L.; Haynes, N.-E.; Kitos, P. A.; Warren, M. S.; Ramcharan, J.; Marolewski, A. E.; Benkovic, S. J. *Bioorgan. Med. Chem.* **1997**, *5*, 1817-1830.
- (28) Greasley, S. E.; Marsilje, T. H.; Cai, H.; Baker, S.; Benkovic, S. J.; Boger, D. L.; Wilson, I. A. *Biochemistry* **2001**, *40*, 13538-13547.
- (29) Nguyen, R.; Huc, I. *Angew. Chem. Int. Ed.* **2001**, *40*, 1774-1776.
- (30) Nicolaou, K. C.; Hughes, R.; Cho, S. Y.; Winssinger, N.; Smethurst, C.; Labischinski, H.; Endermann, R. *Angew. Chem. Int. Ed.* **2000**, *39*, 3823-3828.
- (31) Nicolaou, K. C.; Hughes, R.; Cho, S. Y.; Winssinger, N.; Labischinski, H.; Endermann, R. *Chem. - Eur. J.* **2001**, *7*, 3824-3843.

- (32) Huisgen, R. In *1,3-Dipolar Cycloaddition Chemistry*; Padwa, A., Ed.; Wiley: New York, 1984; Vol. 1, p 1-176.
- (33) Mock, W. L.; Irra, T. A.; Wepsiec, J. P.; Manimaran, T. L. *J. Org. Chem.* **1983**, *48*, 3619-3620.
- (34) Mock, W. L.; Irra, T. A.; Wepsiec, J. P.; Adhya, M. *J. Org. Chem.* **1989**, *54*, 5302-5308.
- (35) Mock, W. L. *Top. Curr. Chem.* **1995**, *175*, 1-24.
- (36) Taylor, P.; Radic, Z. *Annu. Rev. Pharmacol. Tox.* **1994**, *34*, 281-320.
- (37) Argyl-Robertson, D. *Edinb. Med. J.* **1863**, *8*, 815-820.
- (38) Dale, H. H. *J. Pharmacol. Exp. Ther.* **1914**, *6*, 147-190.
- (39) Sussman, J. L.; Harel, M.; Frolow, F.; Oefner, C.; Goldman, A.; Toker, L.; Silman, I. *Science* **1991**, *253*, 872-879.
- (40) Harel, M.; Schalk, I.; Ehret-Sabatier, L.; Bouet, F.; Goeldner, M.; Hirth, C.; Axelsen, P. H.; Silman, I.; Sussman, J. L. *Proc. Natl. Acad. Sci. U.S.A.* **1993**, *90*, 9031-9035.
- (41) Wei, J.; Buriak, J. M.; Siuzdak, G. *Nature* **1999**, *399*, 243-246.
- (42) The enzyme-free reaction under these conditions ( $[TZ2] = 4.6 \mu\text{M}$ ;  $[PA6] = 24 \mu\text{M}$ ) is extremely slow, taking several thousand years to reach 50% conversion at  $18^\circ\text{C}$  (second order rate constant at  $18^\circ\text{C}$  in  $1\text{-BuOH}$ ,  $K = 1.9 \cdot 10^{-5} \text{ M}^{-1}\text{min}^{-1}$  [24]). It has been suggested that the tremendous rate acceleration cannot be explained solely on entropy grounds, and more active participation by the enzyme seems likely (R. Huisgen, personal communication).
- (43) The *in situ* screening experiments are generally performed with the following concentrations:  $1 \mu\text{M}$  for the enzyme,  $4.6 \mu\text{M}$  for tacrine components and  $24 \mu\text{M}$  for phenylphenanthridinium components. Due to the sensitive nature of the analysis method, the building block concentrations can be reduced to as low as  $1 \mu\text{M}$  for tacrine reagents and  $6 \mu\text{M}$  for phenylphenanthridinium reagents, without a significant loss of intensity of the product peak. However, lowering the phenylphenanthridinium component concentration to  $1 \mu\text{M}$ , dramatically decreases the reaction rate, and makes the intensity of the product signal prohibitively small.
- (44) The computation was performed at the SIB using the BLAST network service. The SIB BLAST network service uses a server developed at SIB and the NCBI BLAST 2 software.
- (45) Altschul, S. F.; Madden, T. L.; Schäffer, A. A.; Zhang, J.; Zhang, Z.; Miller, W.; Lipman, D. J. *Nucleic Acids Res.* **1997**, *25*, 3389-3402.
- (46) Rostovtsev, V. V.; Green, L. G.; Fokin, V. V.; Sharpless, K. B. *Angew. Chem. Int. Ed.* **2002**, *41*, 2596-2599.
- (47) Tornøe, C. W.; Christensen, C.; Meldal, M. *J. Org. Chem.* **2002**, *67*, 3057-3064.
- (48) All samples were analyzed by LC/MS-SIM with electrospray detection on a Cyclobond I 2000 DMP column ( $4.6 \times 100 \text{ mm}$ , preceded by a Phenomenex C18 ODS guard column) using isocratic elution conditions.
- (49) Radic, Z.; Pickering, N. A.; Vellom, D. C.; Camp, S.; Taylor, P. *Biochemistry* **1993**, *32*, 12074-12084.
- (50) Marchot, P.; Ravelli, R. B. G.; Raves, M. L.; Bourne, Y.; Vellom, D. C.; Kanter, J.; Camp, S.; Sussman, J. L.; Taylor, P. *Protein Sci.* **1996**, *5*, 672-679.
- (51) Radic, Z.; Taylor, P. *J. Biol. Chem.* **2001**, *276*, 4622-4633.
- (52) Ellman, G. L.; Courtney, K. D.; Valentino Andres, J.; Featherstone, R. M. *Biochem. Pharmacol.* **1961**, *7*, 88-95.

## Table of Contents Graphic



52 combinations  $\Rightarrow$  104 potential products

